INFORMATION TO USERS

This manuscript has been reproduced from the microfilm master. UMI films the text directly from the original or copy submitted. Thus, some thesis and dissertation copies are in typewriter face, while others may be from any type of computer printer.

The quality of this reproduction is dependent upon the quality of the copy submitted. Broken or indistinct print, colored or poor quality illustrations and photographs, print bleedthrough, substandard margins, and improper alignment can adversely affect reproduction.

In the unlikely event that the author did not send UMI a complete manuscript and there are missing pages, these will be noted. Also, if unauthorized copyright material had to be removed, a note will indicate the deletion.

Oversize materials (e.g., maps, drawings, charts) are reproduced by sectioning the original, beginning at the upper left-hand corner and continuing from left to right in equal sections with small overlaps.

Photographs included in the original manuscript have been reproduced xerographically in this copy. Higher quality 6" x 9" black and white photographic prints are available for any photographs or illustrations appearing in this copy for an additional charge. Contact UMI directly to order.

ProQuest Information and Learning
300 North Zeeb Road, Ann Arbor, MI 48106-1346 USA
800-521-0600

INTEGRATED DISTRIBUTED FEEDBACK LASERS AND ELECTROABSORPTION MODULATORS FABRICATED USING HELIUM-PLASMA-ASSISTED InP DEFECT INDUCED QUANTUM WELL INTERMIXING

by

GREGORY LETAL, B.ENG, M.ENG.

A Thesis
Submitted to the School of Graduate Studies
in Partial Fulfillment of the Requirements
for the Degree
Doctor of Philosophy

McMaster University

DFB lasers and Modulators Fabricated Using He*-InP Induced QWI

DOCTOR OF PHILOSOPHY (1999)
(Engineering Physics)

McMaster University
Hamilton, Ontario

TITLE: Integrated Distributed Feedback Lasers and Electroabsorption Modulators Fabricated Using Helium-Plasma-Assisted InP Defect Induced Quantum Well Intermixing

AUTHOR: Gregory Letal, B.Eng. (University of Alberta),
M.Eng. (McMaster University)

SUPERVISORS: Professor John G. Simmons
Professor David A. Thompson

NUMBER OF PAGES: xvi, 147

Abstract

An integrated DFB laser and electroabsorption modulator was fabricated by using a novel quantum-well-intermixing technique that uses the defects from a layer of InP grown by He-plasma-assisted gas source molecular beam epitaxy (He*-InP). This is the first investigation into the He*-InP defect induced intermixing, and the first time a device has been fabricated by using this technique.

The first part of this thesis outlines the first investigation into the effects of defects within a layer of He*-InP on annealing-induced quantum-well intermixing. Such a layer can be used to either decrease or increase the total amount of intermixing depending upon the placement of the He*-InP layer relative to the QW and the thickness of the layer. When the layer is far from the QW ($\sim 0.5\mu m$), the total amount of intermixing is decreased. When the layer is close to the QW, the total amount of intermixing can be increased as well as being accompanied by a reduction of the photoluminescence intensity. The main benefit of this intermixing technique is that, unlike dielectric-enhanced intermixing, it is possible to regrow over material that has been intermixed by the He*-InP defect.

The He*-InP defect-induced-intermixing technique has been applied to the fabrication of an integrated electroabsorption modulator and a distributed feedback laser. The techniques developed to fabricated the integrated device are discussed in detail in the second part of the thesis, followed by the device results. The device

characteristics vary with device geometry. For example, the extinction ratios range from 9-16dB for voltage of 3V applied to a 400μm modulator due to the variation of the lasing wavelength with ridge width (for a 3QW structure). The threshold currents of discrete, 600μm long DFB lasers ranged from 18 to 35mA depending on its ridge width and where on wafer it was taken from.

Acknowledgements

I would like to thank my supervisors, Dr. John Simmons and Dr. David Thompson for supporting the research and working to obtain funding for this project through Materials and Manufacturing Ontario (MMO). I would also like to thank the rest of my committee members, Dr. Daniel Cassidy and Dr. David Conn, for reading my thesis and for guiding me through the project. Thanks to the Ontario Graduate Scholarship (OGS), the Natural Sciences and Engineering Research Council (NSERC), and the Department of Engineering Physics for paying for my education, and for making it possible to survive six years as a graduate student.

I'd like to thank all the people who helped to make the research possible: John Hazell for his contribution to the initial research into dielectric-enhanced and for all his work over the years in helping to keep the cleanroom running; Susan Nagy for performing the initial research into the DFB fabrication; Kevin Cearns for showing me how to process ridge-waveguide lasers; Brad Robinson for the research into regrowths and for coordinating the many growths; Scott McMaster for performing all the growths; and Dr. Peter Mascher's research group for the antireflection (AR) coatings- especially Steve Wallace for the useful discussions about AR coatings.

On a more personal note, I'd like to thank my younger siblings, Peter and Cynthia, for pushing me along by obtaining "real jobs" first, and Mike, with whom I had a race to become a doctor (though I still say that I'll be the real doctor- not

just a medical doctor.) Thanks to my parents, Theresa and Jim, for being supportive during my (long) time in school.

Finally, I would like to thank my fiancée Heidi, for her support throughout the degree, for helping me keep my focus, and for the many interesting and useful discussions about the He-plasma-assisted material. Without her support, this degree would not have been possible.

Contents

List of Figures

List of Tables

Glossary of Abbreviations

1.15Q	A quaternary with a RTPL wavelength of 1.15nm
AR	Anti-reflection
DBR	Distributed Bragg Reflector
DFB	Distributed Feedback
EA	Electroabsorption
ECR	Electron Cyclotron Resonance
FP	Fabry-Perot
GSMBE	Gas Source Molecular Beam Epitaxy
I-V	Current-Voltage
L-I	Light-Current
LTPL	Low-Temperature Photoluminescence
MBE	Molecular Beam Epitaxy
MOCVD	Metal-Organic Chemical-Vapour-Deposition
p–i–n	p-doped–intrinsic–n-doped
PL	Photoluminescence
PECVD	Plasma Enhanced Chemical-Vapour-Deposition
PR	Photoresist
QW	Quantum Well
QWI	Quantum Well Intermixing
RTA	Rapid Thermal Anneal
RTPL	Room-Temperature Photoluminescence
RWG	Ridge-Waveguide
SMSR	Side-Mode Suppression Ratio
SOG	Spin-On-Glass
TMM	Transfer Matrix Method
WDM	Wavelength Division Multiplexing

Chapter 1

Background

1.1 Introduction

Optical systems are an integral part of our lives. They have a broad range of uses from sensors in bridges to transmitting information. One of the main reason why these systems have become so prevalent in our society is due to the rapid development of semiconductor opto-electronic devices. These devices have proven to be relatively inexpensive to manufacture and are relatively efficient. Currently, the main opto-electronic semiconductor devices in use are semiconductor lasers, modulators, waveguides, and detectors.

The majority of the research today into optical systems is driven by the telecommunications industry which is continuously looking for ways to transmit more information over longer distances and at a lower cost. Since optical systems have a lower loss per kilometer, they provided an advantage over electrical systems. The reduction in the signal attenuation allows for substantially fewer repeater stations in a optical communications link than in an electrical link; hence, the majority of today's long-haul communication links are optical systems. New research into higher data transmission rates is now being fueled by the increased demand for high-speed data transfer for use by telephones, modems, fax machines, cable television, the internet,

medical imaging and many other similar applications.

The simplest type of optical communication system consists of a laser which is directly modulated by an electrical signal to produce an optical signal, an optical fibre to transmit the optical signal, and a detector which converts the optical signal back into an electrical one. Traditional glass optical fibres have two windows of operation: there is a local loss minimum and dispersion minimum at a wavelength of 1.3μm, and an absolute loss minimum at 1.55μm [1]. Modern long-haul optical communication systems normally take advantage of the low-loss window at 1.55μm. This is also partly due to the availability of erbium-doped fibre amplifiers that operate at a wavelength of 1.55μm. Erbium doped amplifiers provide a method for optical amplification. Electrical amplification is a much more expensive process since additional lasers, detectors, and electronics are required. Lasers are used in optical communication systems because they are high-power coherent monochromatic sources. A monochromatic source is required because in an optical fibre, different wavelengths travel at different speeds due to material dispersion (which is particularly important in the 1.55μm window where the material dispersion is not zero). This dispersion causes the pulses of light containing the data to broaden and overlap which makes it more difficult to decode the optical signal.

Medium-range optical data links use modulators to modulate the light instead of direct laser modulation. This is mostly because direct laser amplitude modulation is accompanied by a strong frequency modulation known as chirp. Chirp greatly increases the bandwidth of a transmitted signal and, due to fibre dispersion, makes direct laser modulation suitable for only short or slow data links. A narrow bandwidth signal has also become essential with the advent of wavelength division multiplexing (WDM) in which multiple wavelengths are sent down the same fibre. As the wave-

length spacing becomes tighter, the bandwidth of the signal must be decreased. These more complicated optical systems using separate modulators are needed since they produce substantially less chirp than direct laser modulation.

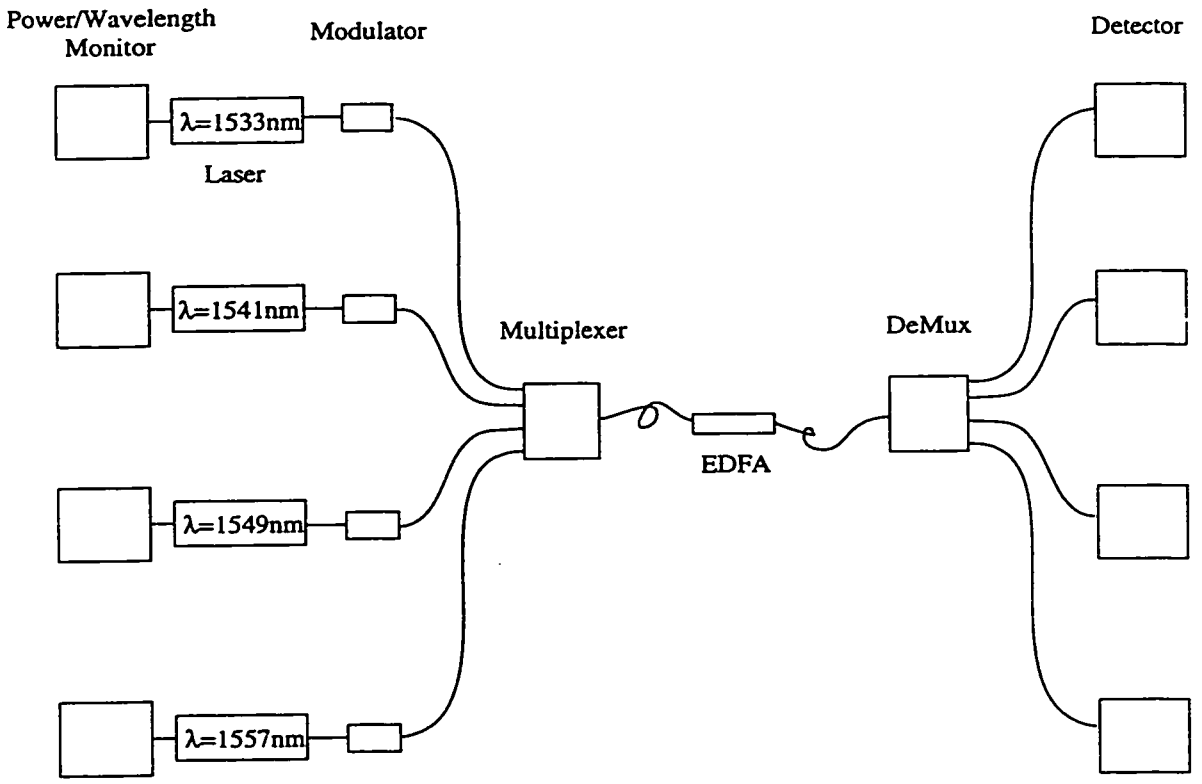

Figure 1.1: Schematic diagram of an optical telecommunications link

Long-haul data links consist of even more components. A schematic diagram of a 4-channel WDM link is illustrated in Fig. 1.1. As can be seen, there are many components that make up the link including multiple lasers, modulators, wavelength/power monitors, detectors, a multiplexer, a demultiplexer, and a erbium-doped fibre amplifier (EDFA). Each of these devices need to be connected together by lenses and waveguides, which can be difficult and costly to package. Also, Fig. 1.1 illustrates only a 4-channel system. Sixteen channels with a 100GHz channel spacing are

becoming prevalent, and the next generation 32 channel system has a 50GHz channel spacing which will require even more components. Hence, one can understand why device integration is being investigated. Integrating the devices would result in a great simplification in the packaging required: the more devices there are, the more cost effective it is to integrate them. (Imagine trying to fabricate a computer with today's capabilities using discrete devices.) In theory, lasers, modulators, wavelength monitors, waveguides, and multiplexers can all be integrated since there are semiconductor versions of all these devices. In practice, it is not an easy procedure, especially when considering the reliability requirements for modern opto-electronic devices. The focus of this thesis is on the development of an integrated distributed feedback (DFB) laser and an electroabsorption (EA) modulator by a novel quantum-well intermixing technique. The integration procedures and device requirements are discussed in the following pages.

1.2 Semiconductor Background

1.2.1 Bulk Crystals

There are two broad categories of semiconductors: those with direct and those with indirect bandgaps. A schematic diagram of these two cases is illustrated in Fig. 1.2. This diagram contains the four most common bands seen in semiconductors: the conduction band, the heavy-hole (HH) band, the light-hole (LH) band, and the split-off (SO) band. Most opto-electronic devices are fabricated from direct band-gap semiconductors such as gallium arsenide (GaAs), indium phosphide (InP), or their compounds. These semiconductors have three main valence bands: the heavy hole, light hole, and split-off band. The heavy hole and light hole are distinguished by their curvature, which determines the effective mass of the holes at the top of the band as

described by the equation [2]

$$\frac{d^2E}{dk^2} = \frac{\hbar^2}{m^*} \tag{1.1}$$

where m^* is the effective mass. This effective mass is used to help describe how the carriers will behave when perturbed by electric or magnetic fields–electrons and holes behave like particles with a mass equal to the effective mass.

In a direct-bandgap semiconductor, the minima in the conduction band and the maxima in the valence band occur at the same momentum values. In such a case, when a hole in the valence band and an electron in the conduction band recombine, the most probable transition is one that results in the emission of a photon. Momentum is conserved since the photon has very little momentum. This is known as radiative recombination. Other transitions are possible such as a non-radiative transition involving a defect level, or the energy from the recombination might cause an intraband transition instead of the generation of a photon (i.e. Auger recombination). The transition in an indirect bandgap semiconductor is a little more complicated. In order to recombine, the hole and electron must also lose momentum. Since a photon has very little momentum, it is much more likely that the transition will involve phonons which do have momentum. For devices such as semiconductor lasers the principle recombination process must be radiative recombination which is why most opto-electronic devices are fabricated from direct band-gap semiconductors. Alternatively, if a photon of light is incident on a semiconductor, there are three possibilities: if the photon has less energy than the bandgap, it will be transmitted; if it has more energy than the bandgap it can be either absorbed or it will induce stimulated emission. It is these characteristics that lead to the development of optoelectronic devices, such as lasers, modulators, waveguides and detectors [2].

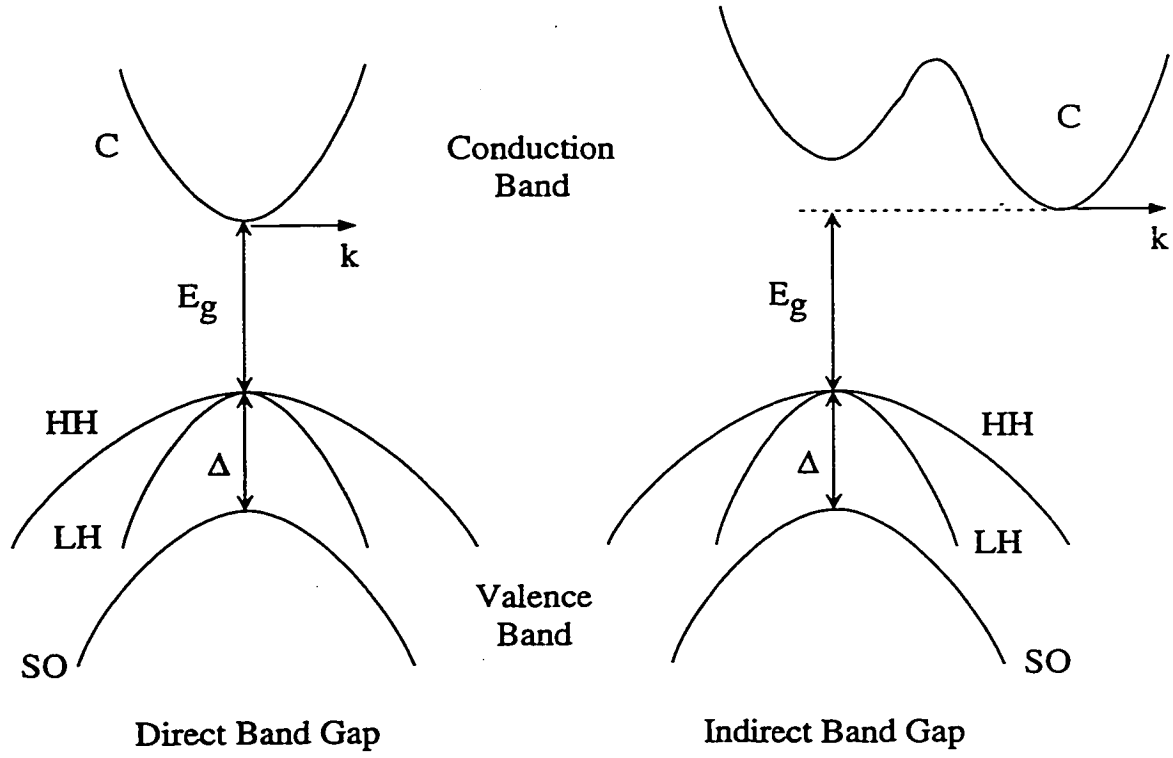

Figure 1.2: Schematic diagram of a direct and indirect bandgap semiconductor

1.2.2 General Device Structures

Modern optoelectronic devices contain structure to constrain both the optical mode and carriers. This is done by growing layers of different compositions (which equates to materials of different bandgaps) on a semiconductor wafer. Wide bandgap materials are used at the top and bottom of the device, and narrower bandgap materials are used in the centre. When current is injected into the device, the majority of the carriers become trapped in the narrow bandgap region where they recombine. Narrow bandgap materials also have a higher index of refraction, so the same structure can be used to confine both carriers and the optical mode. This type of structure is known as a double-heterostructure. For recombination to occur, holes and electrons must

be present. This can be accomplished by designing the device as a p-i-n (p-doped, intrinsic, n-doped) type structure. When a positive voltage is applied to the p-side, current flows through the device resulting in holes being injected from the p-side and electrons from n-side into the narrow bandgap material where they recombine. For a more quantitative description see the book by Streetman [2].

1.2.3 Quantum Wells

When the middle layers in heterostructures are made extremely thin (on the order of 100Å), quantum-confinement effects can strongly affect the electron transition energy in the material; hence, quantum-wells provide another way to modify the electron transition energy. Quantum wells also have a different density of states than bulk material, which also acts to improve the energy distribution of the carriers (from a laser or modulator standpoint) by increasing the number of states at the lowest transition energy within the device [3].

The increase in transition energy due to the quantum confinement effect depends on: the size of the well; the band energy difference between the well and the barriers (which depends on their compositions and the amount of strain); and the well profile. Strain can be added to the quantum-wells to further modify the band structure since the quantum-wells are much thinner than the critical thickness of the material. The procedure for calculating the energy levels in a finite quantum-well is discussed in Appendix A. It is the dependence on the well composition and the well profile that make the transition energy highly susceptible to any quantum-well intermixing process. In quantum-well intermixing, diffusion (or defect-enhanced diffusion) is used to exchange atoms within the quantum-well and the barrier thereby changing the shape of the quantum-well. The quantum-well intermixing (QWI) process is one way to fabricate devices with different transition energies on the same wafer,

thereby making it possible to integrate various optoelectronic devices. Methods for QWI is discussed in more detail in section 1.3. These benefits, and the development of epitaxial growth techniques have allowed for the majority of modern optoelectronic devices to be based on designs using quantum-wells [3].

1.2.4 Motivation for Studying $\mathbf{In_{(1-x)}Ga_xAs_yP_{(1-y)}}$

The most common semiconductor material used in optical communications is indium gallium arsenide phosphide ($In_{(1-x)}Ga_xAs_yP_{(1-y)}$ where x and y refer to the compositions of Ga and As respectively) grown on an indium phosphide (InP) substrate. The quaternary is used to provide the greatest control over bandgap, lattice constant, and strain in layers grown on the InP substrate. By using this material, it is possible to fabricate devices with an operating wavelength that coincides with the ideal wavelength for optical communications using silica glass fibres. This ideal wavelength is determined by the loss minima of optical fibre (which occurs at 1.55μm) as well as the operating wavelength of erbium-doped optical fibre optical amplifiers. As stated earlier, if erbium-doped fibre amplifiers (or some other type of optical amplifier) were not used, one would require electrical amplification of the signal which requires many more components. It is these factors that make long-distance optical communication links economically viable; hence, InGaAsP devices manufactured to operate in the 1.55μm window are employed for most applications.

1.3 Optoelectronic Device Integration

Integration of different discrete devices have yielded a decrease in the total device cost and an improvement in performance of many different systems. A perfect example of this is the integration of resistors, capacitors and transistors to form the

modern microprocessor which would have been impossible to create using discrete devices. Improvements in optical systems can also be realized by device integration. Device integration can greatly reduce packaging costs as well as improving device performance by increasing optical coupling between different devices. However, the integration of opto-electronic devices normally requires the integration of materials with different bandgaps (or transition energies).

Photonic systems researchers have attempted the integration of waveguides, detectors, lasers and modulators by using many different techniques. For the devices to interact properly with an incoming photon, they require different material properties: waveguides require the photon to have less energy than the electron transition energy in the material so that the material is transparent. Laser and detectors require the photon energy to be greater than that of the transition energy so that the photons can interact with the carriers within the semiconductor. The electron transition energy of electroabsorption (EA) modulators are required to be variable so that in the off-state, the material is absorbing, and the on-state, the material is transparent. A compromise is normally required for modulators so that they are not too lossy in the on-state, yet easily switched to the off-state. The transition energy of a quantum-well can be changed by one of three methods: heating or cooling the lattice; applying a bias so that the bands bend in a phenomena known as the quantum-confined-stark effect; or changing the composition or band profile of the quantum-well.

Localized heating has limited use for integrated photonic devices. Bandgap shrinkage due to localized heating can be realized by current injection but it is not a very effective method for changing the bandgap, since the obtainable shift in the transition energy is relatively small. This limits the types of devices that can be integrated. Also, the switching time constant for local heating is relatively slow which

makes it an unsuitable method for changing the absorption in an EA modulator. Even so, Delprat et al. [4] have illustrated the fabrication of an integrated distributed feedback (DFB) laser and modulator and Lammert et al. [5] have illustrated the fabrication of a distributed Bragg reflector (DBR) laser and (EA) modulator by using this technique. In both these papers, localized heating is used to reduce the transition energy in the laser section thereby moving the gain peak to a longer wavelength. The broadness of the semiconductor laser gain is also used to their advantage by using the grating to pull the lasing wavelength to a longer wavelength than the gain peak to increase the separation between the lasing wavelength and the wavelength of the absorption edge of the modulator. (The requirements for an integrated laser and modulator will be discussed in detail in section 2.8.) The EA modulators were based on the quantum-confined-Stark effect (QCSE). The QCSE is the name for the observed reduction in the transition energy of a quantum well when a bias is applied [6] and can therefore be used to modify the absorption edge of a modulator. It is an effective principle to base the development of EA modulators in which the modulator is switched from a transparent state to an absorbing state by applying a bias. The QCSE will be discussed in further detail in section 2.5.

The most effective way of integrating different optoelectronic devices is by using quantum-wells with different transition energies. Fabricating adjacent devices with different transition energies of the quantum-wells can be performed in three ways: by etching and regrowth; by selective-area epitaxy, or by the post-growth technique known as quantum-well intermixing (QWI). The etching and regrowth technique involves completely etching away the quantum-wells in the region where the transition energy needs to be changed. This is the most obvious and direct way to implement integration of photonic devices since one has complete control over the composition of

the quantum-wells in each section. However it is extremely difficult to correctly align the active regions of the different devices, since tight control of the growth and etching processes is required. As well, the traditional regrowth process is non-selective and results in material being regrown on top of the material from the first growth. Patterning and tightly controlled etching must be used to remove this material before devices can be fabricated. Due to the large amount of processing required, this method becomes unfeasible if more than two different transition energies are required in the integration process–each device with a different transition energy will require another set of etching and regrowth. Selective area epitaxy and quantum well intermixing are much more practical techniques, as will be discussed in sections 1.4 and 1.5 respectively.

1.4 Selective Area Epitaxy

Selective area epitaxy is one photonic integration technique that has been examined extensively by various research groups [7, 8, 9, 10, 11]. The material commonly grown by metalorganic vapour phase epitaxy (MOVPE) [7], or less commonly, by MBE [11] and is based on the principle that an epilayer will not grow on an amorphous oxynitride layer. Selective area epitaxy by MBE has not been very successful since polycrystalline material grows on the oxynitride, and the available shifts are limited. However, a large degree of success has been achieved by MOVPE, where there is no growth on the oxynitride layer. Instead, the growth material is desorbed, where it is free to be scattered back to the substrate. If the material is scattered back to an area where there is no oxide, there is a high probability that it will be adsorbed, which will lead to an enhanced growth rate in that region [7]. The enhanced growth rate results in thicker quantum wells that have a smaller transition energy due to

the reduction in the quantum confinement effect. Therefore, to produce a device, stripes are patterned in the oxynitride, and the amount of red-shift depends on the width of the area without the oxynitride. Red-shifts in excess of 100meV are possible (The PL wavelength can be made to vary from 1475 to 1575nm as the mask width is varied from 0 to 50μm) [8]. Devices with different transition energies are integrated by using different oxide gap widths. The main shortcoming of this method is that it does not allow complete control of the bandgap in two dimensions, unlike quantum well intermixing [12, 13], and the material thickness (and therefore transition energy) varies across the width of the window in the oxide [14, 15]. Even so, there are many papers which discuss the fabrication of integrated DFB lasers and EA modulators by selective-area epitaxy [16, 9, 10]. For these devices, an oxide mask is used to red-shift the quantum wells in the laser section thereby moving the gain peak to longer wavelengths. The lasing wavelength will therefore be at a longer wavelength than the absorption edge of the modulator. The device properties will be discussed further in section 5.4 where they are compared to the devices fabricated in this thesis.

1.5 History of QW Intermixing

Quantum well intermixing is a preferred technique in the development of photonic integrated circuits. This is because it can be performed after the growth is completed and it is usually straight-forward to obtain a wide range of bandgaps on the same wafer. Also, device integration is simplified because the waveguiding region is guaranteed to be continuous from device to device because the waveguides of all devices were grown at the same time. The main disadvantage over a regrowth fabrication technique is that each device will have an identical structure (i.e. doping profiles, numbers of quantum-wells, waveguide profiles etc.); hence, design compromises must

be made for some applications.

In the intermixing process, the interdiffusion between the material in the barriers and that in the quantum-wells is induced. This results in a change in the shape and depth of the quantum-well profile thereby changing the transition energy of the quantum-well. A sample calculation for a quantum-well before and after intermixing is given in Fig. 1.3. For an intermixing process to be useful, several requirements must be met [13]:

1. The shift in the bandgap energy must be controllable and reproducible both from run-to-run and spatially across the wafer.

2. Sub-bandgap losses must not increase appreciably.

3. The electrical properties must not be adversely affected.

4. The operating lifetime of the device should not be decreased.

There are many techniques for producing an intermixed quantum-well in InP based devices. Ion implantation [13], impurity induced-intermixing [12, 17], impurity free-intermixing [18, 19, 20, 21, 22], intermixing by surface damage [12], localized laser heating [12], and intermixing by using the gallium vacancies found in low-temperature gallium arsenide [23] (which is only applicable to GaAs-based devices) have all been demonstrated. For the technique to be useful, it is necessary for defined areas on the wafer to be preferentially intermixed with respect to other areas. In all the techniques mentioned here, except for laser annealing, this is done by introducing defects into the crystal lattice. These defects then diffuse through the QW's and enhance the rate of intermixing. More detail of the main techniques is given in the following sections.

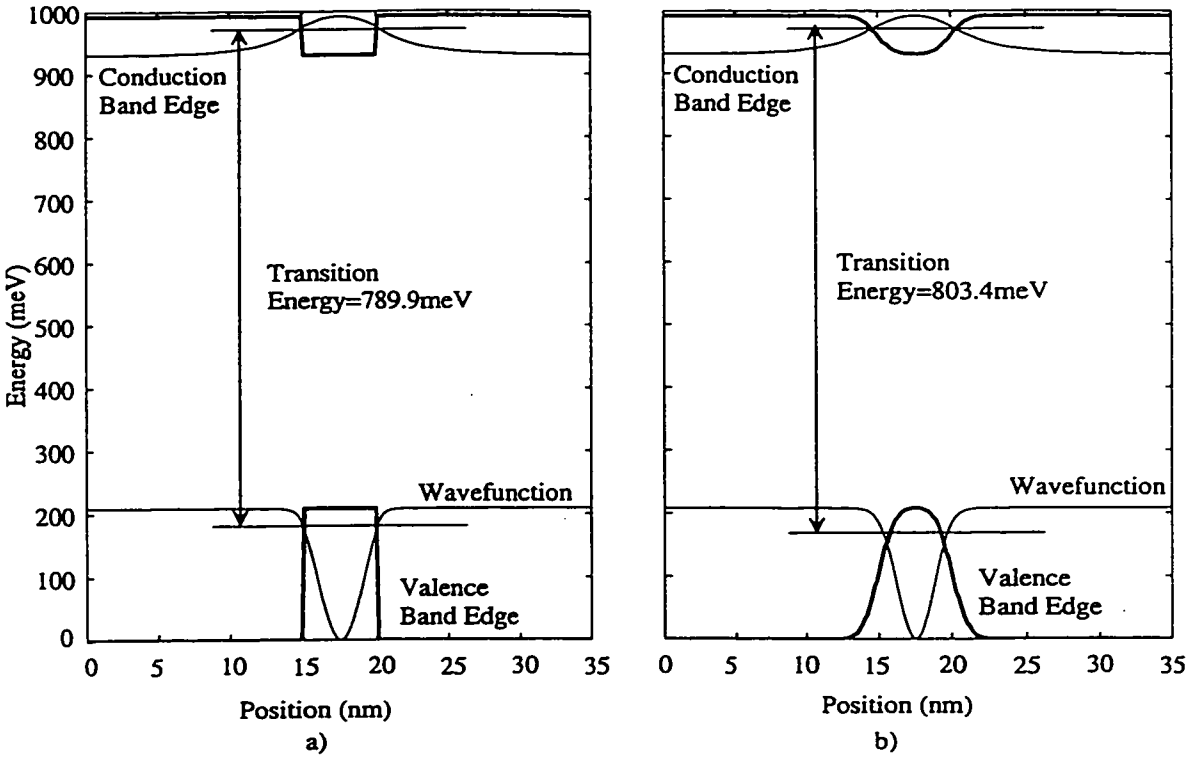

Figure 1.3: Illustration of the effect of intermixing a QW

1.5.1 Ion Implantation Induced Intermixing

The basic process for ion-implantation-induced intermixing is straightforward. For InP-based devices, damage is caused to the crystal by implanting energetic ions into the semiconductor crystal [13]. Phosphorus is chosen so that the implanted species does not dope the semiconductor. The depth of the damage can be varied by changing the ion energies typically from 0.5MeV to 6MeV. The implantation is performed at 7° to the substrate surface normal to prevent channeling. The ion impact causes vacancies and other defects to be formed. The crystal is then annealed, typically at 700°C for 30s, to repair the crystal damage [13]. In the InP material system, the vacancies formed are suggested to be highly mobile; hence, during the

anneal, they diffuse through the QWs and cause intermixing [13]. The amount of intermixing is controlled by the depth of the implantation and ion dose which, in turn, controls the number of defects that diffuse through the quantum-wells during the subsequent thermal anneal treatment. The implant depth and the number of defects created can be controlled by either varying the incident ion species and energy or, alternatively, by using a thick oxide mask (that can be of varying thickness) to decrease both the energy and the number of ions reaching the semiconductor. Therefore, an oxide mask can be used to integrate device components with different electron transition energies. Using ion-implantation, blue shifts in excess of 40meV are possible [13].

1.5.2 Laser Heating Induced Intermixing

Laser-induced intermixing is essentially a localized annealing process which uses heat to increase the interdiffusion rate of the wells and barriers [12]. A high power (usually Nd:YAG) laser is tuned to a wavelength such that the light is absorbed in the active region (i.e. quantum-wells and barriers). Thus, a large number of carriers are generated within the material which then recombine resulting in heat generation. This results in a blue shift of the transition energy which can be in excess of 100meV. A 100nm gold mask can be used to provide spatial selectivity. The main drawback to this method is that there is poor lateral selectivity because of the high thermal conductivity of the sample [12].

The spatial selectivity of the laser-induced intermixing method may be improved by using pulses of light to produce rapid transient heating. The resulting rapid localized thermal expansion causes the formation of point defects. The sample can then be subjected to a high-temperature anneal which causes the point defects to diffuse and intermix the quantum-wells and barriers. The anneal can be performed

at the same time as the defect formation by using a continuous wave (CW) laser–a technique that has the added benefit of reducing the probability of formation of extended defects. A spatial resolution of 25μm is possible using this technique [12].

1.5.3 Dielectric-Enhanced Intermixing

Dielectric-enhanced intermixing is a process that has been studied extensively at McMaster University [20]. In this process, an oxide, nitride, or oxynitride film is grown on the top surface of the semiconductor. The sample is then subjected to an anneal at 700 °C to 800 °C for 30 to 120s. The material capped with the dielectric exhibits an enhanced quantum-well intermixing as compared to an uncapped sample. This is hypothesized to be due to a strain field being set up between the semiconductor and the film, which causes atoms (most likely gallium) to diffuse into the film. The resulting vacancies then diffuse through the active region and cause the intermixing. The amount of intermixing depends on the composition of the film; how it was deposited; the semiconductor structure and its doping; and the anneal temperature and time. The process developed at McMaster University involves the growth of a 1000Å oxynitride film by plasma-enhanced chemical vapour deposition (PECVD) (though films grown by electron cyclotron resonance (ECR) CVD have been examined as well). Samples are typically annealed at 750 °C to 850 °C for 30s to 120s. Shifts in excess of 100meV are easily obtainable by this process [20].

Several difficulties are encountered when using the dielectric-enhanced intermixing process. Since the magnitude of the intermixing is a strong function of the film composition, there can be significant variation from run to run, or even across the sample. This may be caused in part by the fact that amorphous oxide and nitride layers deposited on semiconductors are highly strained systems–especially during high-temperature anneals, due to the different thermal expansion coefficients of the

materials. Tight controls on the dielectric growth technique are required to obtain a reproducible result. The semiconductor-dielectric interface quality (and strain at the interface) might also play a role in the reproducibility of the intermixing process.

In some situations it is advantageous to be able to regrow over intermixed material. We have developed techniques to regrow over annealed material (which will be discussed in section 4.1.3) but we have yet to successfully regrow (by molecular beam epitaxy or MBE) over material that has been annealed while being capped with a dielectric layer. We have tried as much as 7000Å of sacrificial material in an attempt to obtain a good growth interface to no avail. (Sacrificial material was found to facilitate the regrowth over annealed material that was not capped by a dielectric as will be discussed in section 4.1.4.) Two possible reasons for the inability to regrow over dielectric-enhanced QWI material are: contamination from the dielectric layer is forced into the material by the anneal; or residual strain fields are left in the material from the anneal even after the dielectric is removed. If the dielectric is removed before the anneal, the regrowth is much more successful with the formation of many fewer defects. The source of the regrowth defects is currently being investigated.

Dielectric-enhanced QWI has an additional problem in that after annealing, the dielectric capped regions exhibit an increased etch rate as compared to uncapped regions when using the standard InP and InGaAs chemical etchants. It is not just a surface effect, and the preferential etching can still be observed 1μm below the dielectric-semiconductor interface. This can become a problem during certain device fabrication steps when fabricating integrated devices. Fabricating devices using reactive-ion etching (which could be a solution to the etching problem) has yet to be investigated. These effects severely limit the viability of the dielectric-enhanced intermixing process.

1.5.4 Sputtering Damage Enhanced Intermixing

It has been found that a sputtered SiO_2 layer can be used to enhance quantum-well intermixing [12]. In the work by Marsh et al. [12], the SiO_2 is deposited by RF sputtering. The sample is then subjected to a 550 °C to 750 °C anneal. The intermixing obtained using the sputtered films is found to occur at a much lower temperature than for PECVD films: a 100meV shift is obtainable at 700 °C. It has been hypothesized that the SiO_2 deposition damages the surface, which causes the QWI to occur at a much lower temperature. Devices with different bandgaps can be fabricated by using a 2000Å PECVD SiO_2 layer and a $2\mu m$ photoresist layer as a mask during the sputtering process. The photoresist is required since it was found that the 2000Å PECVD layer alone provided insufficient surface protection and did not inhibit the blue-shift [12].

1.5.5 Intermixing Using Low-Temperature Grown GaAs

Tsang et al. [23] found that low-temperature grown GaAs (LT-GaAs) can be used to enhance the intermixing of quantum-wells fabricated using the GaAs material system. Even though this method is only applicable to GaAs, LT-GaAs defect induced intermixing is discussed here since it is similar to the intermixing technique presented in this thesis that was developed for the InP material system: both techniques use grown-in defects to enhance the quantum-well intermixing. In LT-GaAs technique, gallium vacancies from within the LT-GaAs film have been used to enhance the quantum well intermixing process [23]. The technique used in this thesis uses vacancies generated by growing an InP layer while a He-plasma is present in the MBE chamber and is discussed in more detail in the next section and in Chapter 3.

1.5.6 He*-InP Defect Induced Intermixing

In this thesis a novel intermixing technique is developed in which the defect formed by using a Helium plasma during the growth of InP by gas source molecular beam epitaxy (GSMBE) is used to enhance the intermixing of quantum-wells. This method is discussed in detail in Chapter 3. In addition, the applicability of the intermixing technique to semiconductor devices is discussed. The project motivation is discussed in detail in the next section.

1.6 Project Motivation

This thesis examines the feasibility of using He-plasma-assisted GSMBE InP (He*-InP) to selectively enhance quantum-well intermixing. This procedure has been applied to the fabrication of DFB lasers and EA modulators to study the feasibility of the procedure for the fabrication of integrated devices.

1.6.1 Advantages of Using He*-InP

The method used in this thesis is different to most other intermixing methods in that it uses defects from a He*-InP epilayer. The only similar research is that performed by Tsang et al. [23] who use a layer of LT-GaAs as a source of defects. By using a layer of He*-InP as the source of the defects it is hoped that an improvement to the reproducibility of the intermixing process will be realized. An epilayer grown by MBE has many advantages over an amorphous layer grown by PECVD such as less strain, an improved interface quality, and a better control over the film composition. An epilayer grown by He*-plasma-assisted GSMBE does not show any measurable strain (as determined by double-crystal x-ray diffraction) and when the layer is InP, it has the same thermal expansion coefficient as the InP substrate. This

is very different from dielectric-enhanced intermixing which is a highly strained system as discussed in section 1.5.3. The InP/He*-InP interface is highly reproducible since all layers are grown consecutively within a MBE chamber. This again, is very different from the dielectric-enhanced intermixing process, where it is difficult to control the interface quality since the sample must be transferred from the MBE to a PECVD chamber, during which time a native oxide grows on the surface and the surface becomes contaminated. The reproducibility of an epilayer such as He*-InP (i.e. composition and thickness) is also much greater than an amorphous film grown by PECVD. This is extremely important for the reproducibility of the intermixing process, since dielectric-enhanced intermixing is found to be a strong function of the film stoichiometry.

There are two other major advantages of He*-InP defect induced intermixing over dielectric-enhanced intermixing. The first one is that it is possible to regrow over material intermixed by He*-InP defects, unlike material intermixed by the dielectric-enhanced intermixing defect. (This will be discussed in detail in section 4.1.4). Another major advantage of the He*-InP intermixing technique over dielectric-enhanced intermixing is that material that has been intermixed using the He*-InP defect etches at the same rate as thermally intermixed material which facilitates device fabrication.

1.6.2 Effects of Adding Recombination Centres to the Device

Helium-plasma-assisted InP-based intermixing has an interesting side-effect in that it can be used to introduce non-radiative defects into the quantum-wells. This effect is discussed further in Chapter 3, and may be useful for the development of procedures to integrate ultrafast devices that require a short carrier lifetime [24]. However, the magnitude of the reduction of the carrier lifetime due to He*-InP defect induced intermixing has not been determined in this work. The effect of adding

non-radiative defects into a device are discussed in this section.

There are four limiting factors to the speed of a device: the diffusion of carriers; the drift transit time in the depletion region; the capacitance of the depletion region, and the magnitude of the parasitic resistance [25]. Designing a device with a short carrier lifetime can reduce these limitations; hence, materials with short carrier lifetimes are used extensively in the fabrication of high-speed devices. By introducing a fast non-radiative defect into the active region of a device (such as a modulator), one addresses the problem of long carrier transit time: fast non-radiative defects act to reduce the carrier lifetime so fewer carriers are required to diffuse out of the active region of the device [24]. Using defects to decrease the carrier lifetime also acts to decrease the quantum efficiency which is detrimental for some applications (for example, photodetectors) [24]. However, for EA modulators, one does not need a high carrier collection efficiency at the contacts. Instead, EA modulators require short carrier lifetimes within the quantum-wells, since any band-filling due to the absorption of light is detrimental to device operation. Band-filling acts to decrease both the absorption by reducing the states available for absorption, and to screen the quantum-wells from the applied electric field in an effect known as absorption saturation [26]. Designing a device so that the carriers have a short lifetime within the quantum-wells can decrease band-filling effects. The increase in absorption found in these devices enable a shorter device to be used to obtain an acceptable extinction ratio for the modulator. Since the capacitance is determined by $C = \varepsilon A/d$, any reduction in the length of the device results in a reduction in the capacitance and will, therefore, result in a faster device. As well, a smaller voltage can be applied to the modulator to obtain the same increase in absorption at a given wavelength due to a reduction in carrier screening.

There are many ways to reduce the carrier escape time of quantum wells in EA modulators [27, 28, 29, 30, 31, 32]. Most techniques discussed in the literature involve designing the quantum-wells with as small an escape time as possible by using strain in the wells and the barriers. Another way is to apply a pre-bias, which decreases the carrier escape time [30]. However, a large pre-bias also causes the hole and electron wavefunctions to move to opposite sides of the quantum-well, which decreases the wave function overlap and the transition probabilities [29]. Instead of these techniques, we propose the use of non-radiative defects to decrease the carrier lifetime.

The majority of the research into device applications of fast non-radiative defects has focused on low-temperature grown gallium arsenide (LT-GaAs) or ion implanted GaAs. Some of the devices investigated include saturable absorbers for sub-picosecond mode-locking [33, 34], photoconductors [35], ultrafast (370 GHz) p-i-n photodetectors [24], electroabsorption modulators [36], ultrafast all-optical switches [37, 38], and optical gates for a pulse discriminators [39]. Recently it has been discovered that material grown by He-plasma-assisted gas-source molecular beam epitaxy (GSMBE) can also exhibit picosecond carrier lifetimes [40]. Because it is possible to fabricate devices with a 1.55μm transition wavelength, this material might prove to be extremely useful for incorporating ultrafast devices into current optical communication links. As well, the He-plasma-assisted material has been found to be capable of both inducing quantum-well mixing and introducing non-radiative defects into the quantum-wells while keeping a sharp band-edge, as will be discussed in Chapter 3. This process has the possibility of enabling the integration of high-speed devices along with standard devices, such as an EA integrated modulator and a DFB laser. The properties of the He-plasma-assisted InP will be discussed further in the Chapter 3.

1.7 Outline

This thesis discusses the development of an a novel quantum-well intermixing process which uses the He*-InP defect and demonstrates how He*-InP induced intermixing can be used to integrate an EA modulator with a DFB Laser.

Chapter 2 discusses the theory behind the operation of DFB lasers and EA modulators and includes a discussion of design considerations for both the discrete and the integrated devices.

The He*-InP intermixing process is examined in Chapter 3. It outlines the experiments used to characterize the intermixing processes and discusses the procedures used to obtain the intermixing, some of the unique properties of this intermixing method, and potential applications of the He*-InP defect intermixed material.

In Chapter 4 the fabrication techniques developed in the process of fabricating the integrated DFB laser and EA modulator is presented. These include a procedure to regrow over annealed material, a procedure to pattern DFB gratings by using a holographic system, and a method to selectively pattern a grating so that an integrated DFB and EA modulator can be fabricated.

Chapter 5 discusses the device results. This chapter includes a discussion about the properties of both the DFB laser and the EA modulator and how the two devices interact in an integrated device.

The results are summarized in Chapter 6.

Chapter 2

Device Theory

2.1 Introduction

Optical communication systems require light sources of narrow line width, high mode selectivity, high side-mode suppression, and high wavelength stability. There are many different types of semiconductor lasers with the three main ones being: 1) a Fabry-Perot laser (where the feedback is provided by the facets); 2) a distributed feedback laser (where the feedback is provided by an internal grating which runs the length of the cavity); and 3) a distributed Bragg reflector laser (where the grating acts as a Bragg mirror). Other types of semiconductor lasers are normally variations of these three. The most common device used in optical communications is the distributed feedback (DFB) semiconductor laser. It has the best compromise between ease of fabrication, good side-mode suppression, wavelength stability, and narrow linewidth [1]. A DFB laser is similar to a standard Fabry-Perot laser except that there is a periodic perturbation in either the gain, loss, or the refractive index in the cavity. This periodic perturbation causes the feedback that is required for lasing. The mode spacing, and hence the side-mode suppression, for such a laser is much greater than for a Fabry-Perot laser, thus enabling the fabrication of lasers with a single longitudinal mode [1]. The light from DFB lasers is usually modulated with an

external modulator that is either based on interference (e.g. a Mach-Zehnder modulator) or on electroabsorption [41]. Electroabsorption (EA) modulators are relatively simple to design and fabricate, and are well-suited to integrated device fabrication techniques.

The device investigated in this thesis was an integrated DFB laser and EA modulator fabricated using QWI. A schematic diagram of the cross-section of the device is illustrated in Fig. 2.1. The device consists of two sections: one containing quantum-wells with a smaller transition energy and a grating that forms the DFB laser; and one containing quantum-wells with a larger transition energy and no grating that forms the EA modulator. The large transition energy in the modulator section makes it transparent to the light from the DFB. The devices are separated by a trench which provides the electrical isolation. The focus of this chapter is DFB laser and EA

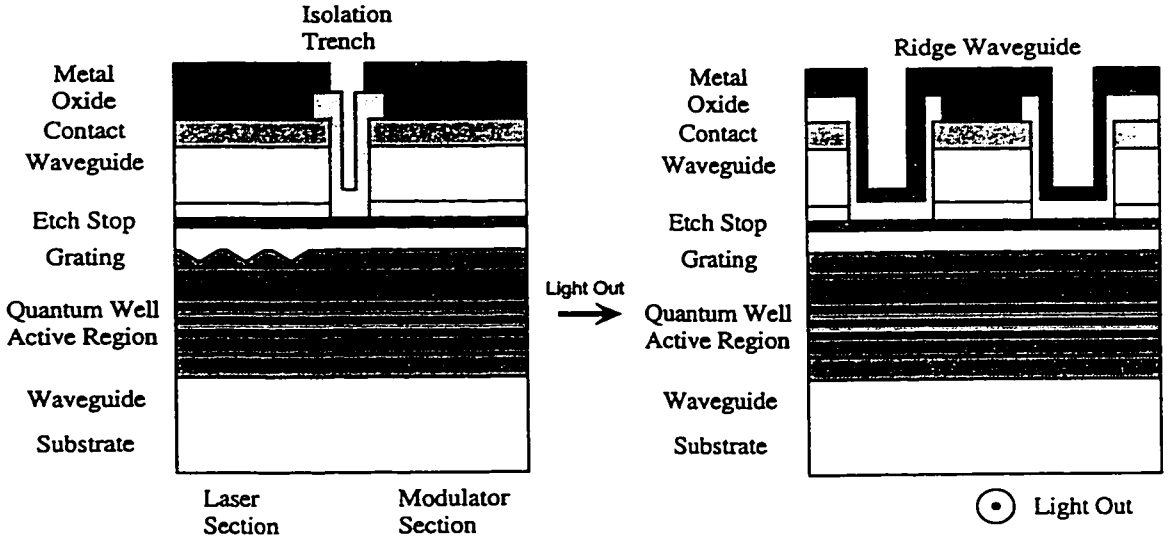

Figure 2.1: Schematic diagram of a RWG DFB laser integrated with an EA modulator showing the side and front cross-sections.

modulator theory, device fabrication techniques, and design considerations. The discussion will start with DFB lasers (section 2.2), shift to EA modulators (section 2.5),

briefly discuss antireflection coatings (section 2.7), and close with a discussion about the integrated device (section 2.8).

2.2 DFB Theory

Lasing requires optical feedback in order to achieve the light threshold needed to induce stimulated emission. In DFB lasers, the feedback is provided by Bragg reflection due to a periodic perturbation of a grating that extends throughout the device. The lasing wavelength of a DFB laser is determined primarily by the grating period and modal index of the device, and is further influenced by the grating depth, and the grating overlap with the optical mode. It can be perturbed by facet reflections, by external reflections, by the position of the gain peak, or by nonuniformities within the laser cavity.

Distributed feedback lasers do not normally lase at the Bragg wavelength of the grating. Instead, there is a local minima centered at the Bragg wavelength known as the stop-band. The modes that provide the greatest feedback are the two modes located on either side of the stop band (known as the left and right Bragg modes). The stop band and two Bragg modes can be seen in Fig. 2.2 which shows the calculated below-threshold spectrum of a index-coupled DFB laser. (The details of the calculation will be discussed in section 2.2.2.) For an index coupled laser with anti-reflection coatings (which is the simplest case to model), the lasing mode will be the mode with the greatest gain. The Bragg wavelength of a grating can be calculated using the equation:

$$\lambda_B = 2\Lambda n_0 \tag{2.1}$$

where λ_B is known as the Bragg wavelength, n_0 is the modal index, and Λ is the grating period. The modal index can be calculated by using a matrix method such

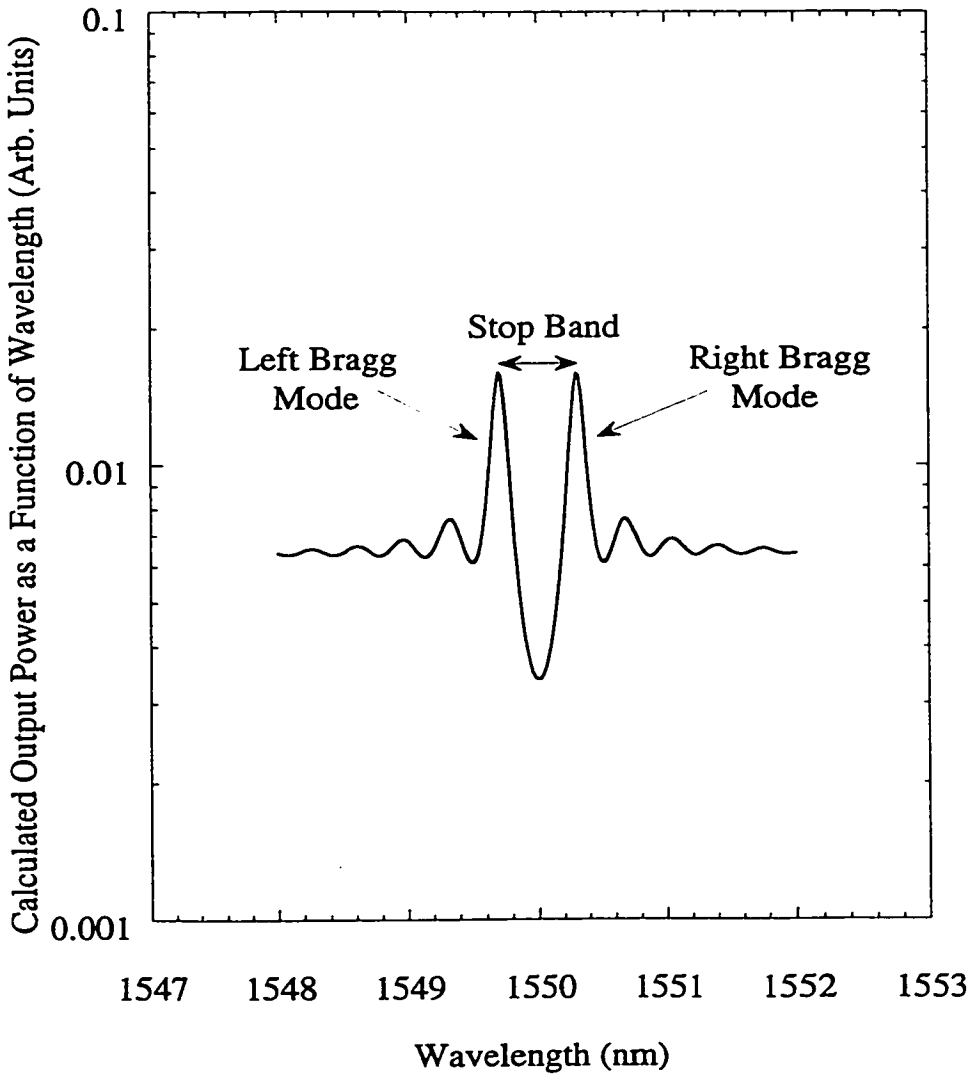

Figure 2.2: A sample calculation of a below-threshold DFB spectrum for $\kappa L = 1$ and zero facet reflectivity.

as that discussed in the appendix in section B.1. A 3-dimensional model such as the effective index method [1] is required to calculate the modal index of a laser structure. Such calculations provide a good estimate of the required grating period; however, due to uncertainties in the index for the different materials (especially strained quantum-wells), the modal index has to be experimentally determined to a

high accuracy whenever a specific lasing wavelength is required. The left and right Bragg peaks in the DFB spectrum normally occur within a couple of nanometers of the Bragg wavelength and depend on the strength of the grating. The strength of the grating is characterized by a factor known as the grating coupling coefficient and is a function of grating depth, grating shape, and grating overlap with the optical mode. To accurately determine the lasing wavelength one needs to first determine the coupling coefficient of the grating, and then use a numerical technique to calculate the spectrum [1].

2.2.1 The Coupling Coefficient

Ideal DFB laser operation requires $\kappa L \approx 1$ where κ is the coupling coefficient, and L is the length of the device. This criteria ensures a uniform photon density throughout the cavity [42] and reduces effects such as spatial hole burning. Also, if the grating is too weak and the facet reflectivities are nonzero, the device will not lase as a DFB laser. Since the coupling coefficient can vary greatly for the same grating shapes in different waveguide structures, the coupling coefficient should be calculated for a structure before trying to fabricate devices. The coupling coefficient depends on the interaction of the grating with the optical mode, so the optical mode profile must first be calculated. This calculation is normally performed using a matrix method (such as that described in section B.1) since modern semiconductor lasers contain many different layers of material and using a matrix method simplifies the calculation procedure for multilayered structures. A plot of the calculated optical mode profile for the laser structure investigated in this thesis is illustrated in Fig. 2.3. After the optical mode profile is calculated, the coupling coefficient is calculated by integrating

the optical mode over the grating perturbation:

$$\kappa = \frac{{k_0}^2}{2\beta} \frac{\int_{corrugation} A_{q\neq 0} E_y^2(x) dx}{\int E_y^2(x) dx} \tag{2.2}$$

where $E_y(x)$ is the electric field (from the optical mode profile calculation), and A_q is the qth harmonic of the Fourier coefficient of the grating (where q=1 for a first order grating) [1]. As can be seen from (2.2), the strength of the grating is dependent on the amount of overlap of the optical mode with the grating as well as the depth and shape of the grating. The calculated mode profile and coupling coefficient for the structure used in this thesis is shown in Fig. 2.3. These calculations are discussed in more detail in section B.2.

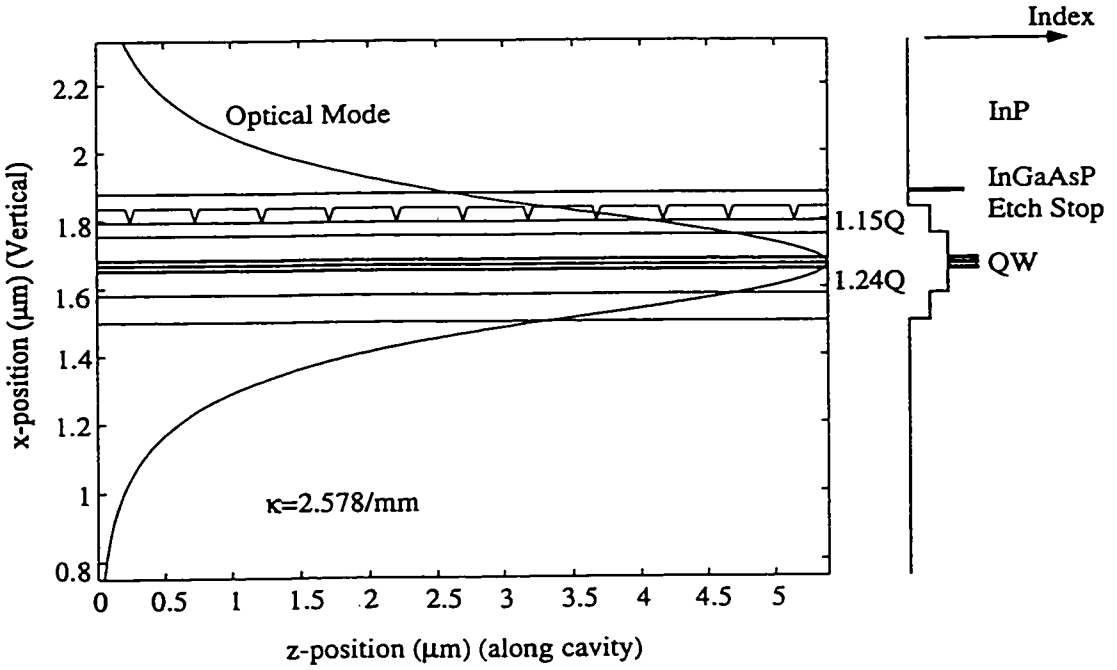

Figure 2.3: Sample mode profile and coupling coefficient for a DFB laser.

2.2.2 The Transfer Matrix Approach

There are several different methods used to calculate the output spectrum of a DFB laser. The Transfer Matrix Method (TMM) is the most common since it is very flexible. The TMM is a matrix formulation of the coupled mode solution to periodic gratings in a waveguide [1]. The matrix method allows one to model arbitrary structures and is extremely useful for investigating a structure such as a distributed Bragg reflector (DBR) laser where the grating is not uniform throughout the cavity. Another application of the TMM is in DFB laser models which takes into account non-uniform gain, carrier densities, and photon densities within the laser cavity in which the laser cavity is modeled as a series of coupled cavities with different properties (such as gain and index). A general discussion of how the optical modes of DFB lasers are calculated and details to the Transfer Matrix approach are described in section B.3.2. A sample calculation of the output spectrum of an index-coupled DFB laser (with zero facet reflectivities) was illustrated earlier in Fig. 2.2. For the calculation, a uniform gain and carrier density was assumed (i.e. a below-threshold calculation). The length was 1000μm, the facet reflectivity was set to zero, and $\kappa L = 1$ (which is the ideal case since it produces a nearly uniform photon density throughout the cavity [42]). It was also assumed that the gain and spontaneous emission was independent of wavelength. If a wavelength dependence is taken into account, one mode will experience a higher gain than the other, and the laser will lase with a single longitudinal mode. Gain (or loss) coupling will also cause the laser to lase with a single longitudinal mode.

Adding mirror reflectivities with random phases (to model cleaved facets) can act to change the wavelength of the lasing mode (the laser might start to lase at a wavelength that is within the stop-band) and affect the mode selectivity. The random

phases of the facet reflectivity is due to the random nature of the grating termination at the facet–it is impossible to cleave a laser at exactly the start of a grating period. In addition, the facets will allow for formation of Fabry-Perot fringes which will be superimposed over the spectrum caused by the grating. It is a relatively simple matter to include facet reflectivities in the Transfer Matrix model. The TMM is discussed in detail in Appendix B.

2.3 DFB Laser Design Considerations

There are several considerations that must be taken into account when designing a DFB laser. The most important is that the material (or QW) gain peak must be matched to the DFB grating. This requires accurately knowing the period of the grating, the modal index of the structure, and the position of the gain peak of the material. The period of the grating can be easily and accurately measured, as will be discussed in Chapter 4. While the modal index can be either calculated or determined experimentally (as discussed in the previous section), the calculation of the gain peak is an extremely involved process and normally needs to be determined experimentally. The gain measurement requires the fabrication of semiconductor lasers and can be measured by using a technique such as that described by Cassidy [43]. However, once the gain peak of one set of devices is measured, the gain peak can be related to the photoluminescence (PL) peak (there is a fixed relationship between the gain peak and the PL peak since they both depend on the transition energy of the quantum well). Therefore, measurements of the PL peak on an unprocessed semiconductor wafer can be used to calculate the position of the gain peak before subsequent devices are fabricated. This is extremely useful since the grating must be matched to the gain peak. For our measurement apparatus, the gain peak was at a

wavelength that was 20nm longer than the PL wavelength.[1] Normally, the gain peak is approximately 40nm wide, so if the offset between the PL peak and the gain peak is not taken into account, it is very likely that the lasers will not lase as a DFB laser at room temperature.

2.4 DFB Laser Structure

The type of laser fabricated in this thesis is a ridge-waveguide (RWG) InGaAsP quantum-well DFB laser. A cross-section of a RWG laser was illustrated earlier in Fig. 2.1. Carriers (holes) are injected through the ridge and into the quantum-wells. The ridge in a RWG semiconductor laser acts to both confine the optical mode and the injected current; thus providing both optical and carrier confinement.

The fabrication of the DFB laser is more complicated than a Fabry-Perot laser because of the grating. The DFB laser fabrication involves two growths. A sample structure used for fabricating DFB lasers is given in Fig. 2.4. This figure shows the two required growths, as well as a schematic diagram of the final structure. The initial growth includes the quantum-wells and terminates with a 250Å InP layer on top of a 1.15Q waveguide layer. The grating is etched into the InP and 1.15Q layers and then the InP is removed to leave a clean surface. A second growth completes the laser structure and includes the upper waveguide and contact. The ridge waveguide is patterned after the regrowth.

[1] This is for two reasons: 1) There is more heating when the material is electrically pumped than when it is optically pumped which causes bandgap shrinkage; and 2) the gain, $g \propto (f_c - f_v)$ while the spontaneous emission rate, $R_{spon} \propto f_c(1 - f_v)$ where f_v and f_c are the Fermi-Dirac distributions for electrons in the valence and conduction bands [3]. This results in a different wavelength dependence for g and R_{spon} with R_{spon} peaking at a shorter wavelength.

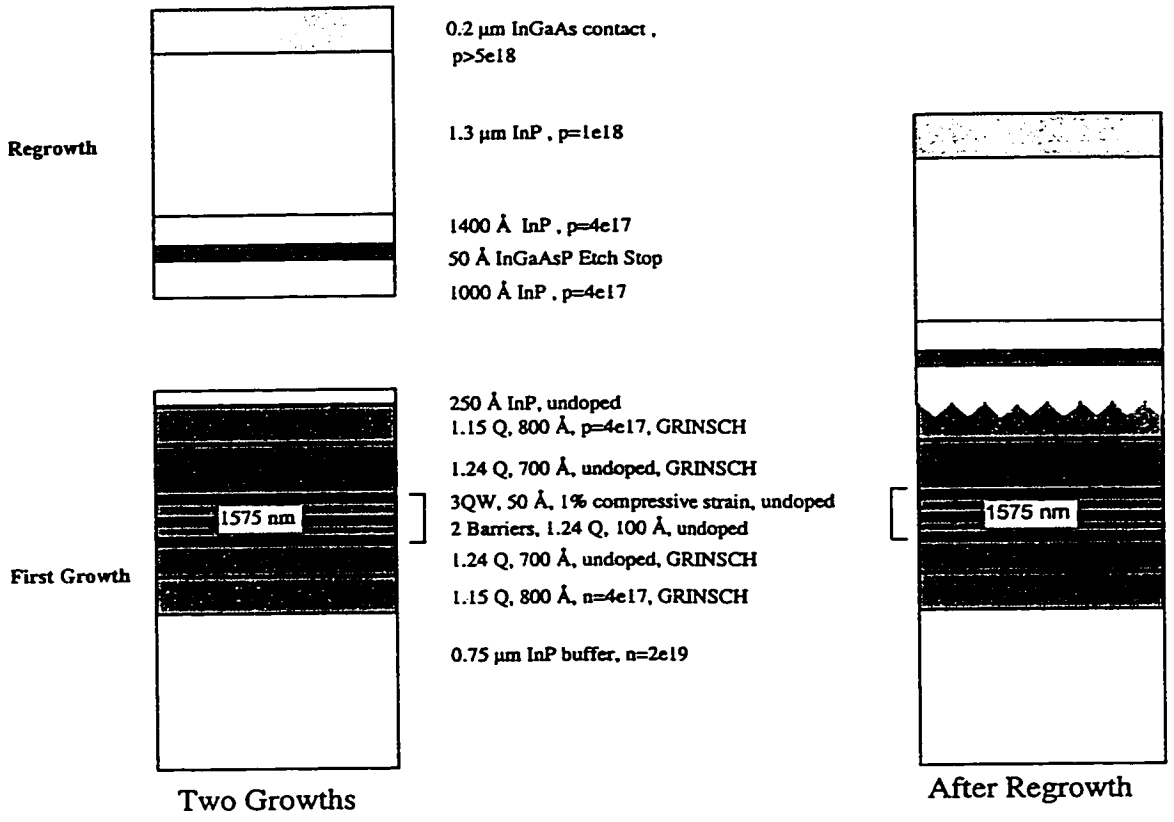

Figure 2.4: Schematics of a typical structure used for fabricating a DFB laser showing the two required growths and the completed structure.

2.5 Electroabsorption Modulator Theory

The light from a DFB laser needs to be modulated to transmit information. The EA modulator is one type of modulator used by the telecommunications industry. There are two broad categories of EA modulators: one that is normally off (absorbing) and a bias is applied to make it transparent; and the other is normally on (transparent) and a bias is applied to make it absorbing. Any effect that changes the absorption of a semiconductor material can be used: carrier injection can be used to decrease the material absorption; or the Franz-Keldysh effect (in bulk semiconductors) or the quantum-confined Stark effect (for quantum-wells) can be used to increase the

material absorption at certain wavelengths. However, due to the potential for large shifts in the absorption band edge, the most common semiconductor EA modulator is based on the quantum-confined Stark effect (QCSE) [6].

The QCSE is caused by the distortion experienced by a QW due to the application of an electric field. This distortion has a large effect on the electron transition energy [44]. An example of the effect of an electric field on the calculated transition energy of a quantum-well and the electron and hole wavefunction is illustrated in Fig. 2.5. Notice how both the quantum-wells and the wavefunctions are distorted by the application of the electric field. It is the distortion of the quantum-well that causes the large decrease in the transition energy. The effect on the electron transition energy is much larger than the Franz-Keldysh effect seen in bulk materials; hence, quantum-wells are used whenever large changes in the band edge are required. A p-i-n diode structure (with the quantum wells in the intrinsic region) is normally used to ensure most of the reverse-bias voltage drop is across the quantum-wells. To implement a modulator based on the QCSE, the absorption edge of the modulator must be at a shorter wavelength than the wavelength of the incoming light. A reverse bias is then applied to increase the absorption at the input wavelength; hence, the bias switches the modulator to the "off" state. Replacing a bulk absorbing material with quantum-wells has several other effects that should be mentioned: the density of states is modified and the absorption edge is sharpened [45], the exciton binding energy is increased so that excitons are present in the absorption spectrum even at room temperature which acts to further sharpen the band edge [44].

One way to fabricate QCSE EA modulators with an absorption edge at a shorter wavelength than that of an integrated laser is to use a method of quantum-well intermixing. This is the technique used in this thesis and will be discussed in detail

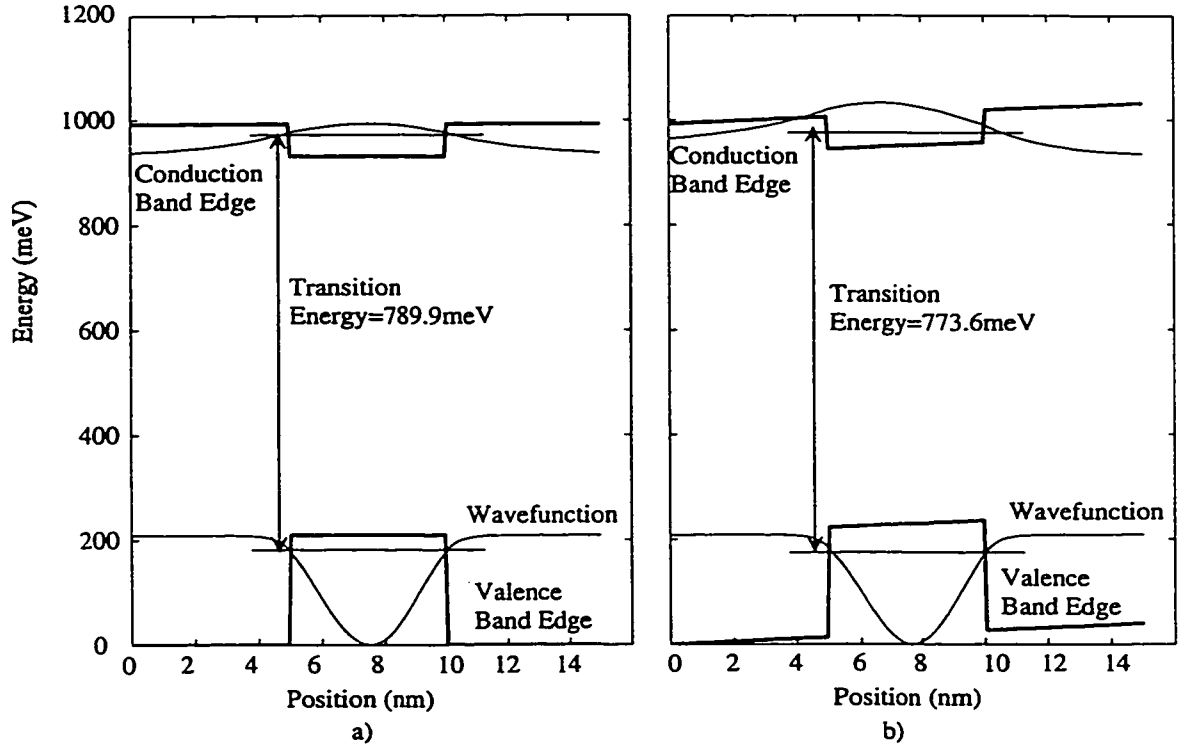

Figure 2.5: Transition energy of a quantum well for a) with no field, and b) with an applied electric field. The thin lines are the electron and hole wavefunctions, while the thick lines are the quantum well profiles.

in Chapter 3. Intermixing the quantum-wells has been shown to modify the QCSE: the wavelength shift in the absorption spectrum for a given voltage is greater for an intermixed quantum-well than for a quantum-well that is not intermixed [13]. Also intermixed quantum-wells can be designed to have an equal bias-dependent absorption for both TE and TM polarizations [46]. These effects were not investigated in this thesis.

2.6 EA Modulator Design Considerations

There are several design considerations for EA modulators. The extinction ratio (for a given applied voltage) is a common figure of merit for modulators and is defined as the ratio of output power between the "on" and "off" states (normally quoted in dB). Generally, one would like as high an extinction ratio as possible. However, a compromise is often made between the extinction ratio and the operating voltage of the modulator. This is because a modulator with an absorption edge far from the lasing wavelength will have a high extinction ratio but will also require a high operating voltage. An extinction ratio of ~12dB is normally required by industry.

The total absorption of a EA modulator depends not only on the absorption of the quantum-wells, but also on the overlap of the optical mode with the quantum-wells (known as the optical confinement factor). In an ideal EA modulator, the barriers and waveguide are not absorbing at the lasing wavelength so the majority of the absorption is taking place in the quantum wells. Therefore, to increase the absorption of the modulator one needs to increase the interaction of the optical mode with the quantum wells. To do this, one can either modify the waveguide to increase the optical confinement (different waveguide geometries have different confinement factors), increase the number of quantum wells, or increase the length of the modulator. There are limits to each of these techniques. Increasing the optical confinement (without increasing the size of the active region) makes it more difficult to couple light in and out of the waveguide, and there are limits as to how much one can increase the optical confinement in the InGaAsP material system (due to the index of the material). Increasing the length of the modulator also increases the capacitance, which is detrimental to the modulation characteristics of the device. Increasing the number of quantum wells increases the thickness of the intrinsic region in the p-i-n diode which

acts to decrease the device capacitance. However, the increased thickness of the intrinsic region also has detrimental effects: it results in a reduction in the electric field seen by each quantum-well for a given applied voltage (since the electric field in the intrinsic region of a p-i-n diode is given by $E = V/d$ where V is the voltage applied across the intrinsic region, and d is the intrinsic region width); hence a higher voltage is required to obtain the same wavelength shift in the absorption spectrum [6, 45, 30].

Insertion loss must also be considered when designing an EA modulator. The insertion loss includes all losses in the modulator when it is in the non-absorbing state: waveguide losses due to roughness, etc.; residual absorption of the waveguide layers; residual absorption of the quantum-wells when the modulator is in the "on" state; and transmission losses due to facet reflectivities. Coupling losses associated with coupling light in and out of a modulator can also be a problem, but are not normally included in the discussion of insertion losses. (Coupling losses can be minimized by device integration techniques.) There are several methods whereby the insertion loss can be minimized. Waveguide losses can be minimized by optimizing the processing procedure (i.e. ensuring a smooth waveguide) and by the proper selection of waveguide materials. The residual absorption of the quantum-wells is usually due to the compromise required between having a large extinction ratio and a small turn-off voltage (as discussed earlier), so there is a limit as to how much this absorption loss can be minimized. The effect of the facet reflectivities can be eliminated by using anti-reflection coatings or by using device integration techniques to eliminate the facets altogether.

2.7 Anti-Reflection Coatings

Designing an anti-reflection (AR) coating for a semiconductor laser is not an easy task. For the coating design, one must take into account the modal index of the structure as well as the fact that the beam exiting the facet will be highly diverging and a new coating must be developed for each different laser structure [47]. Usually an iterative process is required to obtain the desired reflectivity.

The general procedure for characterizing an antireflection coating involves examining the below-threshold spectrum of a Fabry-Perot laser from which it is a relatively straight-forward matter to calculate the reflectivity-gain (RG) product [43]. After coating, the new RG term can be calculated. If the laser is at the same bias point, the gain will be the same, so the change in reflectivity can be calculated by taking the ratio between the two RG products.

2.8 Integrated DFB and EA Modulator

The integrated device in this thesis combines the DFB laser and EA modulator and the design considerations for fabricating an integrated device will be discussed in this section. A schematic diagram of the structure was illustrated in Fig. 2.1. The structure used was a RWG laser structure due to its good compromise between ease of fabrication and its good device characteristics (i.e. low threshold, high external efficiency). For these reasons, it is also used extensively in industry. Some of the shortcomings of such a structure for use in an integrated device will also be discussed in this section.

2.8.1 Laser and Modulator Transition Energies

An integrated DFB laser and EA modulator is comprised of two sections. One section that forms the DFB laser contains quantum-wells of one transition energy and a grating. The second section forms the EA modulator and contains quantum-wells with a larger transition energy than the laser section and no grating. Therefore, to fabricate such a device, the transition energy of the modulator must be increased with respect to the laser section to make it transparent to the lasing wavelength, and the grating must be patterned in the laser section only.

As discussed in Chapter 1, one of the easiest ways to modify the transition energy in a quantum-well is by using QWI. For proper device operation, a 25-50nm difference between PL in the laser and modulator section is required with the laser at the longer wavelength (corresponding to a difference in the QW transition energy of the devices). The difference of the transition energies of the QWs in the two sections will affect the voltage required to obtain a specific absorption and extinction ratio of the modulator (i.e. for a larger PL peak separation a larger extinction ratio is possible but a higher voltage is required to obtain the same extinction ratio). The PL peak separation is quoted because PL is easy to measure than the gain peak or absorption edge of a QW. However, the peak PL wavelength is not really the parameter of interest–the device operation depends on the lasing wavelength of the laser, and the absorption edge of the modulator. The value of 25-50nm peak PL wavelength difference is if the laser is lasing at the gain peak. The grating provides us with an additional degree of freedom and the tolerance can be loosened slightly since it is not necessary to perfectly match the grating to the gain peak (i.e. if the grating is $\pm$10nm from the gain peak, it will still lase as a DFB at room temperature).

2.8.2 Device Isolation

Device isolation is critical to proper device operation. Care must be taken to ensure that the modulator section is not perturbing the laser section either optically or electrically. Good isolation can be verified by examining the light-current (L-I) curves of the integrated device for different modulator biases. In the ideal case with perfect isolation, the L-I curve out of the laser facet would be unaffected by the bias on the modulator section. In addition, the L-I curve measured from the modulator facet should show a constant threshold current, but a different external differential efficiency measured from the modulator facet for each modulator bias. If not, additional care must be taken in interpreting the results. There are two types of isolation required: electrical and optical.

Electrical isolation is required for proper device operation. A lack of electrical isolation causes a change in the laser bias point as the modulator section is modulated. This can lead to an additional amplitude modulation and frequency modulation of the output light. Therefore the resistance between the laser and modulator should be significantly greater than the modulator resistance. (The laser resistance is small in comparison.) Device isolation is obtained by etching a trench through the top highly doped InGaAs and InP layers (i.e. a depth equivalent to the ridge height as illustrated in 2.1). This trench increases the resistance between the two devices. One problem with using isolation trenches with ridge waveguide lasers is that a trench greatly decreases the amount of optical coupling between the devices so a compromise must be made between good optical coupling and good electrical isolation. However, a small reduction in the optical coupling can actually improve the device performance by reducing the amount of optical feedback reaching the laser.

Optical feedback reaching the laser can cause kinks in the L-I curves, mode

hopping, and an increase in the measured dynamic chirp. If reflections from outside the cavity are eliminated, the main source of optical feedback is from the modulator facet. Optical feedback from the modulator facet needs to be minimized because the amount of feedback reaching the laser depends on the bias of the modulator, and any change in the amount of feedback reaching the laser will affect both the laser's output power and output wavelength. (Note that approximately 2% of the light traveling from the laser to the modulator will be reflected by the isolation trench which will not affect the integrated device operation since it is independent of modulator bias.) An AR coating on the modulator facet is one method that can be used to reduce this optical feedback. The isolation trench can also be used to decrease the amount of optical feedback reaching the laser by decreasing the optical coupling between the cavities. For the laser structure investigated, the coupling between the two cavities is approximately 60% (with the remaining light being lost to the optical mode and reflected into the substrate) and is dependent on both the ridge width and trench length as calculated by the Beam Propagation Method [48]. Therefore, any light reflected by the facet will be attenuated by more than 64% (plus any losses associated with absorption in the modulator) before entering the laser.

Chapter 3

Quantum Well Intermixing Using the He*-InP Defect

3.1 Introduction

The semiconductor industry is interested in integrating various optoelectronic devices, such as lasers, waveguides, modulators, and detectors on a single wafer. Different device integration techniques used have been discussed in detail in Chapter 1. The technique that has the best compromise between simplicity and flexibility is quantum-well intermixing (QWI) in which the electron transition energy is selectively changed by intermixing quantum-wells and barriers after the growth has been completed. A novel method for QWI using helium-plasma-assisted GSMBE grown InP is discussed in this chapter along with some of the advantages over the more widely studied process involving a dielectric cap and a rapid thermal anneal (RTA) treatment.

3.2 Quantum Well Intermixing Experiments

Most QWI techniques involve defects which act to selectively enhance the intermixing between adjacent QWs and barriers during a RTA. However, there is a

significant amount of intermixing due solely to the RTA treatment. When a sample containing quantum wells fabricated from standard InP and InGaAsP is annealed at temperatures greater than about 500 °C, the peak wavelength of the photoluminescence from the quantum-wells exhibits a shift to a higher energy [20]. This shift is referred to as the thermal blue-shift. There is currently uncertainty as to the source of the thermal blue-shift. Possible explanations are: defects migrating from the air/semiconductor interface; defect migration from the substrate and the initial growth/substrate interface; diffusion of native defects within the as-grown epilayers; removal of QW inhomogeneities; or some type of strain-enhanced diffusion caused by the different thermal-expansion coefficients of the various materials comprising the structure. This thermal blue-shift must be compensated for when designing devices with gratings since the gain peak of the material must match the grating.

One of the more common intermixing techniques is known as dielectric-enhanced QWI, which has been investigated in detail at McMaster University [20]. If the sample is coated with a plasma-enhanced chemical-vapour-deposition (PECVD) SiO_xN_y film, the blue-shift can be enhanced for anneal temperatures greater than about 750 °C. This intermixing accompanies the thermal blue-shift and is assumed to be the result of a different process. Both the thermal and dielectric-enhanced intermixing have been observed in MBE and metal-organic chemical-vapour-deposition (MOCVD) grown materials. The amount of intermixing depends on the semiconductor structure and its doping, the composition of the dielectric film, and the method of film deposition. Also, the source of the dielectric-enhanced shift is unclear, though it is generally assumed that gallium diffuses into the dielectric and that the resulting group III vacancies diffuse from the surface and through the quantum-wells, resulting in enhanced intermixing between the wells and the barriers.

Dielectric-enhanced QWI involves the introduction of defects at the surface of the semiconductor structure. Alternatively, defects can be grown in the material. One way to incorporate substantial numbers of defects into an InP or InGaAsP epilayer that was developed at McMaster University is by igniting a electron cyclotron resonance (ECR) helium-plasma during a growth by gas source molecular beam epitaxy (GSMBE) [49]. The resulting material is highly resistive, is optically fast (i.e. it has a short carrier lifetime), and has a sharp band edge [40] that can be tuned to a particular application in the case of InGaAsP (i.e. the composition of $In_{(1-x)}Ga_xAs_yP_{(1-y)}$ can be controlled to produce a bandgap compatible with the 1.55μm wavelength of light used in optical communications). One possible explanation for the material's unique properties is that the impact of the He-plasma particles cause damage leading to multiple defects with energy levels within the band gap–one of which is a deep and optically fast level [49]. Despite large changes in the electrical and optical properties, the samples exhibit no measurable strain and no change in the surface morphology as determined by double-crystal x-ray diffraction and optical microscopy [49]. Previous research with this material has interested research groups working at developing ultrafast switches, modulators, detectors, and saturable absorbers. Ultrafast device research, until the discovery of the helium-plasma material, had focused on using low-temperature, MBE-grown GaAs [50] which is not an ideal material for optical communication systems due to its large bandgap. Helium-plasma-assisted InP and InGaAsP are much more suited for optical communications applications.

When the He*-InP material is annealed at temperatures greater than ~500 °C, both the resistivity and the carrier lifetime of an undoped sample increase with increasing anneal temperature [49]. From these results it has been concluded that annealing causes the defects to annihilate, cluster, or migrate out of a semiconductor

layer grown by helium-plasma-assisted epitaxy and into the substrate [49]. How these defects interact with quantum wells and the defects associated with thermally induced QWI is of great interest since it might provide additional insight into the types of defects involved. Also, if the non-radiative defect is mobile, there is the potential for fabricating ultrafast devices with short carrier lifetimes, and integrating them with other devices. Ultimately, it would be useful to integrate different types of devices, such as lasers or waveguides with ultrafast modulators or detectors. The annealing characteristics of the He*-InP defect were investigated and the results are discussed in the following sections.

3.3 Intermixing Experiments Using He*-InP

The structures investigated in this chapter were grown by GSMBE. They are based on standard truncated laser structures with similar doping and band profiles. He-plasma-assisted epitaxy is identical to the standard GSMBE growth techniques used at McMaster University, except that during the growth the sample surface is exposed to a flux of He particles from an ECR source. Typical gas flows to the ECR source are 5-10 sccm and the absorbed power is 100-150W at 2.45GHz. The average energy of the plasma particles is approximately 25eV [49]. The growth temperature is typically 450-460 °C; i.e. our normal growth temperature for phosphorus containing epitaxial layers. [51]

The annealing of the samples to be intermixed was performed in a nitrogen atmosphere in a rapid thermal anneal (RTA) furnace. The temperature was ramped at 100 °C/s during the heating cycle. The samples were placed face down on a GaAs wafer and capped with another GaAs wafer to protect the surface during the anneal. After annealing, the top InGaAs and InP layers were etched off to improve the pho-

toluminescence (PL) signal from the quantum-wells. To minimize errors caused by material variation across the wafer, only samples taken from the centre of the wafer were used. As well, several unannealed samples taken from random places on the wafer were measured and were found to have PL peaks within 2nm of each other. Anneal temperature variations were minimized by annealing all the samples for each temperature at the same time.

3.4 Intermixing Results

3.4.1 Experiment 1

The He*-InP material is known to contain large numbers of vacancy type defects that appear to agglomerate on anneal [49], so it was decided to investigate whether a layer of such material could inhibit QWI by trapping or annihilating with any defects that diffused from the top surface, top InGaAs layer, from the substrate, and from the substrate/growth interface in a truncated multiple-quantum-well (MQW) laser sample. To this end, two truncated laser structures were produced in consecutive MBE growths: a standard MQW laser structure, and the same laser structure containing layers of He*-InP inserted above and below the QW active region (see Fig. 3.1). Hence, in the latter case, the region containing the quantum-wells was isolated from the surface and the substrate and growth interface by InP layers containing a large concentration of vacancy type defects.

The samples were annealed at temperatures ranging from 550 °C to 700 °C for 10s. The room-temperature PL (RTPL) results are illustrated in Fig. 3.2, with the upper curve representing the sample without the He*-InP layers, and the lower curve representing the sample with the He*-InP layers. The PL intensity increases with anneal temperature for the sample without the He*-InP layers, while the PL

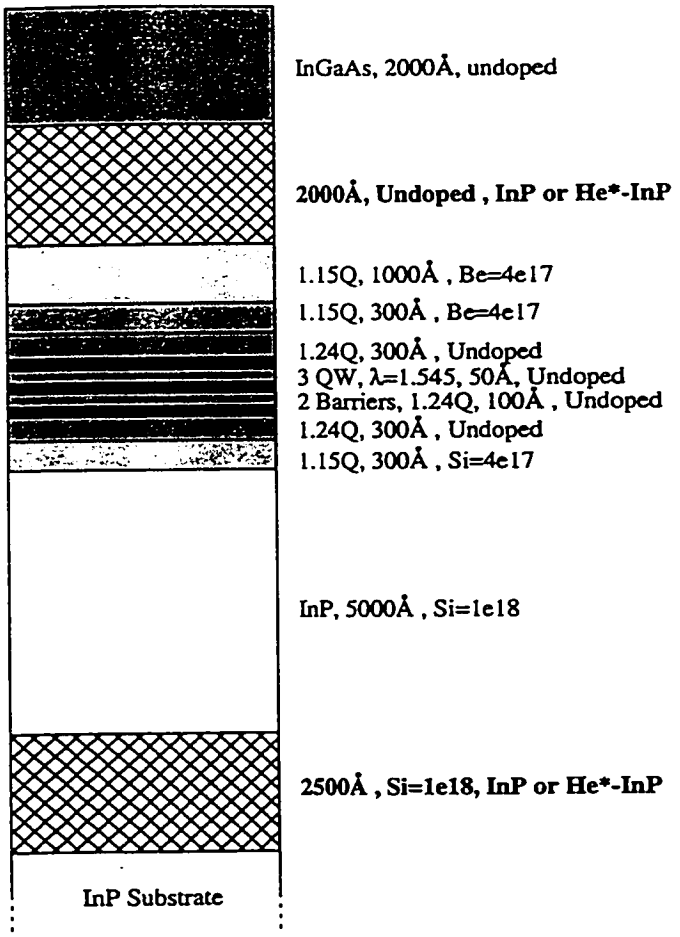

Figure 3.1: Structure diagram for experiment 1.

intensity decreases with anneal temperature for the sample with the He*-InP layers as shown on the graph. The error associated with measuring the PL peak (due to the width of the peak at room temperature) is ±2nm, which makes the error in the measured blue-shift ±3nm. (Error bars are left off the graph for clarity.) As can be clearly seen from this plot (by the reduction in the blue-shift in the sample with the He*-InP layer), the He*-InP layer inhibits the thermal blue-shift. This suggests that a component of the thermal blue-shift is caused by defects migrating from either the

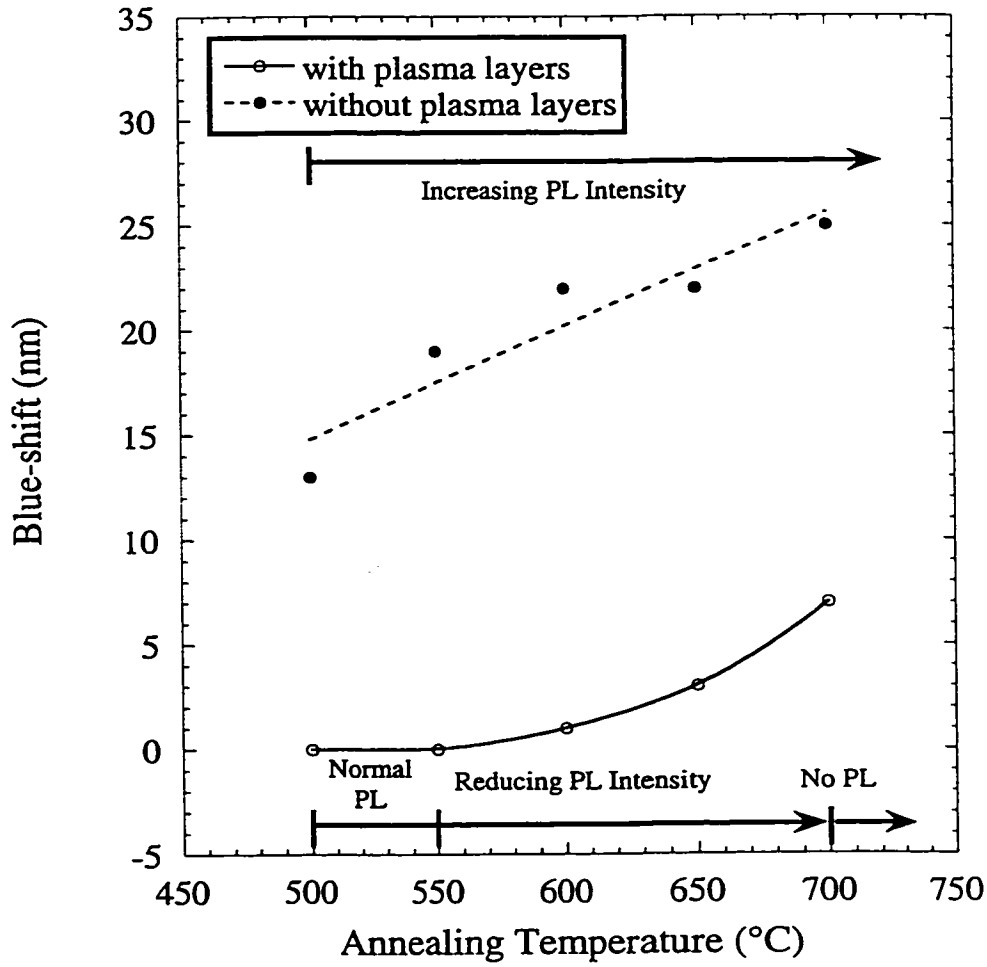

Figure 3.2: Variation of blue-shift with anneal temperature for samples with and without the He*-InP layers (measured using RTPL). The anneal time was 10 sec.

InGaAs top contact layer, the growth interface, or the substrate, which then become trapped in the He*-InP layers. Also, samples containing the He*-InP layers showed a reduction in PL intensity with increasing anneal temperature (as compared to an unannealed sample), and for anneal temperatures greater than 700 °C there was no measurable RTPL. This contrasts with the PL from the standard samples (without the He-plasma), which show a slight increase in the PL intensity with increasing

anneal temperature. A schematic diagram of the defects involved is illustrated in 3.3. Figure 3.2 also shows the onset of QWI in the sample containing He*-InP at anneal temperatures greater than 550 °C which is the same temperature at which the PL intensity starts to drop off. This result suggests that the defect that is causing the reduction in the PL signal is the same one that is causing the QWI. This hypothesis will be examined further in section 3.4.2.

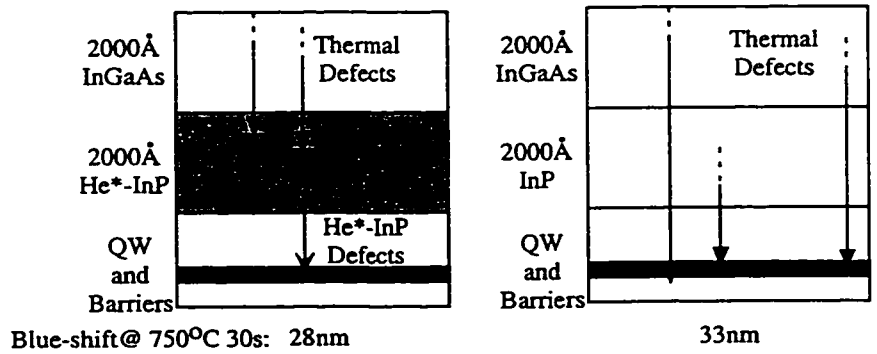

Figure 3.3: Schematic diagram of the source of the defects causing the intermixing for the samples in experiment 1. (Blue-shift values quoted are for a 750 °C, 30s anneal.)

Three other material intermixing properties were briefly examined: the effect of etching the top He*-InP layer to obtain an idea of the diffusion length of the defects contained within the He*-InP layer; the effect of annealing at temperatures greater than 700 °C (examined using 15K photoluminescence); and the effect of capping the sample with a PECVD film to see if the dielectric-enhanced shift is modified. After the top He*-InP layer was removed by etching and the sample was annealed at 750 °C, no reduction in the PL intensity was observed. This suggests that the diffusion length of the defect that is responsible for reducing the PL is sufficiently short that the defects from the bottom He*-InP layer (which is 5000Å below the active layer) are unable to diffuse to the quantum-wells. Thus the He*-InP defect is a more slowly diffusing defect than that observed in dielectric-enhanced QWI. Also, the peak PL wavelength

of the sample with He*-InP layer was only 3nm less than that of the sample without the He*-InP layer which suggest that if defects are migrating from the substrate, the He*-InP layer is not effective at blocking them. A sample annealed at 750 °C for 30s was measured using low-temperature PL (LTPL). After this anneal, there is no measurable RTPL, but it is possible to see a weak PL signal when measured at 15K. At this temperature, the sample without the He*-InP showed a 33nm(±2nm) blue-shift while the He*-InP sample showed a 28nm(±2nm) blue shift with respect to the unannealed sample (producing a relative blue shift of -5nm(±3nm)). The PL signal of the He*-InP sample 0.017mV, and the signal from the sample without the He*-InP layer was 5.4mV. (The measured voltage is proportional to the power incident on the detector since a transimpedance amplifier is used.) This makes the PL signal from the He*-InP sample ~1/300th the intensity of the PL signal from the non-He*-InP sample. (However it should be noted that care must be used in interpreting these results since the apparatus was not designed to make quantitative PL intensity measurements. The error is estimated at 10%.) As will be shown in the next section, this result is quite different from the result obtained by using a thinner He*-InP layer. The effects of coating the sample with a CVD SiO_xN_y film were also briefly examined to investigate whether the He*-InP layer affects the dielectric-enhanced QWI. (The films used were a 1000Å SiO_xN_y film deposited by PECVD and have an index of 1.56.) Comparisons of He*-InP samples with and without dielectric caps have shown the PL spectra to be nearly identical. Since the enhanced blue-shift due to capping the sample with a dielectric is eliminated, these preliminary results show that the $0.2\mu m$ He*-InP layer completely blocks the defects responsible for the dielectric-enhanced blue-shift.

Further experiments were needed to determine unequivocally the source of the

intermixing in the sample with He*-InP layers; i.e. whether it is from the He*-InP layer, surface defects diffusing through the He*-InP layer, or grown-in defects. From the reduction in the PL signal, one can conclude that the He*-InP defects are mobile; therefore it is likely that the remaining blue-shift is caused by the He*-InP defects as they migrate through the QWs. If so, this defect migration might prove to be extremely useful in integrating ultrafast devices incorporating the "fast" He*-InP defect with waveguides and other semiconductor devices. However, after this first investigation, it appeared that He*-InP defect diffusion had limited use for integrated device applications. This is because for the anneal temperatures investigated, samples containing the He*-InP layer resulted in a suppressed intermixing as well as a reduction in the carrier lifetime. Diffusing the He*-InP defect into quantum-wells might prove to be a good method for fabricating fast photodetectors or saturable absorbers, but many other intermixing applications (such as when fabricating an integrated DFB and electroabsorption modulator) require one section to have both an enhanced QWI and a reduced carrier lifetime. (Intermixing requirements were discussed in detail in section 2.8.1.) If He*-InP was to prove useful for device integration, there are two options: investigate methods to enhance the QWI in the section with the reduced carrier lifetime; or focus on using the He*-InP layer to suppress the intermixing and investigate methods to prevent the He*-InP defect from diffusing into the quantum-wells. These two options were investigated in the next experiment.

3.4.2 Experiment 2

The purpose of this second experiment was threefold: to study whether the intermixing seen in the He*-InP sample in experiment 1 was due to defects from the He*-InP layer or from defects migrating through the He*-InP layer; to investigate whether a He*-InP layer far away from the quantum-wells can be used to suppress

the intermixing without reducing the carrier lifetime; and to see whether a thinner He*-InP layer has the same effect as a 2000Å He*-InP layer.

To this end, the structure illustrated in Fig. 3.4 was grown. Sample A has two He*-InP layers, while sample B has only the top He*-InP layer. The lower He*-InP layer in sample A was grown to examine the He-plasma defect further. A 400Å layer was used instead of a 2000Å layer to see if the thinner He*-InP layer still blocks defects migrating from the top surface. Sample B was an equivalent structure with the He*-InP layer replaced with a normal InP layer. The top He*-InP layers in both A and B were an attempt to inhibit the thermal blue-shift; hence the upper He*-InP layer was placed a distance from the quantum-wells that was greater than the estimated diffusion length of the defects. Also, in subsequent experiments at McMaster University, it has been found that an InGaAs layer as thin as 200Å blocks the migration of the He*-InP defect.

Four samples were annealed at 700 °C, 750 °C, and 800 °C: samples A and B were processed as grown, and A_E and B_E were processed with the top He*-InP layer etched off. The LTPL results are shown in Fig. 3.5 and Fig. 3.6. The error in the blue-shift is ±2nm. The error in the measured voltage is estimated to be 10% (although the system was not designed to make quantitative PL intensity measurements). The lines are not meant to suggest that there is a linear relationship between blue-shift (or voltage) and temperature, but are there as an aid to help illustrate the trends. More data points are required before any conclusions can be drawn about how the intermixing varies with anneal temperature (i.e. whether the relationship is exponential, linear, etc.). From the data, some of the results seen in experiment 1 are verified: the samples with the He*-InP near the quantum-wells (A and A_E) exhibited a reduction in the PL signal. However, the LTPL was only reduced by ap-

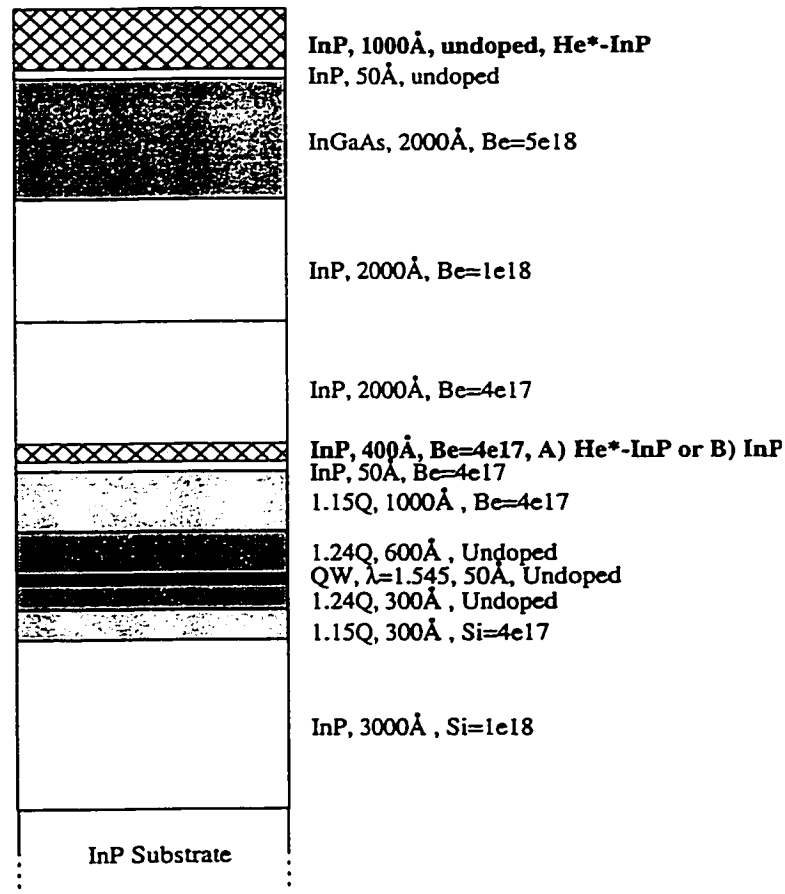

Figure 3.4: Structure diagram for experiment 2. Sample A has an upper and lower He*-InP layer, while sample B has only the top He*-InP layer.

proximately an order of magnitude for a 750 °C, 30s anneal. In contrast, the sample shown in Fig 3.1 (with the 2000Å He*-InP layer) showed greater than a two order of magnitude decrease in the PL intensity when annealed under the same conditions (as discussed in the previous section). This difference is attributed to the fact that due to the thinner He*-InP defect source layer, fewer defects were available to migrate to the QWs in the new structure.

Several other conclusions can be drawn from the four curves in Fig. 3.5 and Fig. 3.6. As summarized in table 3.1, the sample with only the lower He*-InP layer

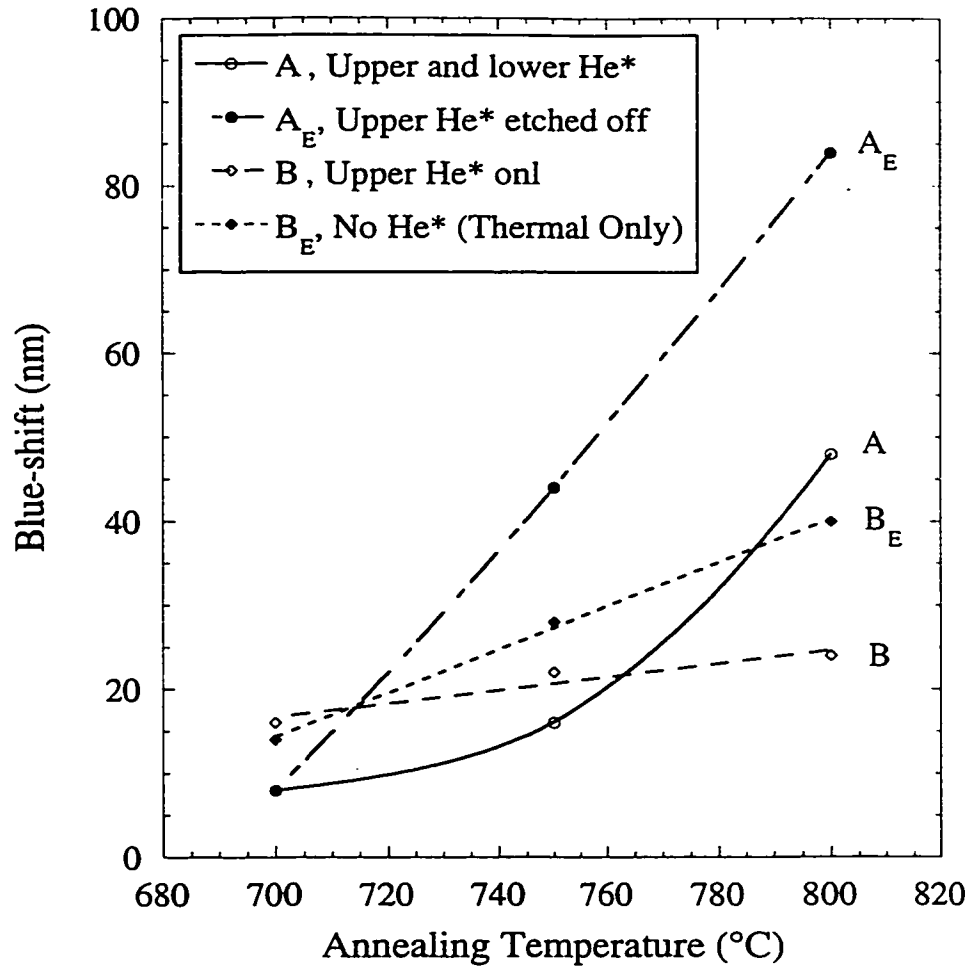

Figure 3.5: Variation of blue-shift with anneal temperature for samples with and without He*-InP defects (measured using LTPL). The anneal time was 30 sec.

(A_E) showed the greatest blue-shift, while the sample with both the upper and lower He*-InP layer (A) showed significantly less QWI, and the sample with only the upper He*-InP layer showed the least amount of intermixing (for an anneal temperature 800 °C). Only the samples with the lower He*-InP layer showed a reduction in the PL signal which once again confirms that the He*-InP defect has a short diffusion length. A schematic diagram of the sources of intermixing for each of the samples is illustrated

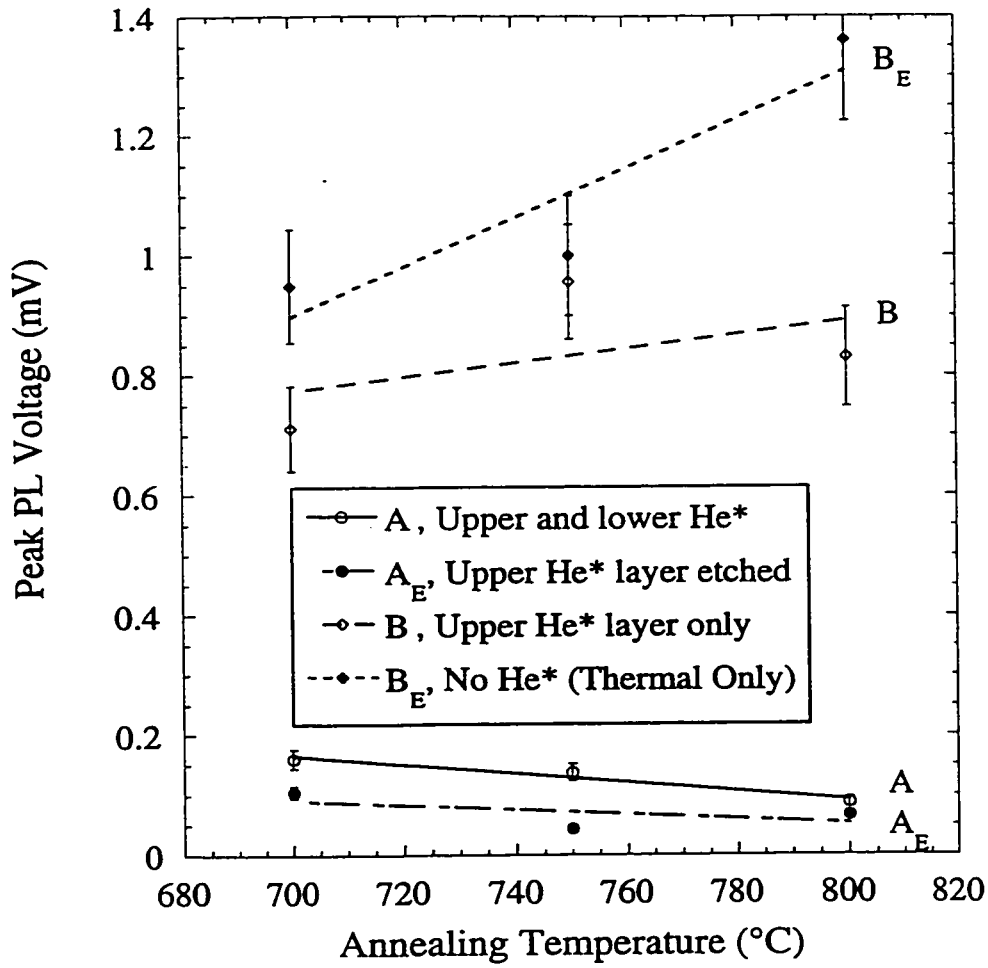

Figure 3.6: Variation of Low-temperature (15K) PL voltage with anneal temperature for samples with and without He* defects. The anneal time was 30 sec.

in Fig 3.7. The fact that the samples with the top He*-InP show a reduced amount of intermixing (samples A and B) as compared to the samples without (samples A_E and B_E) suggests that the top 1000Å He*-InP layer stops defects generated at the top surface from migrating to the QW region. Also, the sample with only the lower He*-InP layer (sample A_E) exhibits a greater amount of intermixing than the sample without any He*-InP (sample B_E), suggesting that the lower layer contributes

Sample Number	Blue Shift (±2nm)	PL Intensity (arb. units)(±10%)	Possible Main Source of Intermixing
A	48nm	0.086	Lower He*-InP
A_E	84nm	0.066	Lower He*-InP and Thermal
B	24nm	0.83	Reduced Thermal
B_E	40nm	1.36	Thermal Only

Table 3.1: Summary of PL data for the samples from experiment 2 annealed at 800 °Cfor 30 sec. The hypothesized source of the majority of the intermixing is also given for each sample. Sample A has the 2 He*-InP layers, while sample B has only the upper He*-InP layer.

defects that enhance the QWI. (Note that as much as 10nm of the blue shift difference between the etched and non-etched samples can be attributed to the different material at the surface –a sample with an InP top layer has been known to show a slightly less thermal blue shift than one with an InGaAs top layer.) The anneal results at 800 °C and the hypothesized sources of the majority of the intermixing in each of the samples are summarized in table 3.1.

One further experiment was also performed: it was found that if a dielectric was grown on the top surface of the samples with an InGaAs top layer (sample A_E), the QWI under the dielectric capped regions was less than that found for either a dielectric coated sample without the He*-InP layers (i.e. sample B_E with a dielectric cap) or a sample with the lower He*-InP layer and no dielectric cap (i.e. sample A_E, uncapped). Also, in contrast to sample A_E without a dielectric cap, the PL for sample A_E with a dielectric cap shows an increase in the PL signal after a 800 °C anneal as compared to a 750 °C anneal. This suggests that the defects in the He*-InP layer and the defects caused by the dielectric are annihilating each other. This results is consistent with the hypothesis that the main He*-InP defect is a phosphorus vacancy [51], and that the dielectric-enhanced intermixing is caused by interstitials [52].

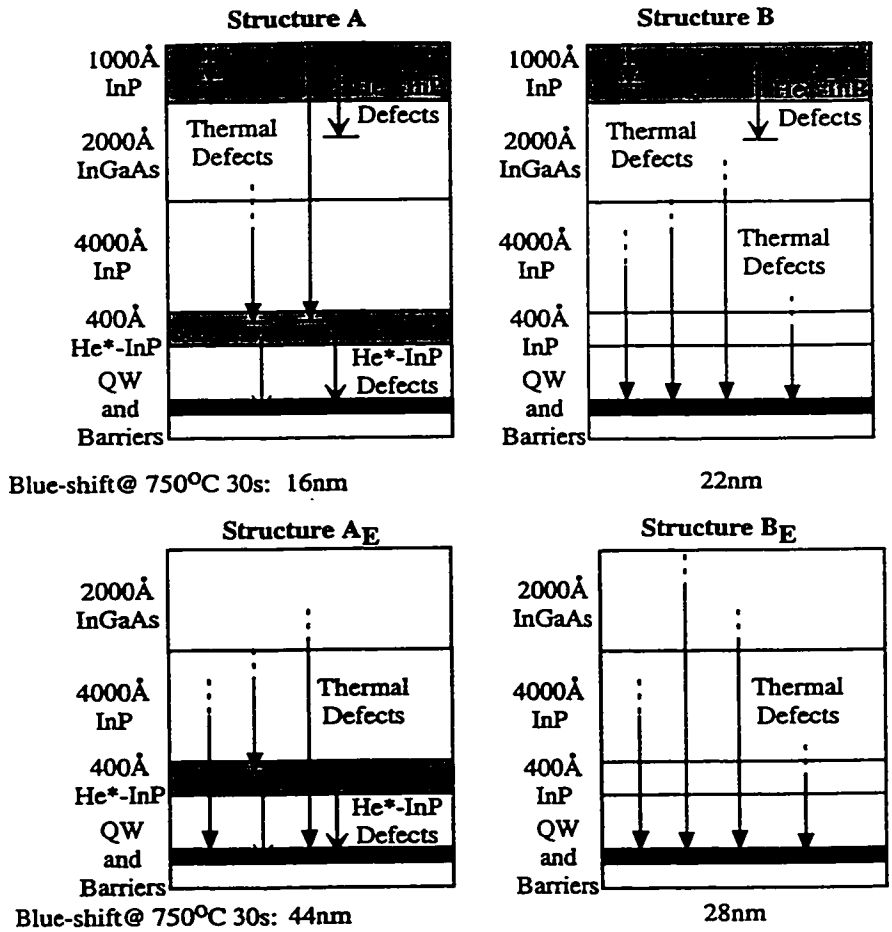

Figure 3.7: Schematic diagram of the source of the defects causing the intermixing for the samples in experiment 2. (Blue-shift values quoted are for a 750 °C, 30s anneal.)

3.4.3 Experiment 3

Once it was found that the intermixing can be enhanced by using a thinner He*-InP layer, the layer thickness was optimized for an integrated DFB laser and EA modulator. The criteria for an integrated device was discussed in Chapter 2. In brief, one would like the peak PL wavelength of the modulator section to be approximately 25 to 50nm shorter than the PL wavelength of the laser section (depending on the required device parameters), and the carrier lifetime to be as short as possible. From

the previous data, it was estimated that a 700Å He*-InP layer would give a good compromise between a short carrier lifetime and an adequate amount of intermixing.

The structures shown in Fig. 3.8 were designed for the intermixing, and were ultimately fabricated into the devices examined in this thesis. The section with the He*-InP layer will become the modulator section, while the section without the He*-InP layer will become the laser section. They were fabricated on the same wafer by etching the top InGaAs layer and He*-InP layer from the laser section, and then regrowing the top InP and InGaAs layer (as would be required when fabricating integrated devices). The regrowth is required because the He*-InP layer needs to be close to the QWs since the defects have a short diffusion length, and the laser section requires at least 1500Å of material to protect the regrowth interface. This will be discussed in further detail Chapter 4 where the device fabrication techniques are discussed.

The structures shown in Fig. 3.8 were subjected to an anneal at 800 °C for 30sec. This caused the RTPL peak to shift from 1574nm to 1546nm for the laser section. It is important to know the RTPL peak since it is used to calculate the position of the gain peak of the device. The wavelength of the RTPL peak can therefore be used to match the grating to the gain peak. Since the PL peak of the modulator cannot be measured at room temperature, the PL of each structure was repeated at 15K. The modulator PL peak was measured at 1398nm(±1nm) with a maximum measured voltage of 0.0108mV. For comparison, at this temperature, the PL peak for the laser section was 1427nm(±1nm) with a maximum measured voltage of 0.52mV (as measured from the lock-in amplifier). The PL peak of the modulator was shifted by 29nm with respect to the laser section and the emitted light was decreased by a factor of ~50. The 29nm(±2nm) between the laser and modulator

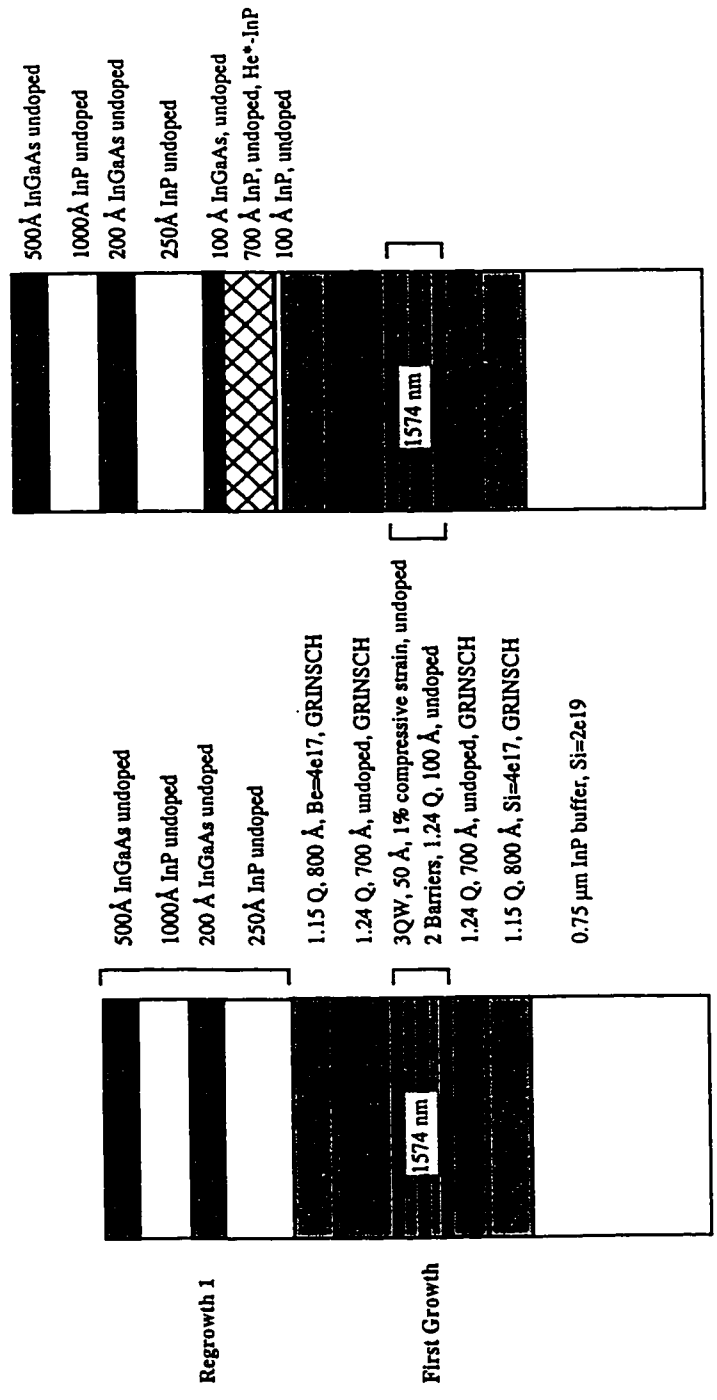

Figure 3.8: Structure investigated for experiment 3. (The top 2 pairs of InGaAs and InP layers were regrown.)

PL peaks is adequate to fabricate integrated DFB lasers and EA modulators, as was discussed in the last chapter.

3.5 He*-InP Induced Intermixing Summary

This chapter presented the first investigation of the annealing properties of material containing both QWs and He-plasma-assisted material. The He*-InP QWI process was found to have some unusual properties. First, even though each of the structures are different (and a direct comparison should be made with caution) there is a general trend relating an increasing He*-InP layer thickness with a decrease in the PL intensity; and a decrease in the relative blue-shift as compared to the thermal-only blue-shift when the He*-InP is adjacent to the active region. It was hypothesized that a thick He*-InP is able to block the defects associated with the thermal blue-shift, while a thin layer allows some of the defects to pass through. At the same time, it was shown that intermixing is caused by defects from the He*-InP layer itself. This hypothesis explains why a sample with a thin He*-InP layer shows enhanced QWI, while a sample with a thick layer shows a suppressed QWI.

In summary, from the results shown in this chapter, it is concluded that:

1. At least one of the He*-InP defects is mobile and can cause QWI. These defects also quench the PL from a QW by acting as non-radiative recombination centres.

2. For thick layers of He*-InP ($\sim$ 2000Å), the He*-InP appears to inhibit annealing-induced QWI in both the thermal and dielectric-capped regions.

3. Thin layers of He*-InP material ($\sim$ 400Å) allow the thermally induced disordering defect to pass through, while the defects within the layer annihilate the PECVD dielectric-induced defect. This shows that dielectric induced QWI is

caused by a different process than the thermally induced QWI.

4. The He*-InP defects are less mobile than those which cause intermixing in the thermal and dielectric-enhanced intermixing processes, and diffusion of the He*-InP defect can be blocked by an InGaAs layer.

5. The majority of the thermal blue-shift appears to be coming from defects migrating from outside the QW region (i.e. from the InP waveguide layers, the InGaAs contact layer, or the semiconductor-air interface.)

6. For the structures investigated, the amount of blue shift increases with decreasing He*-InP layer thickness while the reduction in the PL intensity increases with increasing He*-InP layer thickness which suggests that both effects depend on the number of He*-InP defects within the structure.

The use of He*-InP layers offers a promising alternative method of fabricating devices containing regions of different degrees of QW intermixing, and could perhaps lead to a more reproducible technique for QW intermixing that uses epitaxial layers instead of amorphous dielectric layers. One major advantage of the He*-InP intermixing process is that there is no measurable strain in the layers required to induce the enhanced intermixing (as measured by double-crystal x-ray diffraction), and the material should have the same thermal expansion coefficient as the InP substrate (which is important for high-temperature anneals). It is suspected that this lack of strain at the interface is one reason why regrowth over He*-InP defect intermixed material is possible, while it is not possible to regrow over dielectric-enhanced intermixing material. (Regrowths will be discussed in more detail in section 4.1.3.) The He*-InP layer might also be useful in integrating ultrafast devices where short carrier lifetimes are required, though the carrier lifetime of the He*-InP defect intermixed material still

needs to be measured to evaluate how much the carrier lifetime is reduced.

Due to time limitations, much of the essential materials research into the He*-InP intermixing process was left for future work. Further experiments are needed to evaluate the materials: identification of the specific defects would provide further insight to how the defects interact, and the carrier lifetime in the QWs after the 800 °C anneal has yet to be determined. The He*-InP layer thickness must be optimized since, from the few points investigated, the blue-shift increases with decreasing layer thickness, while the PL intensity decreases with increasing layer thickness. It would also be worthwhile to investigate more thoroughly the effects of anneal temperature and anneal time on the samples in the hope of further optimizing the intermixing process. A discussion of the method used to integrate a DFB laser with an EA modulator fabricated using He*-InP is discussed in Chapter 4.

Chapter 4

Fabrication Details for DFB Gratings and Electroabsorption Modulators

This chapter outlines the processing procedure used for the fabrication of ridge waveguide DFB lasers and EA modulators. Several new processing techniques had to be developed such as selectively patterning a DFB grating, grating etching, and regrowth over an annealed QW structure before the integrated device could be fabricated. Since these procedures influence how the devices were fabricated, they will be discussed first. The second part of this chapter will discuss how these procedures were combined to fabricate the integrated device. It also outlines some of the difficulties encountered. For reference, the step-by-step processing procedure is given in Appendix C.

4.1 Processing Procedure Development

There are several procedures that had to be developed in order to fabricate the integrated device:

1. a procedure to etch the grating

2. techniques to selectively pattern the grating

3. a procedure to regrow over DFB gratings

4. a method to achieve the He*-InP QWI in selected areas

5. modifications to the regrowth procedure to accommodate annealed material

The technique used to pattern the grating will be discussed first. Secondly, the modifications to the processing procedure required to selectively pattern the grating will be discussed. The section will close with a description of the technique developed to regrow over annealed material. (The QWI procedure was discussed in detail in Chapter 3 and will not be discussed further in this section.)

4.1.1 Grating Patterning and Etching

All grating patterning performed in this thesis was done using a holographic system (i.e. by two beam interference). The steps required for grating patterning are illustrated in Fig. 4.1 with further detail provided in Table 4.1.1. In brief, grating fabrication requires patterning, etching, cleaning, and finishes with a regrowth. Further details are discussed below.

The grating patterning starts with a truncated laser structure such as that shown in Fig. 2.4. The laser structure is grown up to the top waveguide layer, and is then capped with a 250Å InP layer. The purpose of the InP layer is twofold: to help obtain the correct etch depth, and to act as a sacrificial layer that is removed just before the regrowth to ensure the 1.15Q regrowth interface is kept as clean as possible. All patterning takes place on top of the sacrificial InP layer.

The patterning for a DFB grating is in many ways similar to patterning other structures. The main difference is the small scale of the features which provides ad-

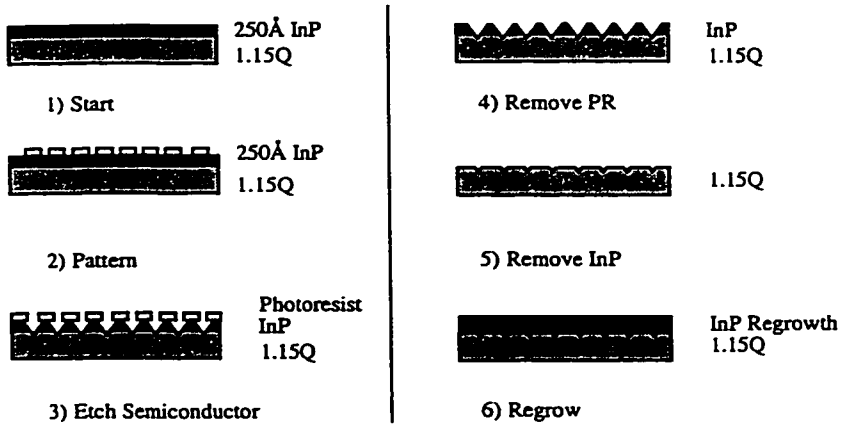

Figure 4.1: Steps required for grating fabrication.

ditional difficulties, especially in the determination of the quality of the patterning. The photoresist (PR) used is Shipley 1808 which is a positive resist (i.e. exposed areas are removed during developing). Due to the small feature size, the PR is thinned in a ratio of 2:3 PR:thinner, and spun on at 5000rpm to ensure the formation of a thin layer of photoresist. After the photoresist is spun-on to the semiconductor surface, the sample undergoes a soft-bake on a hot plate. (A soft-bake is low temperature bake required to partially cure the PR before the exposure is made.) The thinned photoresist requires a lower soft-bake temperature (80 °C) than unthinned PR (110 °C). Also, because the features are so small, the soft bake temperature is more critical. It is essential that the hot plate is allowed to stabilize at the correct temperature (for at least 30 minutes). If the hot plate is too cold, the PR won't set properly and too much of the PR will be removed during development. If it is too hot, not enough of the PR will be removed during the development. Either way, the grating will be patchy. Even a 5 °C temperature variation is enough to noticeably affect the grating quality.

With the soft bake completed, the PR is exposed in the UV holographic setup

Step	Purpose / Comments
Allow HeCd Laser to warm up	
Bake sample at 80 °C for 5 min.	To remove water from surface to ensure hot plate is at the right temperature.
Apply thinned photoresist using standard techniques	
Spin PR at 5000rpm	To ensure a thin layer is formed
Bake at 80 °C for 1 min.	Softbake temperature is critical
Expose in holographic system for 40 sec.	(Detector reading=250μW)
Develop in Microposit CD-30 developer for 45 sec.	Slow agitation works best
Check development	See text for techniques
Bake at 110 °C for 2 min.	Hard bake
Etch in 1:1:20 HBr:HNO_3:DI (etch for 30s using gentle agitation)	See text for special notes (Will result in 50nm grating depth in the quaternary)
Rinse in DI	Stop the development
Soak in Acetone for 5 min.	To remove PR
Etch in 1:2 HCL:H_3PO_4 for 30s	To remove InP.
Remove sacrificial layers using selective etches.	To ensure a clean regrowth interface

Table 4.1: Procedure used to pattern Bragg gratings into a 1.15Q laser waveguide layer.

(Fig. 4.2). The apparatus consists of a Kimmons HeCd laser (which emits at 325nm), a spatial filter which removes beam nonuniformities and expands the beam, a beam splitter to form the two beams required for interference, and two rotating mirrors that are used to redirect the beams onto the sample and to vary the grating period. Normal exposure times are 40s for a 318μW/cm^2 arm power (i.e. the 1cm diameter detector measures 250μW in each arm). Ideally both beams will have an identical power level to ensure that the nodes in the standing wave pattern formed from the interference have zero power and do not expose the photoresist. Both beams must be incident on the sample at the same angle from the normal otherwise the photoresist

will develop with a non-uniform profile. The grating period is varied by rotating the mirrors. Generally, for DFB laser wavelengths between 1520nm and 1570nm, the sample holder does not need to be moved when the mirrors are rotated–the beams are wide enough to provide adequate sample coverage for a quarter wafer. (It is always preferable to move as few components as possible when aligning optical systems.)

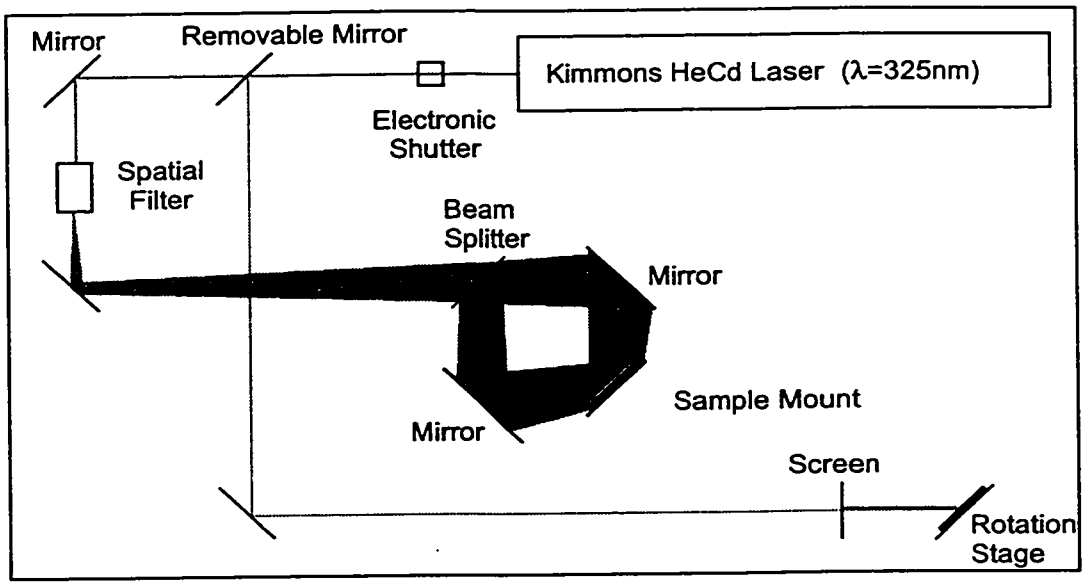

Figure 4.2: Holographic system for DFB Fabrication

The grating period is measured by using the rotation stage in Fig. 4.2 to measure the angles of the light diffracted by the grating. The grating period is related to the diffracted angle by the equation

$$\Lambda = \frac{\lambda_{laser}}{2sin(\theta)} \tag{4.1}$$

where Λ is the grating period, λ_{laser} is the wavelength of the HeCd laser (which is 325nm), and θ is the measured diffracted angle (when the incident angle equals the diffracted angle). To change the DFB laser wavelength, one first calculates the required grating period (Λ) using the modal index of the laser waveguide and the

equation

$$\Lambda = \frac{\lambda_B}{2n_0} \tag{4.2}$$

where λ_B is the Bragg wavelength (which is the wavelength at centre of the stop band as was discussed in Chapter 2), and n_0 is the modal index (n_0=3.20 for a 2μm ridge width for the structure shown in Fig. 2.4). The required angle of diffraction is then calculated from (4.1). The amount that each of the mirrors must be rotated is calculated by

$$\Delta\theta_{mirror} = \left| \frac{\theta_{current} - \theta_{target}}{2} \right| \tag{4.3}$$

where $\theta_{current}$ is the current grating diffraction angle and θ_{target} is the target diffraction angle. To change the period, the mirrors are rotated in opposite directions: rotating the mirrors toward each other increases the grating period, rotating the mirrors away from each other decreases the grating period. The rotation of the mirrors must be controlled to a high degree of accuracy. For example, to change the DFB lasing wavelength from 1570 to 1550nm, the grating period must be changed from 245 to 241.9nm (corresponding to diffraction angles of 41.55° and 42.20° respectively) which means that each of the mirrors must be rotated by only 0.325° (or 19.5 arc-minutes). Extremely tight control of the mirror angle is required for WDM applications where the DFB laser output wavelength needs to be controlled to a fraction of a nanometer.

Development of the exposed photoresist is the next critical step after the exposure. The developer used is Shipley CD-30. The development procedure affects the amount of PR removed which will affect the grating pattern quality as illustrated in Fig. 4.3. An underdeveloped pattern results in regions where not enough of the photoresist is removed, and an overdeveloped pattern results in areas where too much of the photoresist is removed. Hence, both an underdeveloped and an overdeveloped grating will result in regions where the grating is not etched properly into the semi-

conductor. The amount and the uniformity of PR removed is affected by the amount of agitation of the sample during the development. A slow agitation appears to work best: it gives the best trade off between reproducibility and uniformity of the pattern.

After the development, there are three checks for the grating quality: the optical microscope, the diffraction from the grating using the light from a white light source, and the diffraction from the grating examined with light from the HeCd laser. An optical microscope is used as the first check since the light from the microscope does not expose the PR further (if the filters are used). In the microscope a pattern of darker and lighter areas is observed. The darker areas are those that are unintentionally underdeveloped and are caused by PR and optical nonuniformities (often caused by dust on the optics). If the development has been successful, the majority of the sample should be the lighter of the two colours. Next the diffraction by the grating from the white-light source is inspected. The diffracted light should be a uniform blue colour with the intensity of the diffracted light being proportional to the depth of the grating in the photoresist (i.e. the intensity of the diffracted light decreases as more of the photoresist is removed). Black regions signify areas of over-development in which the grating has been completely removed. However, if the grating appears too vibrant, the grating might be underdeveloped (with not enough of the photoresist removed) which will result in a patchy grating after etching. The final test of quality of the grating pattern is the quality of the diffraction pattern obtained by using the beam from the HeCd laser. The diffracted spot should be uniform with very few (if any) side fringes. Multiple diffraction spots are a sign of a nonuniformity in the grating.

Etching the grating is the next critical step. The etchant used is an aqueous bromine solution. This is formed by reacting HBr and HNO_3 to form bromine, and

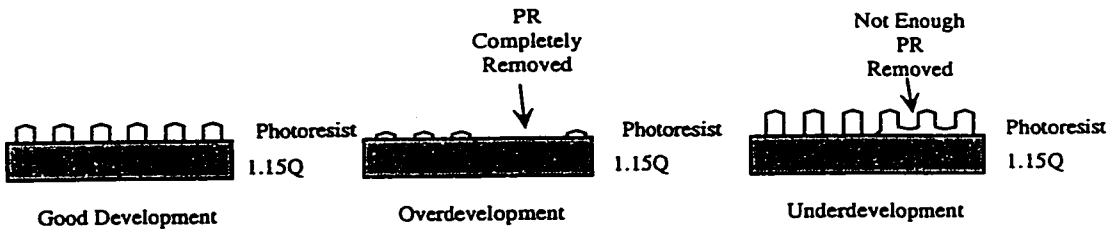

Figure 4.3: Schematic diagram illustrating a properly developed, an overdeveloped, and an underdeveloped DFB grating.

then slowing the reaction by pouring the acid mixture into water. Care must be used when mixing the acids. The acid mixture must be kept in the fumehood at all times. If the solution is left too long before the water is added (greater than ~15 min), noticeable amounts of bromine start to be released into the atmosphere. The concentration of bromine in solution depends heavily on the amount of agitation and the time left before the mixture is diluted. Once the acids are added to the water, the reaction slows down significantly, and it can take several hours for the solution to reach equilibrium. The slow speed of the reaction is the reason why the acids are mixed together before they are added to the water. Also, the reaction is slightly exothermic, so a one hour wait is required before the etchant is used. The etch rate appears to be somewhat proportional to the color of the etchant: the darker the etchant, the faster the etch rate. It was found that a 1:1:20 HBR : HNO_3 : DI solution, agitated for 90s then left to rest for 10 min. before adding to the water works well for obtaining reproducible results. For a 30s etch time, this acid mixture results in a total etch depth of ~80nm in a partial laser structure that is capped with the 250Å InP layer (as was illustrated in step 4 of Fig 4.1). Before regrowth, the InP layer is removed using a selective etch leaving approximately a 50nm deep grating in the 1.15Q waveguide layer.

4.1.2 Selectively Patterning the DFB Grating

Fabrication of EA modulators integrated with DFB lasers is more complex than fabricating DFB lasers alone. A direct writing method such as that which uses an electron-beam can be used to pattern the grating only in specified regions. However, our system is holographic and since a holographic system exposes the whole sample with a grating pattern, it is necessary to develop a technique to pattern the material so that one area has a grating (the laser section) and one area does not (the modulator section). A double-exposure is not a viable procedure to selectively pattern the grating because a double-exposure results in regions with all the photoresist removed (since a positive resist is being used). This means that the waveguide in the modulator section will be etched at the same time as the grating is etched (thereby changing the waveguiding properties in the modulator section). Instead, a better way to selectively pattern a grating is to use an etch mask. This etch mask can be either a dielectric layer or a semiconductor layer–the only requirements are that it must inhibit the etching into the quaternary layer and that it must be thin. Using a thin etch mask acts to minimize the transition region between the grating and no-grating regions. As shown schematically in Fig. 4.4, photoresist builds up around patterned features whenever non-planar samples are patterned and will cause the photoresist to not be patterned properly in these regions.

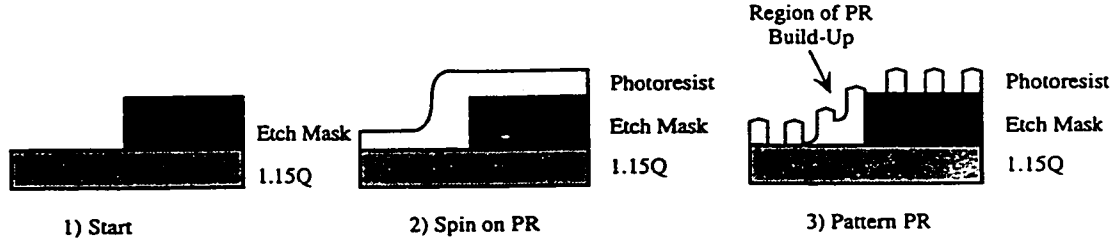

Figure 4.4: Schematic diagram illustrating photoresist build-up around non-planar surfaces.

At first glance, a dielectric mask appears to be a better solution than a semiconductor mask since a thin (20nm) dielectric layer can be grown which is sufficient to act as an etch mask. A 20nm oxide mask has been investigated, and a sharp boundary between the grating and no-grating regions can be obtained. However, experience has shown that PECVD dielectric growths can both contaminate and damage the material–especially if the sample has undergone an anneal with the dielectric cap. This can particularly be a problem when one is trying to regrow semiconductor material on an interface that had a CVD dielectric film.

A much better alternative is the use of a semiconductor etch mask. A schematic diagram of the procedure is illustrated in Fig. 4.5. The layer must be thicker than a dielectric mask (at least the thickness of the etch depth since the etchant used to etch the grating will also etch the semiconductor mask). One of the main benefits of using a semiconductor etch mask is that there is less contamination. It has been found that an 1150Å thick layer of semiconductor works well as an etch mask since it completely prevents a grating from being etched in the 1.15Q, while only preventing proper grating formation for about 2μm from the device boundary due to photoresist build up. The transition region between the two sections does not degrade device performance. Also, as an added benefit, the He*-InP layer used to enhance the intermixing can also be used as a semiconductor etch mask as will be discussed in detail in section 4.2. Due to the dual use of the He*-InP layer, using a semiconductor etch mask yields a processing procedure that involves one less mask step than a procedure that uses a dielectric etch mask.

After the semiconductor etch mask is patterned, the grating is patterned by using the techniques that were discussed section 4.1.1. The semiconductor layer acts as an etch mask thereby preventing the grating from being etched into the 1.15Q layer

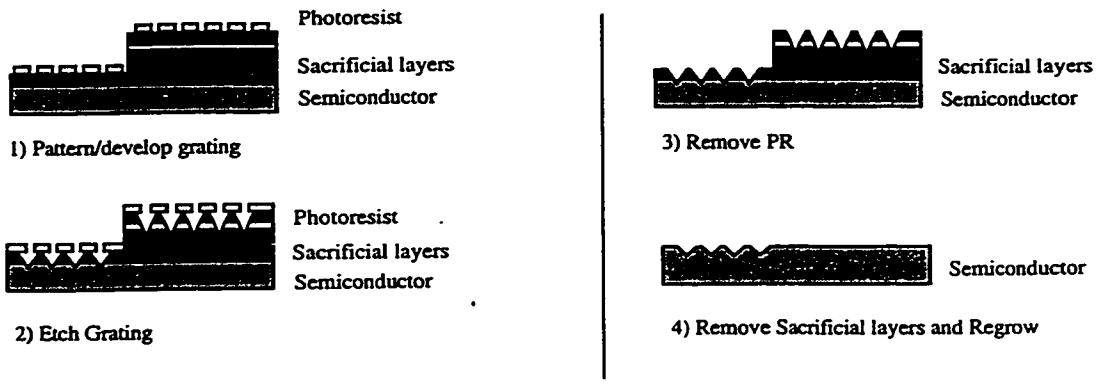

Figure 4.5: Schematic diagram illustrating the selective patterning of the grating.

in the modulator section. After the grating is patterned and etched, it is a simple matter to remove the etch mask down to the 1.15Q layer with the standard InGaAs and InP selective etches.[1] These etchants do not noticeably affect the grating etched into the 1.15Q nor the ability to regrow over the interface so additional patterning is not required. After etching the sacrificial layers, two regions remain: one with a grating, and one without. In this way, EA modulators can be fabricated with only one more mask step than that required for DFB lasers.

4.1.3 General Regrowth Procedures

The devices in this thesis require multiple regrowths: one standard regrowth, and one on annealed material (as will be discussed further in section 4.2. There are enough difficulties associated with regrowths that it is worthwhile to discuss general regrowth procedures before discussing the difficulties encountered when annealing before the regrowth.

A successful regrowth requires the formation of a minimal number of defects, rapid planarization, a minimal amount of mass transport, and a minimal amount of

[1] 1:8:80, H_2SO_4:H_2O_2:H_2O for InGaAs, and 1:2, HCl:H_3PO_4 for InP.

contamination at the regrowth interface. The regrowth procedure used for the devices in this thesis follows the optimized method developed by Robinson et al. [53]. Before the samples are regrown, they must be cleaned. Sample cleaning before regrowth is critical since the cleaning determines the regrowth interface quality. Because of this, all patterning was performed on a sacrificial layer of InP, which was stripped away before the regrowth (using a selective etch) to help ensure the formation of a clean regrowth interface (as was illustrated in Fig. 4.1. After the InP was removed, the sample was cleaned using standard chemical cleaning techniques: warm acetone and methanol baths, followed by a 20 minute UV ozone and an HF acid dip to remove the native oxide. (A longer ozone treatment is used than that used for normal InP cleaning.) Further details are given in the section C.1. After a chemical clean, the sample is then transferred to the MBE chamber for regrowth where an in-situ clean is performed.

A balance needs to be reached between the removal of contaminants and the minimization of mass transport during the in-situ clean. The cleaning procedure outlined here is effective at removing contaminants, but also causes significant mass transport–approximately the bottom third of the grating is filled in by mass transport and needs to be accounted for in the device design. The details of this cleaning process and its effectiveness (including results from SIMS and TEM) is discussed in detail in the paper by Robinson et al. [53] as well as the effects of using a phosphorus instead of an arsenic overpressure during the cleaning phase. (A phosphorus overpressure is required if the regrowth is on an InP surface instead of InGaAsP.) The details are as follows: once the samples were loaded into the MBE chamber, they underwent an in-situ cleaning at 485 °C using an ECR Hydrogen plasma and a Group V overpressure of As_2 (provided by 1.7sccm AsH_3 injected directly into the chamber) for 5 minutes.

The temperature was then ramped to 470 °C within 1-2 minutes. The Group V overpressure was then switched to PH_3, and the regrowth with InP was started. The remaining material was then regrown using the standard growth techniques used at McMaster University.

4.1.4 Annealing Before Regrowth

The devices in this thesis are based on a procedure that involves a high-temperature (800 °C) anneal before the regrowth to produce selective-area quantum-well intermixing. Due to the effect of the anneal on the material, this must be taken into account when designing the laser, and these design considerations will be discussed in this section.

There are several reasons for choosing to anneal before the regrowth. Preliminary investigations into annealing after regrowth have shown that the regrowth can have an unpredictable effect on the quantum-well intermixing, depending on the quality of the regrowth and/or the grating depth. Due to this lack of reproducibility, it is difficult to match the grating wavelength to the gain peak of the material as well as satisfying the PL peak requirements for the modulator. Also, since it is not possible to measure the photoluminescence (PL) from a completed laser structure due to the material absorption, it is difficult to measure the wavelength of the PL peak to verify the amount of intermixing. (The top waveguide layers would need to be etched off to measure the PL.) So instead of trying to match the gain peak to the grating, a procedure was developed to match the grating to the gain peak since the grating can be tuned to any wavelength. This involved annealing the material before the regrowth and then measuring the wavelength of the PL peak of the quantum-wells thereby determining the wavelength shift due to the thermal anneal. If there is any deviation in the peak PL wavelength from that expected, the grating can be tuned

to match the gain peak thereby ensuring a properly matched grating. Due to the large number of steps required to fabricate the integrated device, a PL measurement is simple and worthwhile check to ensure the QWI behaved as planned.

To our knowledge, we have performed the first regrowths by GSMBE over high-temperature (800 °C) annealed QW material. Regrowth on annealed surfaces introduced an unexpected set of problems. The surface of the overgrowth layer exhibits significant roughness due to the formation of many defects. This problem was solved by growing a sacrificial layer (of InP or InGaAs) with thickness greater than 1500Å on top of the 1.15 quaternary waveguide layer. This sacrificial material protects the 1.15Q regrowth surface during the anneal, and is etched off before the regrowth. Then, using the standard regrowth techniques (discussed in section 4.1.3) a smooth surface morphology on the regrowth layer is achieved.

Regrowth over material that was subjected to QWI using He*-InP defects does not exhibit the regrowth problems observed when regrowths are performed on material that was subjected to dielectric-enhanced QWI (as discussed in section 1.5.3). There is no distinction in the quality of the regrowth between material containing the He*-InP defects and material without the defects providing a 1500Å sacrificial layer was used over the regrowth interface. The ability to regrow over QWI regions using the He*-InP defect to produce the intermixing is a major benefit of this technology.

4.2 Integrated DFB and EA Modulator Fabrication Procedure

The techniques discussed above were used to fabricate integrated DFB lasers and EA modulators. Device fabrication is complicated by the fact that ~1500Å of sacrificial material is required to protect the subsequent regrowth surface during

the anneal and to facilitate a good regrowth, while the He*-InP layer must be less than 1500Å away from the waveguide layer due to the short diffusion length of the defects at 800 °C. This means that two regrowths are required–the first one to provide the required protection during the anneal and to form the proper etch masks for fabricating the grating, and the second, to complete the device. Subsequently, the fabrication procedure for an integrated DFB laser and EA modulator involves:

1. a first growth which includes the quantum-wells and the majority of the waveguide
2. sample cleaning
3. patterning to define the laser and modulator sections
4. regrowing the sacrificial material required for protection during the anneal
5. annealing the sample to induce QWI
6. sample cleaning
7. removal of sacrificial material
8. patterning the grating
9. growth of the upper waveguide and contact layers
10. processing the RWG and contacts

A schematic diagram of these steps are given in Fig. 4.6. The detailed steps are in Appendix C.

The first step in fabricating the devices is the growth of the waveguide and quantum-wells. (The different growths required to fabricate the integrated device is

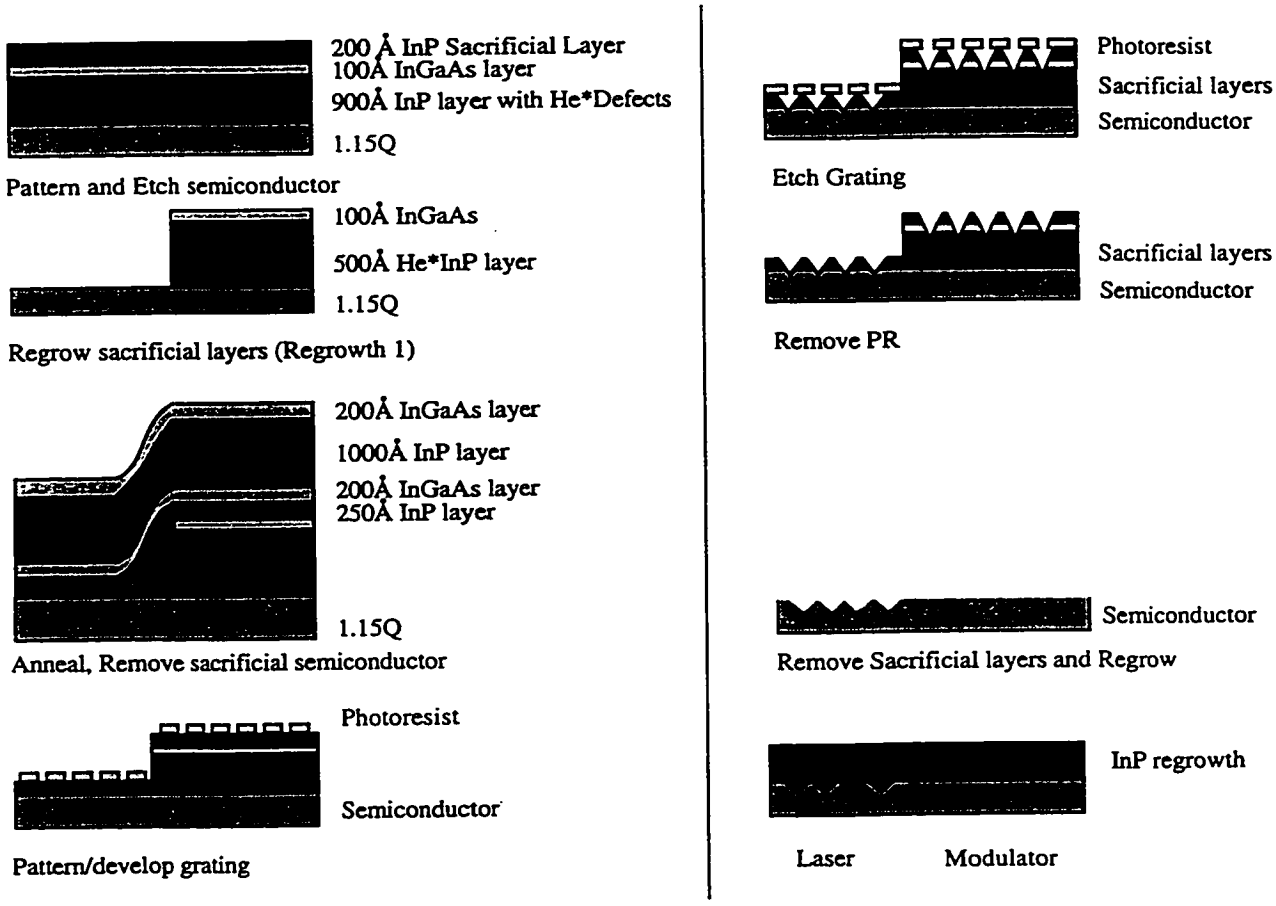

Figure 4.6: Steps required for DFB and EA modulator fabrication.

shown in Fig. 4.7). The first growth has extra layers which are used to facilitate the quantum-well intermixing process, assist in the formation of a defect-free regrowth, and to act as the semiconductor mask required to inhibit grating formation in the modulator section. The top 200Å InP layer is used as a sacrificial layer to ensure a clean regrowth surface–the InP layer is left on during the patterning until the sample is ready to be cleaned for the regrowth. The He*-InP layer provides the defects that enhance the QWI, as discussed in Chapter 3. The InGaAs layer is required for a good quality regrowth (since for the in-situ cleaning an As_2 overpressure was used) and acts as an etch stop for the subsequent removal of the sacrificial layer of InP.

All patterning procedures start with a sample cleaning step. This is to ensure there is a consistent surface to work with which decreases the probability of problems during the various processing steps. The cleaning procedure is summarized in table 4.2. In summary, cleaning procedures involve: a solvent clean to remove organic contaminants; an ozone clean to oxidize the remaining organics and to oxidize the semiconductor surface; and a HF dip to remove the native oxide formed by the ozone (thereby removing several monolayers of the semiconductor surface).

Step	Purpose / Comments
Dry samples with nitrogen (N_2)	to remove light particles
A1 (Acetone) @ 90 °C for 5 min.	solvent clean
A2 @ 90 °C for 5 min.	
M1 (Methanol)@ 90 °C for 5 min.	
M2 @ 90 °C for 5 min.	
De-ionized water (DI) rinse.	
Blow Dry	Prevent water from beading
UV ozone for 10 min.	Oxidize organics and semiconductor
HF dip in 10: 1, DI:HF for 2 min.	Remove native oxide
DI rinse for 2 min.	Remove HF contamination
Blow Dry	Prevent water from beading

Table 4.2: General semiconductor cleaning procedure.

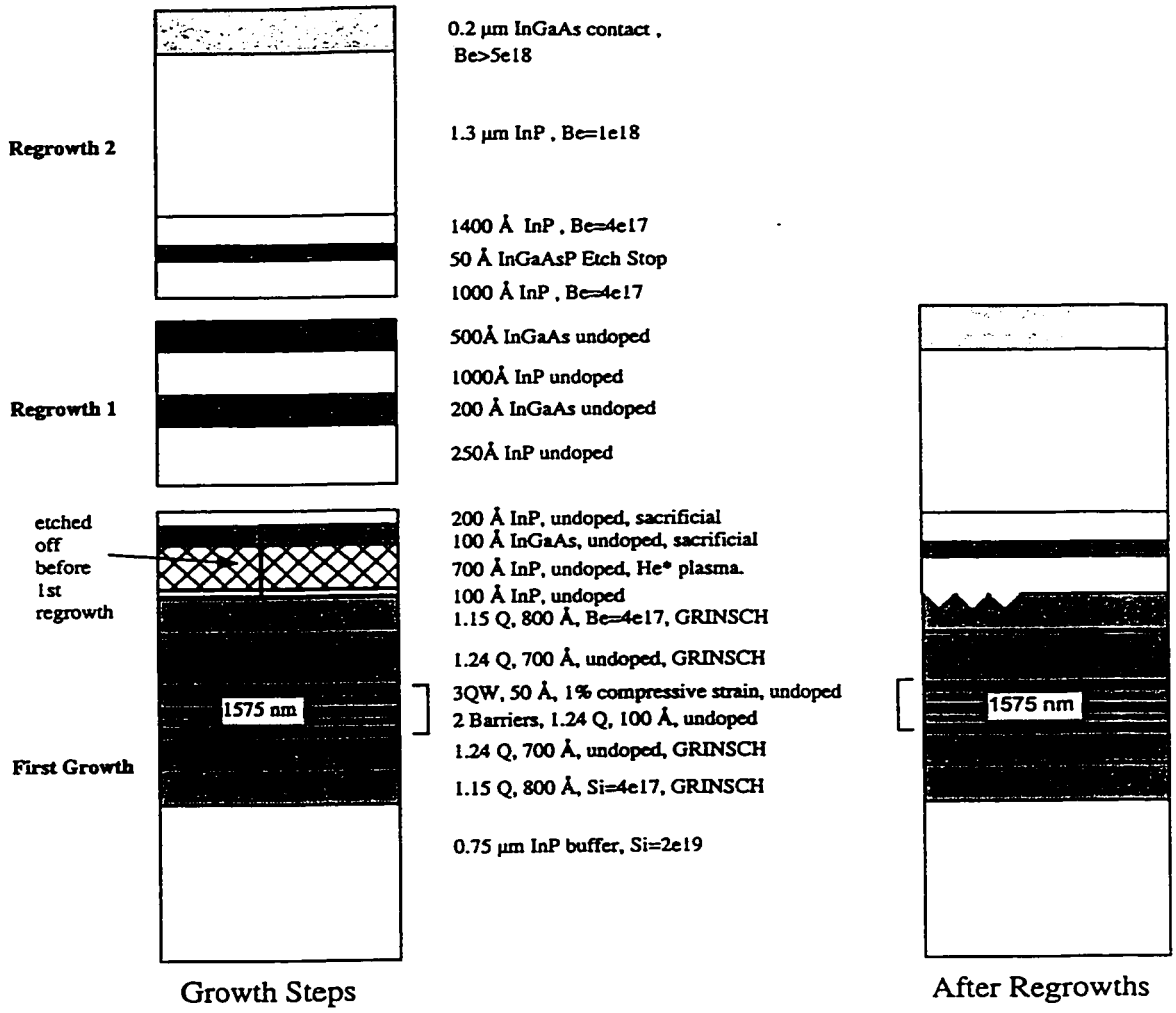

Figure 4.7: Growths required for the integrated laser and modulator structure.

After the semiconductor is cleaned, the modulator and laser sections are patterned. Due to the coarse feature size and to minimize contamination effects, an oxide etch mask is not used at this step. Instead, the photoresist is spun on the surface of the InP layer shown in Fig 4.6. After patterning, the top InP and InGaAs layers are removed from the laser section using the normal selective etches. The photoresist is then stripped off, and the remaining InP is removed to leave a relatively clean surface for regrowth. (The top layer in the modulator section is InGaAs, and the top

layer in the laser section is a 1.15Q.) The sample is then cleaned further by using the techniques discussed in section 4.1.3. The sacrificial material shown in Fig 4.7 (regrowth 1) is then grown.

Step	Purpose / Comments
Pattern laser and modulator sections using standard PL techniques	Define laser and modulator sections
Etch for 15s using 1:2 $HCl:H_3PO_4$	Remove InP in laser section
Etch for 15s using 1:8:80 $H_2SO_4:H_2O_2:H_2O$	Remove InGaAs layer in laser section
Soak in acetone at 80 °C for 5 min.	Remove photoresist
Etching for 1 min. using 1:2 $HCl:H_3PO_4$	Remove top InP layer (in both sections)
Clean for regrowth	Prepare for QWI
Submit for regrowth	
When sample is returned, anneal for band gap shifting	Perform QWI
Clean using standard techniques	Prepare for grating patterning
Remove native oxide- 1 min. 49%HF.	Native oxides can act as a mask
Etch off top layers to the 250Å InP layer using the standard selective etches	The 250Å InP layer is required for proper grating formation
Pattern grating	Using previously discussed techniques
Remove semiconductor etch mask using selective etches	Prepare for regrowth
Clean sample	
regrow	Next step: RWG patterning

Table 4.3: Procedure to pattern the grating in the laser section and prevent the grating formation in the modulator section.

After the first regrowth, the sample was annealed at 800 °C for 30s. The results from the anneal were discussed in detail in section 3.4.2. In summary, before annealing the room temperature photoluminescence (RTPL) peak from the quantum-wells after the growth was at 1574nm. After the first regrowth, an anneal was performed at 800 °C for 30sec. This caused the RTPL peak to shift from 1574nm to

1546nm for the laser section. (The PL of the modulator section cannot be measured at room temperature.) At 15K, the PL peak for the laser section was 1427nm and the modulator PL peak was measured at 1398nm giving a relative blue-shift of 29nm for the modulator with respect to the laser section.

After annealing, the sample has to be cleaned once again by using the techniques outlined previously in 4.2. After the solvent clean, the native oxide the native oxide formed during the anneal has to be removed with a concentrated (49%) HF etch for 1 minute (otherwise it acts as an etch mask for the subsequent processing steps). (Concentrated HF is much more effective at removing native oxides than diluted HF.) Before patterning the grating, the top InGaAs and InP sacrificial layers are removed down to the 250Å InP layer. As stated earlier (in section 4.1.1), this InP layer is required to both help to obtain the correct etch depth, and to keep the 1.15Q interface clean to provide a good regrowth surface. Next, the grating is be patterned by using the techniques that were discussed in section 4.1.1. The He*-InP layer on the modulator section acts as an etch mask thereby preventing the grating from being etched into the 1.15Q (as was illustrated in Fig. 4.6. After the grating is patterned and etched, the remaining sacrificial layers down to the 1.15Q are removed with the InGaAs and InP selective etches leaving two regions on the 1.15Q surface: one with a grating, and one without. The sample is then cleaned for the regrowth after which the upper waveguide and top contact layers of the samples are grown.

The structure is patterned into RWG lasers using standard photolithography techniques after the upper waveguide layers are grown. Since standard techniques are used, the RWG processing steps are not discussed in detail here but, instead, are summarized in section C.2. However, it should be noted that it is a relatively simple matter to align the isolation trenches with the boundary between the laser

and the modulator sections: the device boundaries are visible even after the regrowth due to the non-planar regrowth surface. Therefore, the alignment marks from when the laser and modulator sections were patterned can be used to align the subsequent steps. Device isolation between the laser and the modulator is provided by isolation trenches ranging from 5 to 15μm long. The trenches are etched down to the etch-stop layer at the same time the ridges are etched. (The completed device structure was illustrated in Fig. 2.1.)

Chapter 5

Device Results

The characteristics of the DFB lasers and EA modulators fabricated for this thesis are discussed in this chapter. The analysis includes both electrical and optical measurements. Both the discrete and the integrated devices were examined and the interaction and isolation between the laser and modulator will be discussed in detail.

5.1 DFB Laser Characterization

There are two ways to investigate whether a laser is lasing in the DFB mode. One way is to examine the spectrum and see if a stop-band is present. However, unless the grating is relatively strong ($\kappa L > 1$), the stop-band can be obscured by the Fabry-Perot fringes if the facets are not AR coated. The stop band is clearly seen in the spectrum of a 600μm laser Fig. 5.1. Note that the power values shown in this plot are smaller than the actual laser output power due to imperfect coupling between the laser and the spectrum analyzer. The width of the stop-band for this device is 1.9 ± 0.1nm. For an ideal DFB laser (with zero facet reflectivity) it is possible to measure the width of the stop-band and use this information to estimate the coupling coefficient. However, since the facet reflectivity is nonzero, it is much more difficult to estimate the coupling coefficient due to the random phase of the

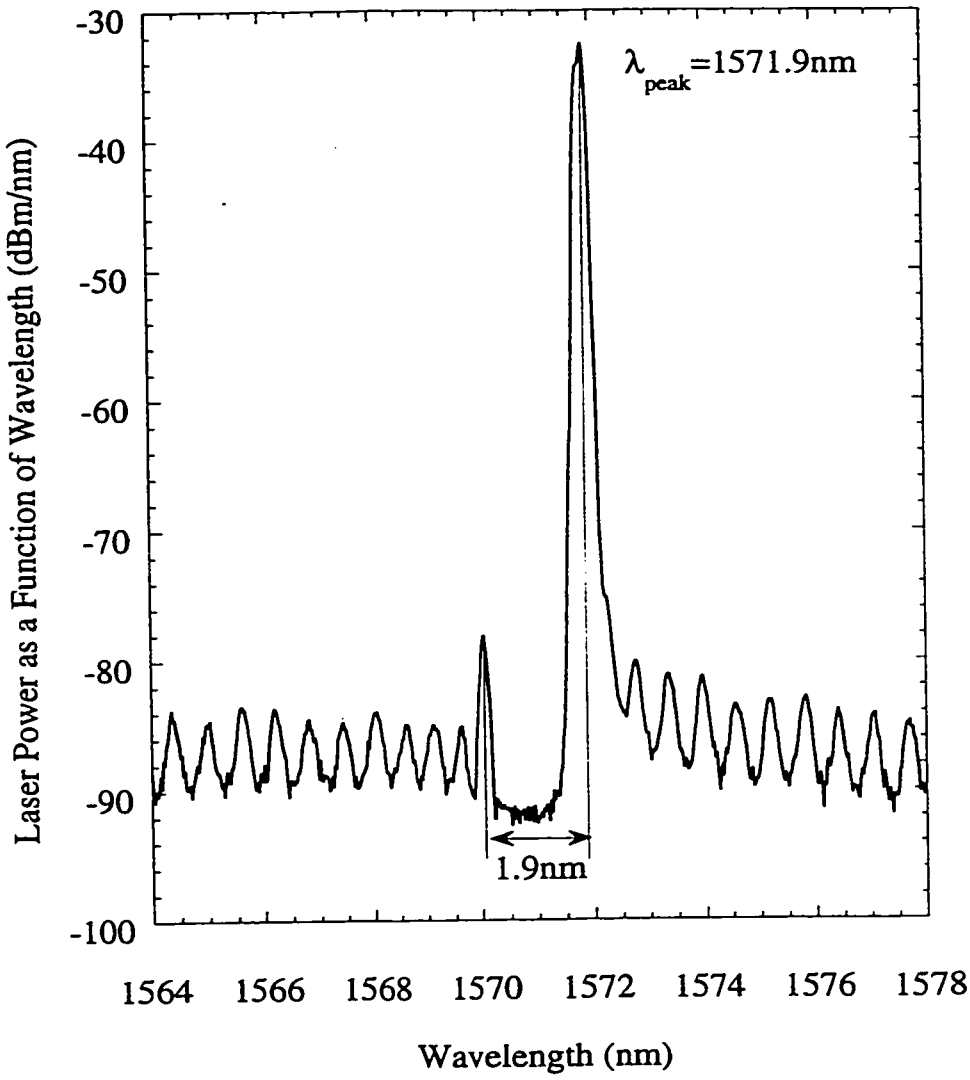

Figure 5.1: Spectrum of a 600μm long DFB laser without facet coatings. The lasing wavelength is 1571.9 $\pm$ 0.08nm, and the stop band width is 1.9 $\pm$ 0.1nm. The SMSR is 45dB.

facet reflectivity. (This was discussed in Chapter 2.) For comparison, a device with zero facet reflectivities would require a coupling coefficient of $\sim$5/mm ($\kappa L = 3$) to give a stop-band width of 1.9nm (as calculated by the TMM). From this, it can be concluded that the coupling coefficient is strong for the device illustrated in Fig. 5.1.

An alternate method to check if a device is lasing in the DFB mode is by

observing the output spectrum as a function of temperature. This is because through the action of the grating, the lasing wavelength will not follow the movement of the gain peak, since the gain peak is more temperature sensitive than the period of the Bragg grating. This technique is particularly useful when the stop-band is obscured by the Fabry-Perot fringes.

The spectrum of a 500μm discrete DFB laser with a weaker coupling coefficient has been obtained and the temperature dependence of the spectrum is illustrated in Fig. 5.2. In Fig. 5.2, one can clearly see that the peak of the spontaneous emission profile (and hence, the gain profile) moves to a longer wavelength with increasing temperature while the lasing wavelength is locked at 1552 $\pm$ 2nm, which confirms that there is distributed feedback from the grating.

The effect of varying the ridge width was also briefly examined. The lasing wavelength varies with ridge width due to the different modal index of each ridge width. A plot of the spectra for different ridge widths is shown in Fig. 5.3. The thresholds of the discrete devices (without antireflection coatings) range from 18 to 35mA and depend on the ridge width, sample length, and where the sample was taken from the wafer. (The threshold currents would be higher if the facets had antireflection coatings due to the reduction in the optical feedback.) The side-mode suppression ratio (i.e. the ratio of the peak power of the lasing mode to the peak power of the next strongest mode) was on the order of 45dB (normal telecom applications require a SMSR of 30dB). The spectra of 3 DFB lasers with 2, 3, and 4μm ridge widths are illustrated in Fig. 5.3. The wavelengths range from 1568-1572nm($\pm$0.08nm) and increase with increasing ridge width due to the different modal index of the lasers. As was discussed in section 2.8, this change in wavelength will affect the operation of the integrated device due to the change in the relative positions of the absorption edge

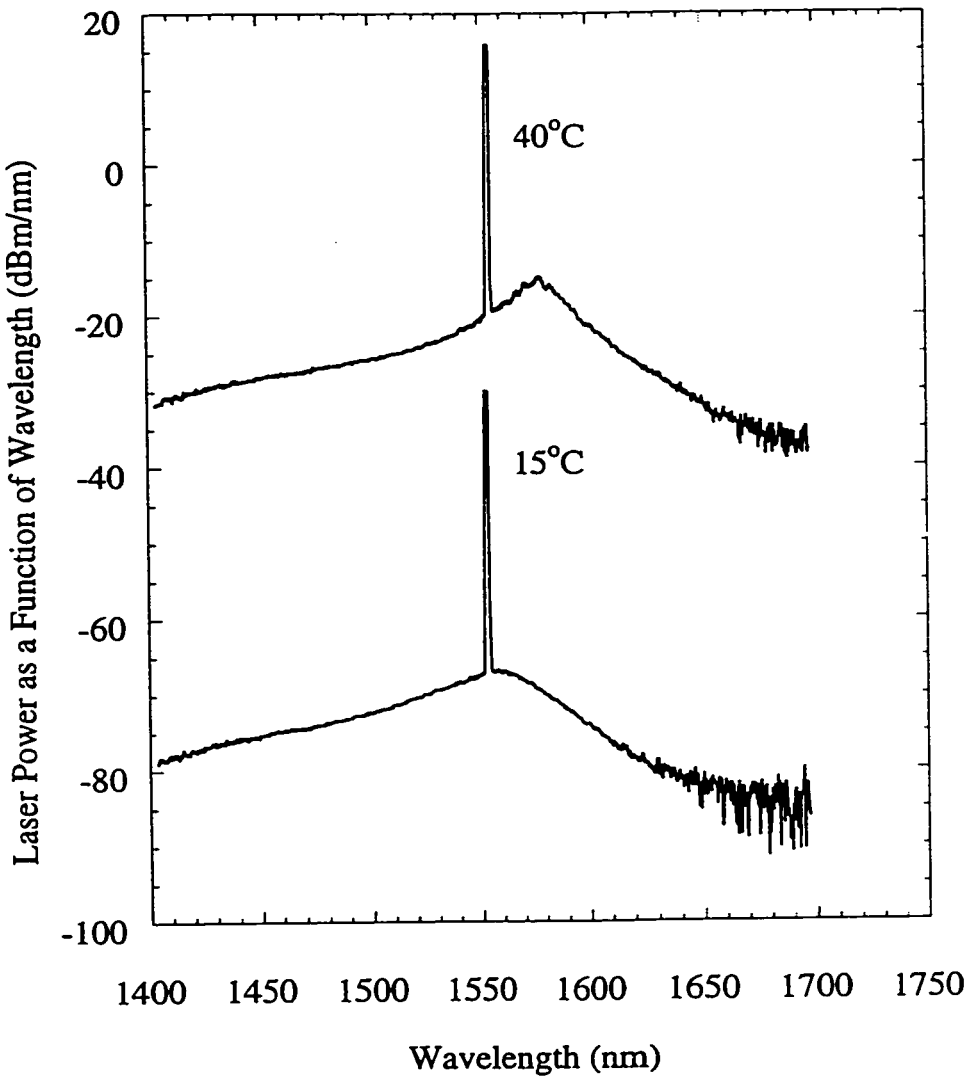

Figure 5.2: DFB laser spectrum at 15 °C and 40 °C. The laser is 500μm long with no facet coatings. The lasing wavelength for this device is 1552 ± 2nm at room temperature. The 40 °C spectrum is shifted by 50dB for illustration purposes.

and the lasing wavelength. The light versus input current (L-I) curves of the discrete devices were measured and found to be kink-free up to the maximum measured input current of 100mA.

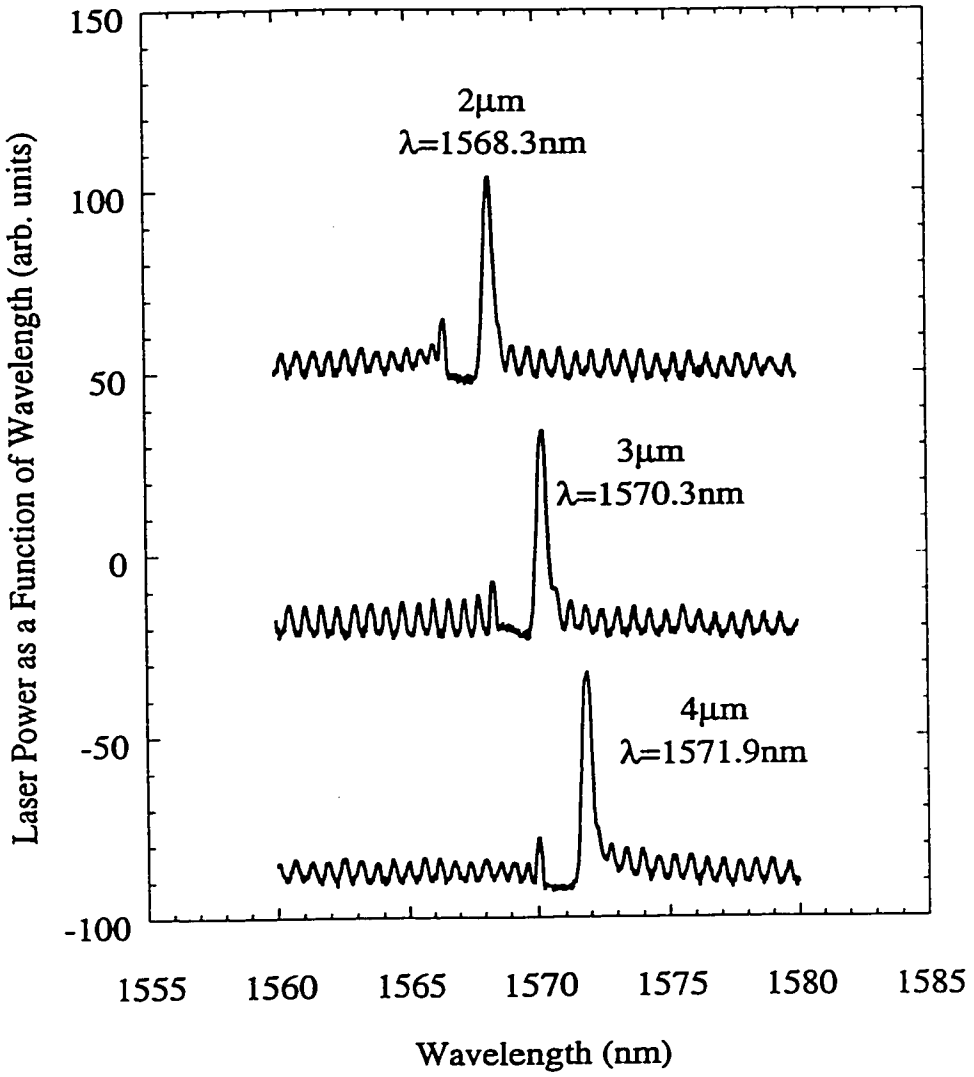

Figure 5.3: Spectra of discrete DFB lasers with ridge widths of 2, 3, and 4μm. The lasers are 600μm long with no facet coatings and are neighboring devices on the same laser bar.

5.2 Modulator Characterization

The modulator needs to be characterized so that one can determine if it is to interact properly with the laser. The three parameters of greatest interest are: the position of the band edge; the magnitude of the absorption at the lasing wavelength; and the dependence of the absorption on bias. There are several ways to characterize

the discrete modulator: a broad-band source or a tunable narrow-linewidth source can be used to measure the transmission through the modulator as a function of wavelength; or a narrow-linewidth source can be used and the photocurrent is measured as a function of wavelength (or conversely as a function of voltage applied to the modulator) to obtain an estimate of the magnitude of absorption [44]. These methods are difficult to implement: high-quality positioning stages and sensitive detectors are required since it is difficult to couple light in and out of waveguides. Care must be used to ensure that the light is coupled into waveguide layers (and not the contact or the substrate) and that the positioning stages do not drift during the measurement thereby changing the amount of light coupled into the waveguide. Also, either a broad-band or a tunable source is required.

Despite these difficulties, a discrete modulator was tested to determine its effectiveness at modulating light. The apparatus is illustrated in Fig. 5.4, and is based on a technique that uses a narrow-linewidth source, and the modulator transmission is measured as a function of modulator bias. A fibre-pigtailed discrete laser operating at 1556nm was used to inject light into a discrete 500μm modulator by using a lensed fibre. The two devices were isolated using an 80dB optical isolator. The alignment for coupling the light into the waveguide was optimized by maximizing the photocurrent generated in the modulator. (Ideally, the near-field pattern would be measured to ensure that the light was correctly coupled into the waveguide; however, the required equipment was not available.) The light transmitted by the waveguide was measured by using a large area detector.

The magnitude of the light transmitted though the modulator for different modulator bias as a function of laser current is shown in Fig. 5.5. The decrease in the slope of the L-I curve with increasing modulator bias signifies an increase in the

absorption of the modulator. Therefore, this figure clearly shows that the absorption in the modulator is increased with increasing reverse bias. The extinction ratio could be increased by using a longer wavelength laser source; however, one was not available. This figure also demonstrates the expected result for a perfectly isolated DFB laser and EA modulator–the slope of the L-I curve changes with bias (without any added kinks) while the threshold remains the same. (Device isolation was discussed in the section 2.8.2.) An alternative technique for measuring the absorption of a modulator that capitalizes on the fact that it is integrated with a DFB laser will be discussed in section 5.3.2.

An attempt was made at measuring the electroluminescence (EL) from the discrete modulator at room temperature by measuring the L-I characteristic of the device. There was no measurable electroluminescence up to an input current of 100mA which suggests that the non-radiative defects have a faster transition rate than the optical transition (i.e. the transition required to produce spontaneous emission). Even a poorly operating (i.e. non-lasing) laser will show measurable spontaneous emission well before 100mA. However, if enough light is injected into the modulator, it is possible to measure a photocurrent. Therefore, it can be concluded that even though the carrier lifetime is reduced, significant numbers of carriers can still escape from the active region of the device.

5.3 Integrated Device Measurements

This section discusses the results obtained from characterizing the interaction between the two devices. The notation used for positive voltages and currents is illustrated in Fig. 5.6.

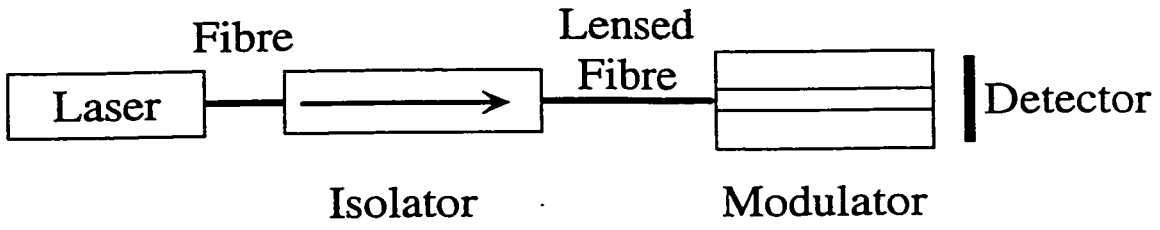

Figure 5.4: Apparatus to measure the discrete modulator transmission as a function of modulator bias.

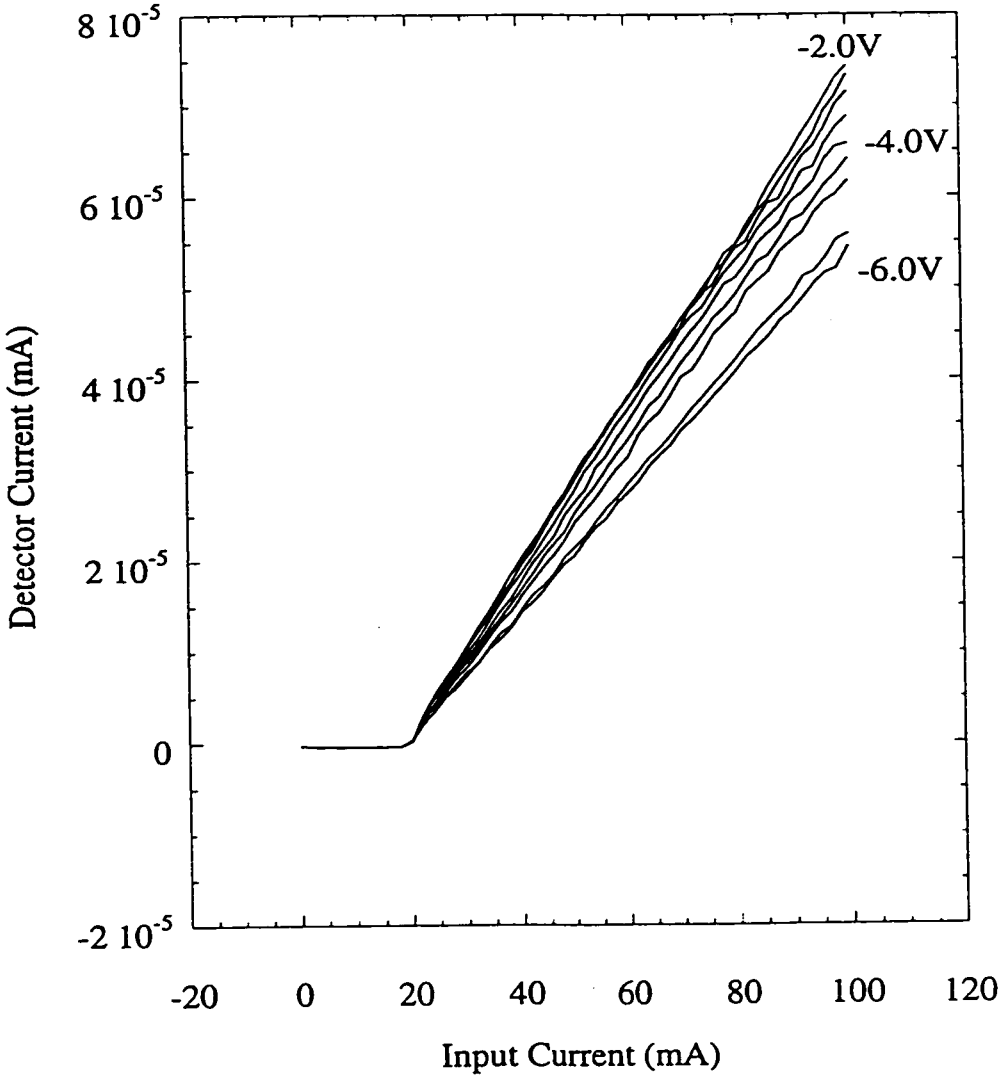

Figure 5.5: The transmitted power through a discrete modulator as a function of laser current for different modulator biases. The laser was lasing at 1556nm.

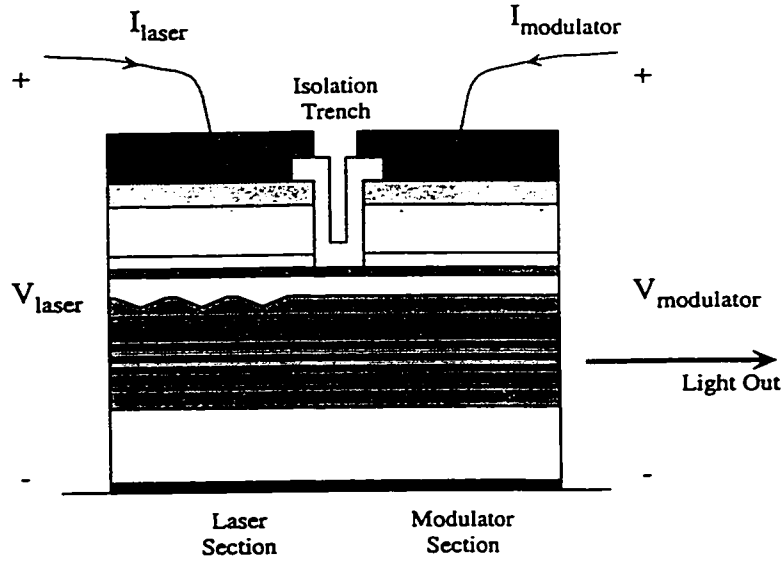

Figure 5.6: A schematic diagram of the applied voltages and measure currents when characterizing the device (The arrows represent positive current flow).

5.3.1 Measured Device Isolation

As previously discussed in section 2.8.2, device isolation is provided by isolation trenches ranging from 5 to 15μm long that were etched down to the etch-stop layer. The electrical isolation between the two contacts for the tested devices was measured to be 2-20$k\Omega$ (from I-V measurements) and depends on the width of the isolation trench, with the larger isolation trenches having a larger resistance. Whether this value is adequate will be discussed in section 5.3.4 when the current-voltage (I-V) curves of the device are examined.

It is difficult to quantify the amount of optical isolation between the laser and the modulator. However, it was found that for the majority of the devices that were tested without AR coatings, the laser experienced enough feedback from the front facet to experience mode-hopping. The amount of mode-hopping increased with increasing ridge-width. This is due to the increased optical coupling and, hence,

optical feedback between the cavities. Due to the mode-hopping, an AR coating is essential for proper device operation.

5.3.2 Modulator Absorption Determined from Laser Spontaneous Emission.

An estimate of the band edge of the modulator as a function of modulator bias was obtained by using the spontaneous emission in the laser section as a broadband source. This was performed by measuring the ratio of the powers out of the laser and modulator facets of the device as a function of wavelength and subtracting the values. The main advantage of such a technique is that the coupling between the broadband source (the laser) and the modulator is fixed and relatively good (as compared to the coupling between a discrete source and tapered fibre). The main problem arising is that the modulator and laser are electrically coupled due to the finite resistance of the isolation trench, so care must be taken when making the measurements. Three techniques were used to minimize the possible errors. First, the laser was biased above threshold for all of the measurements. In this operating regime, a small change in the current affects only the stimulated emission rate, not the spontaneous emission rate (to a first approximation). Second, the modulator-to-laser facet power ratio was determined for each modulator bias independently, so any change in the spontaneous emission profile is taken into account; although, as will be shown shortly, the change to the spontaneous emission profile for different modulator biases is negligible. Third, the laser was held at a constant voltage instead of a constant current in order to minimize the effect of the modulator voltage on the laser current. This was more critical in earlier sets of devices that had an electrical isolation of only $\sim 20\Omega$, which was probably due to incomplete etching of the doped layers in the isolation trench. The later devices that were investigated after the processing had been optimized had

an electrical isolation of 2-20$k\Omega$.

Absorption measurements were made on the fabricated devices using this technique. An absolute value for the material absorption cannot be obtained since there are coupling losses and waveguide losses, which are difficult to estimate. More specifically, the coupling losses between the modulator and the laser remains constant, but the coupling losses between the facet and the optical fibre used to collect the light varies between the measurements of the front and rear facets and adds an offset to the measurement. Even so, this technique is very efficient at making relative absorption measurements; thus it is useful for examining how the modulator absorption spectrum varies with bias.

The laser facet and modulator facet spectra are shown in Fig. 5.7a and Fig. 5.7b. As can be seen from Fig. 5.7a, a change in the modulator bias does not measurably affect the spectrum from the laser facet. This signifies good isolation between the two devices. However, the spectrum from the modulator facet (Fig. 5.7b) changes drastically with modulator bias. As can be seen from this figure, both the spontaneous emission profile, and the power measured at the lasing wavelength change with modulator bias. It is the change in the spontaneous emission that is used to calculate the absorption of the modulator. The calculated absorption (facet power difference) as a function of wavelength for different modulator bias is shown in Fig. 5.8. As previously discussed, the 4dB offset from zero absorption in the modulator section at 1600nm is caused by a combination of the coupling losses between the sections, the fibre coupling losses, and the modulator waveguide/residual absorption losses. It can be clearly seen that the absorption band edge moves by $\sim$40nm as the voltage is varied from 0V to -3.0V, and at 1570nm the absorption changes by approximately 9dB for a 3V bias change on the modulator. From this graph, it can be seen that

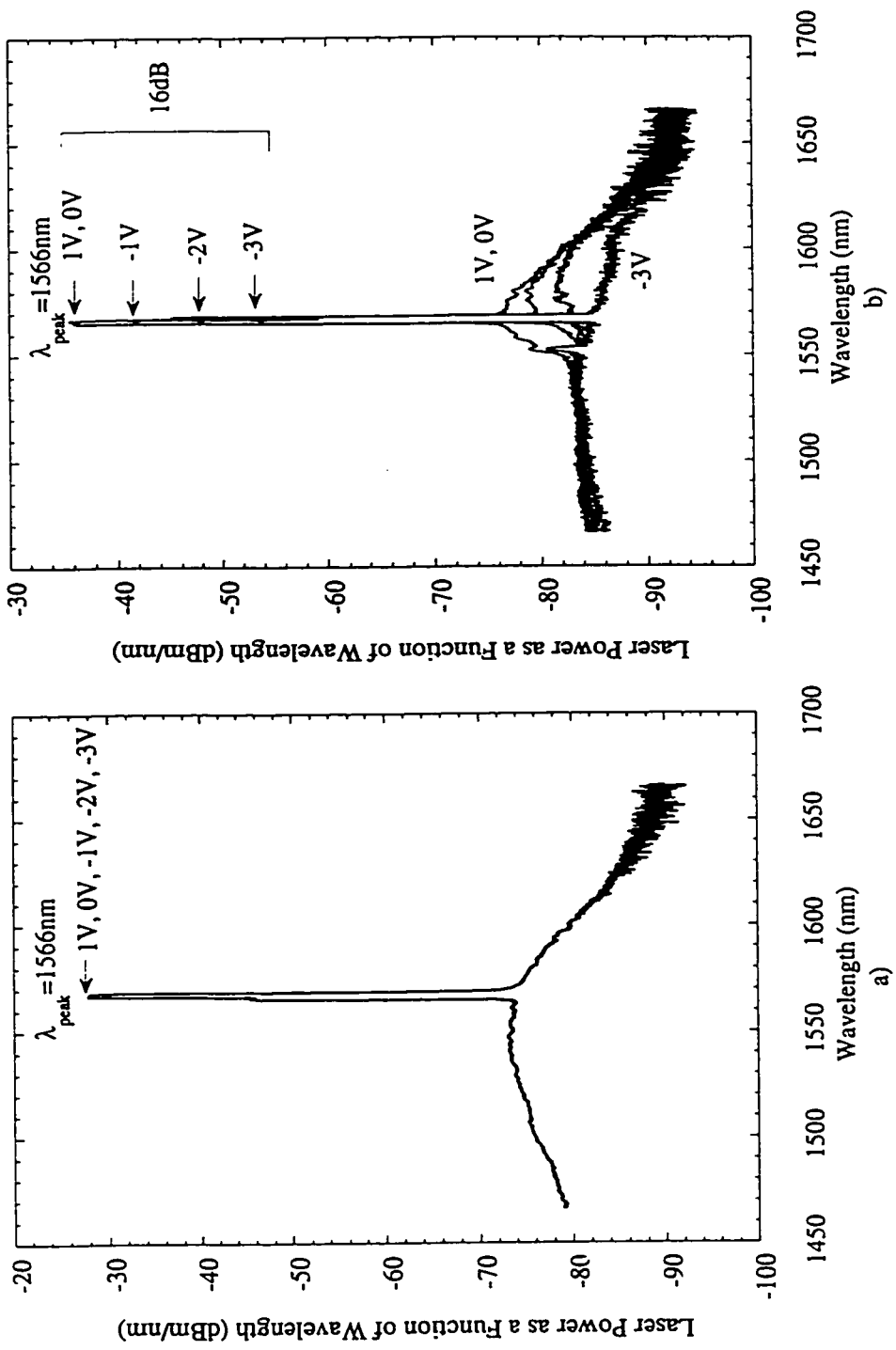

Figure 5.7: Spectra as measured from (a) the laser facet and from (b) the modulator facet for different modulator bias. The device has a 600μm laser, 400μm modulator and the ridge width is 2μm. The lasing wavelength is 1566 $\pm$ 2nm.

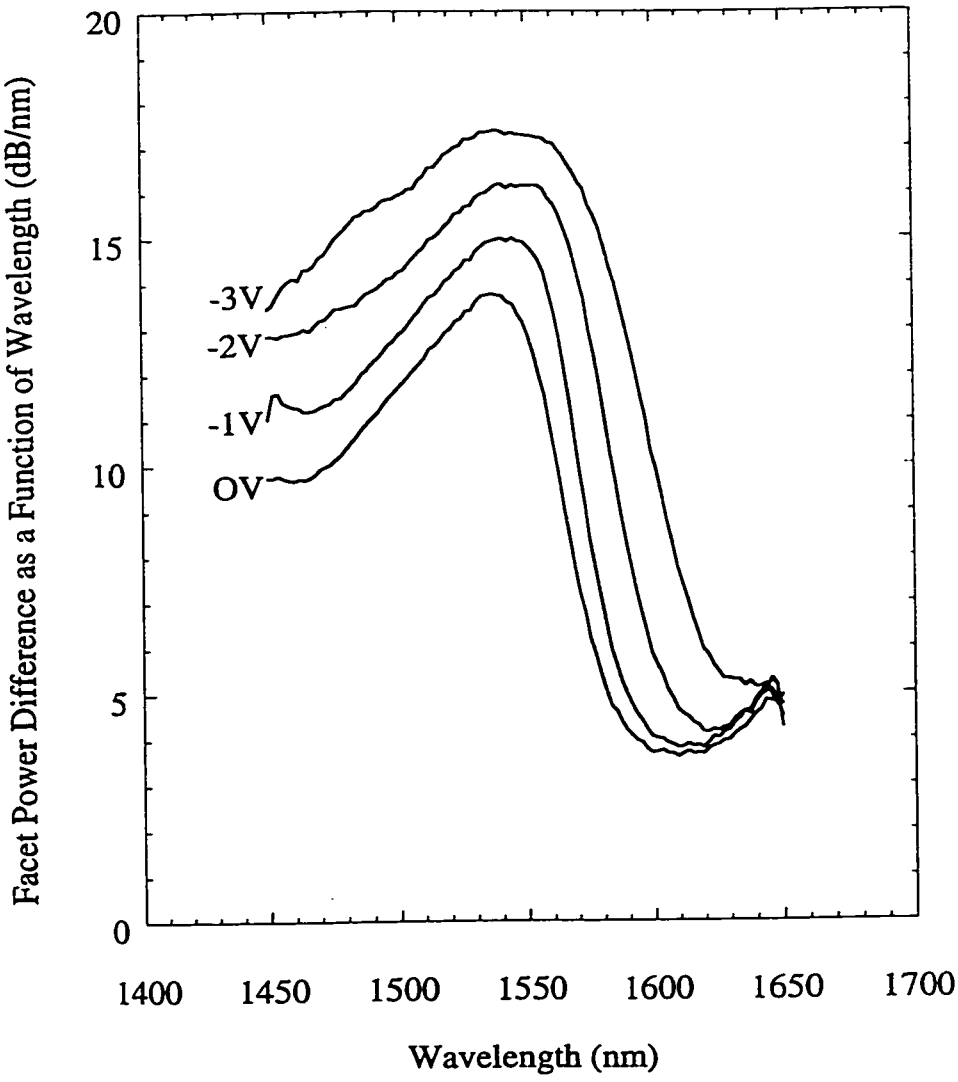

Figure 5.8: Approximate absorption spectra of a 400μm modulator for modulator biases of -3, -2, -1, and 0V. (Calculated using the laser's spontaneous emission).

the laser wavelength should be between approximately 1570nm and 1580nm to give the largest change in absorption for a modulator bias change of 0V to -3V for this modulator design.

As discussed earlier, in making the absorption measurement it is assumed that the spontaneous emission spectrum is not perturbed by the modulator either

due to current leakage or due to light being coupled back into the laser section. This is justified by Fig. 5.7a which shows no significant change to the spontaneous emission profile at different modulator biases.

5.3.3 Output Power vs. Modulator Voltage

The output power was measured as a function of modulator bias. Sample light-current (L-I) curves for different modulator bias are shown for the laser facet in Fig. 5.9a and for the modulator facet in Fig. 5.9b. (The measured detector current is proportional to the incident power.) From Fig. 5.9a it can be concluded that the modulator is not significantly perturbing the laser since the threshold and the slope of the L-I curves are nearly identical for the different modulator biases. The small kinks in the slope of the L-I curves are caused by modulator facet feedback who's magnitude changes with both modulator and laser bias. Discrete devices were kink-free up to 100mA as discussed in section 5.1. Unlike the L-I curve measured from the laser facet, the L-I measured from the modulator facet (Fig. 5.9b) changes significantly with modulator bias: the measured power is decreased by 12dB as the modulator bias is varied from 0 to -3V. For completeness, Fig. 5.10 shows the relative transmission of the modulator (i.e. the extinction ratio) as a function of modulator bias for a 2μm ridge width device with a 400μm modulator. This is how modulator absorption plots are normally presented in the literature. The maximum absorption for this device is -11.8dB at -3V. Industry normally requires an extinction ratio of $\sim$12dB for telecommunications applications. From these graphs it can be seen that the modulator can be used to decrease the light out of one facet without significantly perturbing the laser when a 2μm RW is used. However, the optical isolation was found to vary with the ridge width with the 4μm devices being more sensitive to feedback from the front facet than the 2μm devices. As stated earlier, the optical

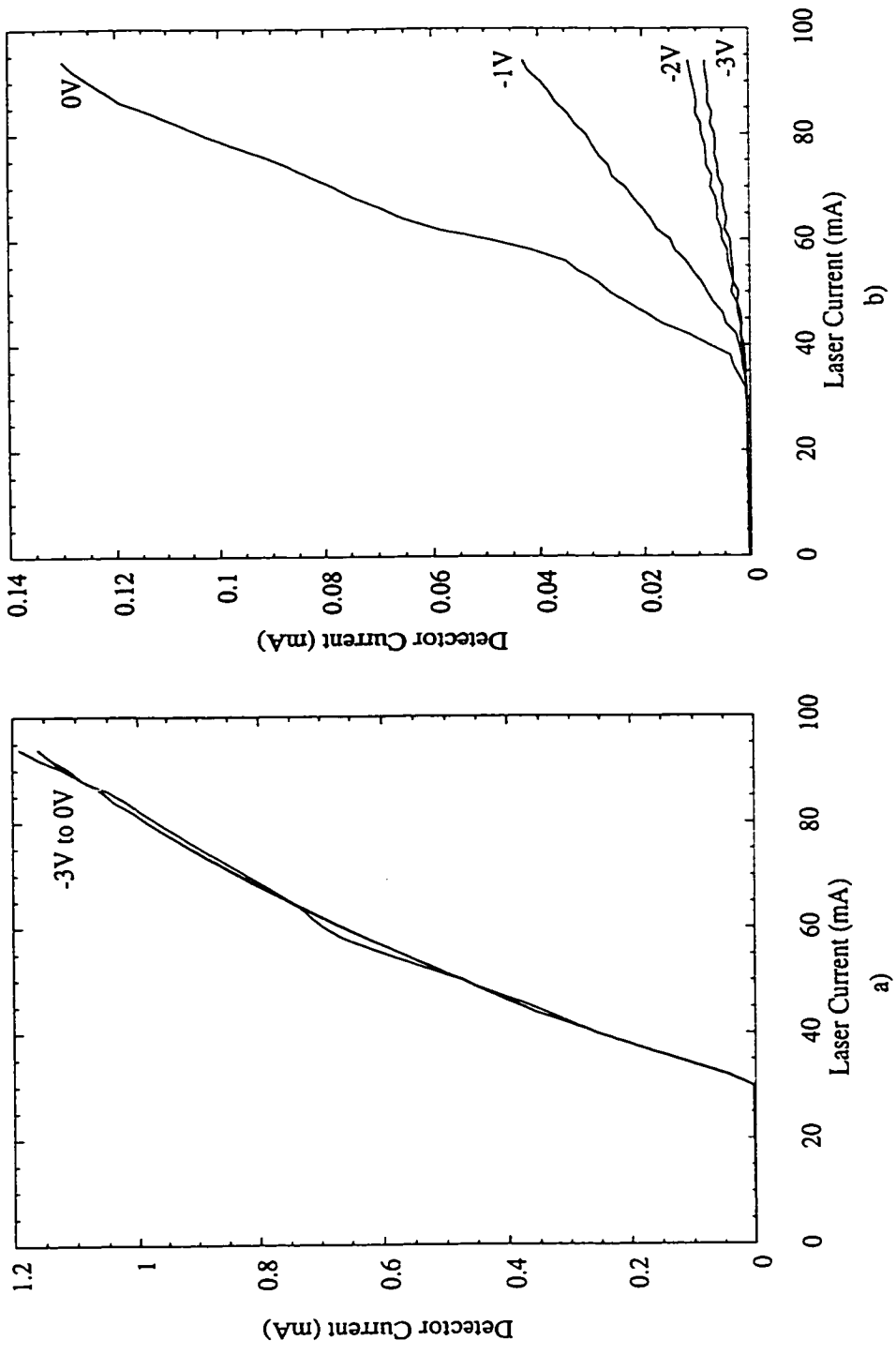

Figure 5.9: L-I curve as measured from (a) the laser facet and from (b) the modulator facet for different modulator bias (0 to -3V). The device has a 600μm laser, 400μm modulator and the ridge width is 2μm.

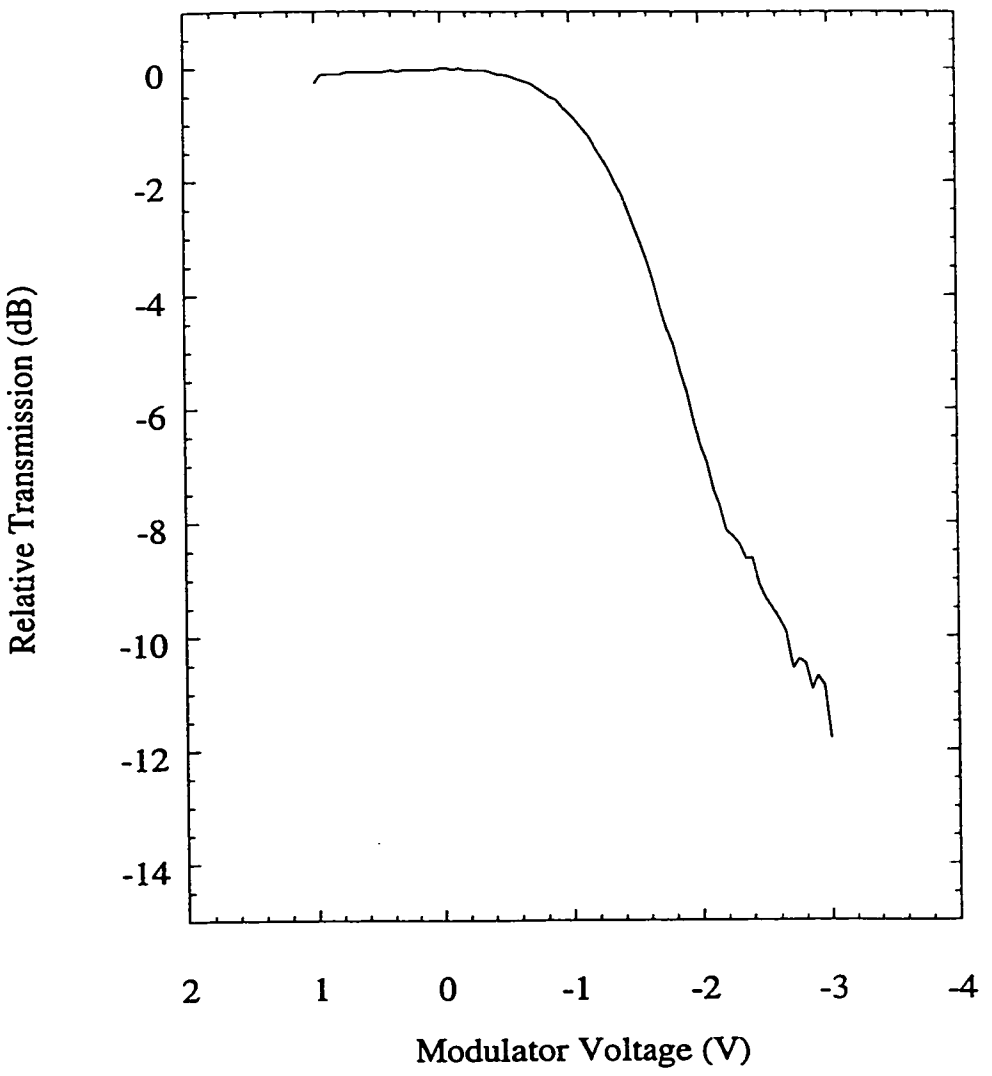

Figure 5.10: Relative modulator transmission as a function of modulator bias. The device has a 600μm laser, 400μm modulator and the ridge width was 2μm.

feedback produces kinks in the L-I curve and mode hops in the output spectrum. AR coatings are expected to improve the optical isolation.

5.3.4 Electrical Characterization

The electrical (I-V) characteristics of the modulator as a function of laser bias were measured and the results are shown in Fig. 5.11. The laser was held at a constant voltage, which ensures that the laser remains at the same operating point regardless of the magnitude of the leakage current and that the same amount of light enters the modulator for all modulator bias. An I-V of the modulator with the laser unbiased is shown as the dotted line (which is equivalent to the modulator dark current). As can be seen from the difference between the modulator I-V curves for the unbiased laser and the 0V biased laser, even with a 2.7kΩ resistance between the contacts, the leakage current between the two sections is a significant fraction of the modulator current. This is because the differential resistance of the modulator section alone is on the order of 10kΩ which is good from a modulator standpoint–ideally, the only modulator current present would be caused by the photo-generated carriers. However, for the devices shown in Fig. 5.11, the modulator resistance is greater than the resistance between the contacts of the two devices (2.7kΩ) and might pose a problem when the device is modulated. Future work should investigate methods to increase the electrical isolation and increase the optical coupling between the laser and the modulator.

It is difficult to separate the modulator photocurrent from the contact leakage current in Fig. 5.11. To obtain a better idea about the magnitude of the photocurrent, one can plot the modulator current as a function of laser current as illustrated in Fig. 5.12. Below threshold there should be very little photocurrent so, at this bias, the modulator current is approximately equal to the dark current and the leakage current. By extrapolating the below-threshold modulator current to a laser current of 100mA, one can estimate the combined dark current and device leakage current as -4.6mA

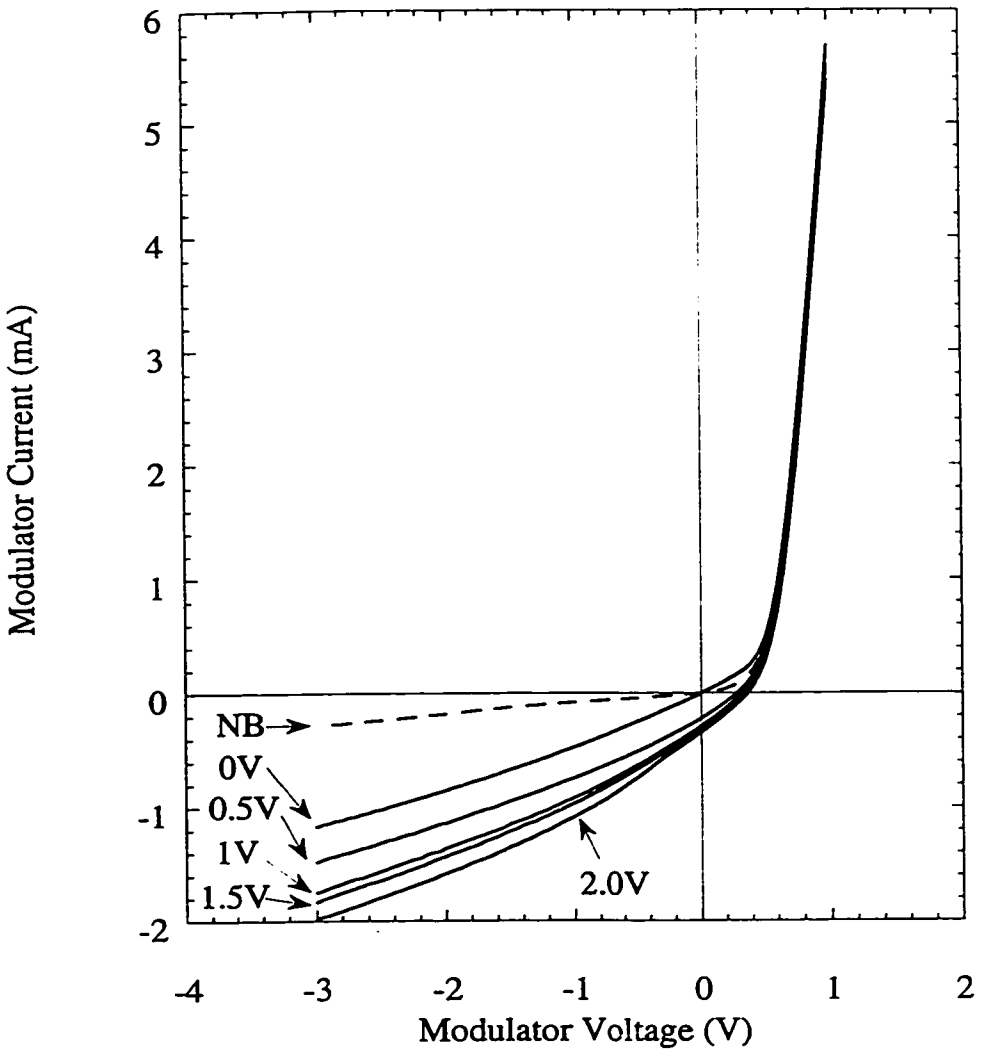

Figure 5.11: I-V curve for different laser bias. The dashed line represents the case when the laser contact is open circuited. The device has a 600μm laser, 400μm modulator and the ridge width was 2μm.

for a -3V modulator bias. The total modulator current at this bias is -8.7mA. For a modulator bias of -3V, the dark current is -0.3mA (from Fig. 5.11) which makes the device leakage current -4.3mA and the photocurrent -4.1mA; therefore, the leakage current is a large fraction of the total modulator current. Device isolation should be improved before the modulation characteristics of the device are examined.

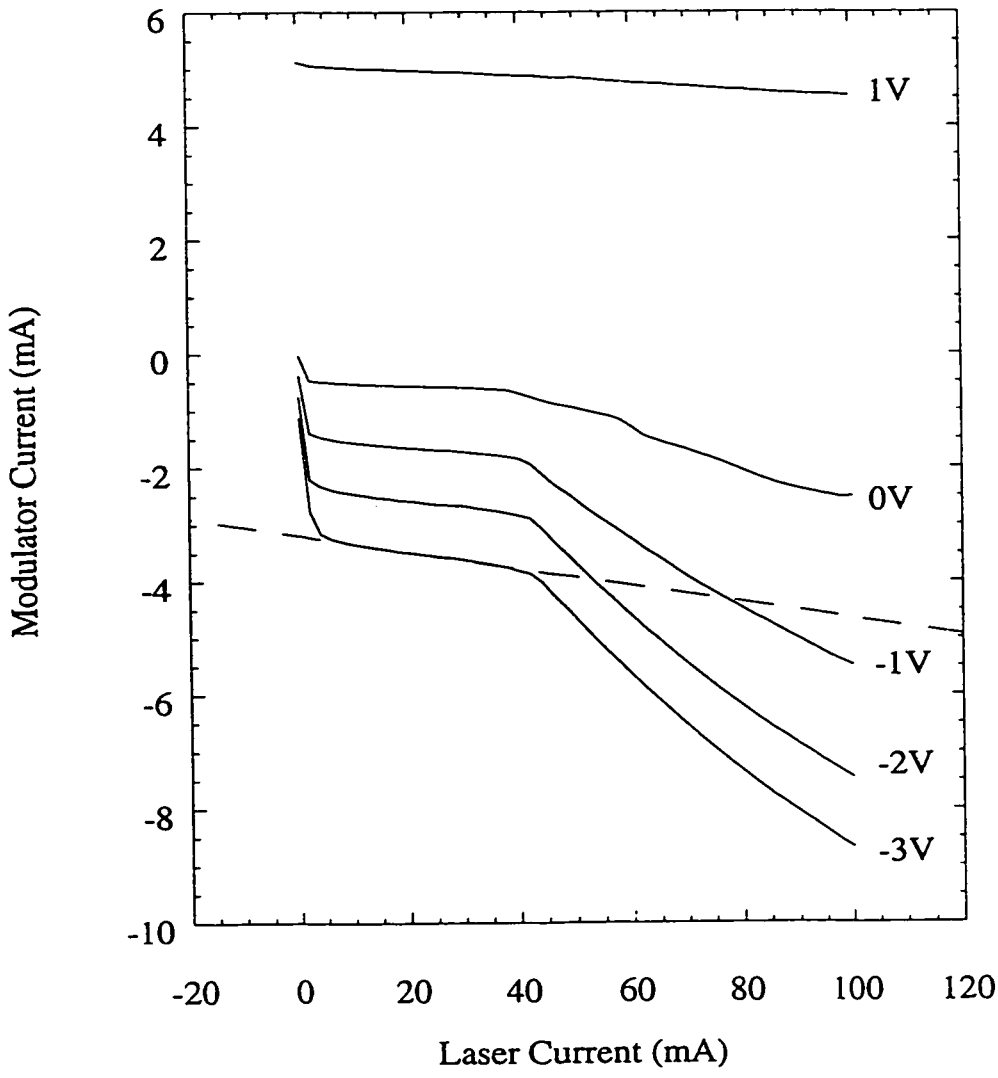

Figure 5.12: Modulator current as a function of laser current. The device has a 600μm laser, 400μm modulator and the ridge width was 2μm. The dashed line is an extrapolation of the combined dark and leakage currents and is used to estimate their values at 100mA.

5.4 Comparison with Previously Published Work

Integrated lasers and modulators have been fabricated by various research groups as reported in the literature. The integration has been performed by using localized heating [4, 5], selective-area epitaxy [10, 9, 16], by etching and regrowth [54], and by QWI (by using phosphorus doped oxides) [55]. A direct comparison with previously published work is difficult because the device operation depends on many parameters such as: the difference in the transition energy of the quantum wells in the laser and modulator; the difference between the lasing wavelength and the absorption edge of the modulator; the number of quantum wells; doping profiles of the devices; layer thicknesses (especially the intrinsic layer thickness); optical confinement; the quality of the contacts; and the quality of the diode. Also, the majority of devices in the literature are buried heterostructure (BH) devices, which have a larger optical confinement factor that leads to a higher absorption of the optical mode for a given bias. In addition, devices with AR coatings also exhibit a higher extinction ratio due to reduced bandfilling effects. (Light reflected by the modulator facet is absorbed by the quantum wells and generate carriers which decrease the absorption of the modulator.) Even so, several previously published devices are discussed in this section.

The 400μm, 3 quantum well, RWG modulators in this thesis show an extinction ratio that ranges from -9 to -16dB for a -3V applied bias at the lasing wavelength. For comparison, a 5 QW BH device was grown by selective-area epitaxy by Tanbun-Ek et al. [9], and has a -15dB extinction ratio at -3V. The exact structure is not given, neither is the PL wavelengths of two sections, nor the lasing wavelength of the laser, so it is difficult to determine the exact source of the difference between the device in the paper, and those in this thesis. One definite difference is that the

modulator facet has an AR coating.

A similar, AR-coated, 5 QW device was fabricated by Aoki et al. [16]. Their 260μm long modulator showed a 25dB extinction ratio at a 3V bias which is significantly better than the devices illustrated in this thesis. For this device, there was a 75nm difference in the PL wavelength of the laser (λ_{pl} = 1565nm) and modulator (λ_{pl} = 1490nm). Also, the laser lased at 1571.9nm which places the absorption edge approximately 15nm further from the lasing wavelength than for the laser design investigated in this thesis. However, once again, the complete structure was not given, so it is difficult to comment on the differences in the laser design. However, it appears that the QCSE has a stronger dependence on bias than in the structures investigated in this thesis. This could be due to: the quality of the diode (magnitude of leakage currents, etc.); the composition of the wells and barriers; the thickness of the intrinsic region in the device; or the fact that they are using a BH type structure.

Clearly further optimization of the devices investigated in this thesis is required. This work involved the development of the first set of integrated DFB lasers and EA modulators ever fabricated at McMaster University, and the first devices ever fabricated by He*-InP induced intermixing. The principle of the device has been demonstrated, and further device optimization is left for future work.

5.5 Device Summary

Integrated DFB lasers and electroabsorption modulators have been fabricated involving He*-InP defect induced QWI to enhance the annealing induced blue-shift in the modulator section. The lasing wavelength of the discrete DFB varies from 1568nm to 1572nm depending of the ridge width, and the stop band is 1.9nm wide which signifies that the grating is relatively strong ($\kappa L > 1$). For a discrete modulator,

the absorption band edge shifts by ~40nm as the voltage is varied from 0V to -3.0V.

The current integrated device design with 3QW and a 400μm modulator has an extinction ratio of 10-16dB when -3V is applied to the modulator. The extinction ratio varies with ridge width primarily due to the different lasing wavelengths (which is due to the different modal indices) of the devices. (The 2μm lasers lased at 1568nm, while the 4μ lasers lased at 1572nm.) The extinction ratio can be modified in future designs by:

1. increasing the number of quantum wells
2. by using a longer modulator
3. by further optimizing the design to increase the optical mode overlap with the quantum wells
4. by increasing the separation between the modulator band edge and the laser gain peak and/or the lasing wavelength
5. by increasing the number of He*-InP defects in the modulator which will act to decrease band-filling effects and to increase the absorption of the quantum wells for a given bias.
6. or by changing the design and improve the processing techniques to minimize the dark current of the modulator. (The dark current acts to reduce the QCSE).

The benefits and difficulties of each of these techniques were discussed in detail section 2.8.

Methods of device isolation other than an isolation trench need to be investigated in future work. For the devices investigated, the resistance between the contacts ranged from 2-20kΩ. However, the measured differential resistance of the

modulator alone was 10kΩ which means that the majority of the modulator current is due to current leakage between the laser and the modulator section. This leakage current will cause a change in the laser bias when the modulator is modulated, and provide additional carriers that will need to be swept out of the modulator when it is switched states. Also, it has been found in other work [48] that the optical coupling varies from 40-60% depending on the geometry of the trench and the ridge width. Using a different method for device isolation that does not result in the large optical losses would be a beneficial technique for improving device performance by increasing the optical power exiting the modulator facet.

The modulator facet reflectivity was also found to be a problem (particularly for the 3 and 4μm ridge widths) and causes kinks in the L-I characteristics of the laser. This effect can be eliminated in future designs by using an AR coating on the modulator facet.

Chapter 6

Conclusions

This was the first investigation into the properties of He*-InP defect induced QWI, as well as the first time devices have been fabricated by this novel intermixing technique. The devices investigated were an integrated DFB laser and EA modulator. The intermixing process uses defects from within a layer of InP grown by He-plasma-assisted gas source molecular beam epitaxy to selectively enhance the intermixing in the modulator section of the device. The main results are summarized in this chapter, and the required future work is discussed.

6.1 He*-InP Defect Induced Intermixing Summary

This was the first investigation into the annealing properties of material containing both QWs and He*-InP. It was discovered that defects within the He*-InP layer can be used to selectively enhance the intermixing experienced by quantum wells. The He*-InP QWI process was found to have some unusual properties. It was observed that as the He*-InP layer thickness increases, the PL intensity and the amount of quantum well intermixing decrease when the He*-InP layer is grown on the 1.15Q waveguide layer of a laser structure. By using a 700Å He*-InP layer, it was found to be possible induce a 29nm relative blue-shift between adjacent areas that

had no He*-InP layer. This is sufficient for fabricating an integrated DFB laser and EA modulator.

Quantum well intermixing using He*-InP was found to have several benefits over other intermixing procedures. The main advantage of this technique is that it is possible to regrow over material that has been subjected to a high-temperature anneal–we have yet to find a way to accomplish this using dielectric-enhanced intermixing. Defect enhanced quantum well intermixing using He*-InP also introduces non-radiative defects into the quantum wells. Evidence of this was seen in the large reduction in the photoluminescence and the electroluminescence intensities. These defects decrease the carrier lifetime in the quantum wells, and are therefore useful at reducing effects such as carrier screening which results in absorption saturation. To date, no research has been performed to investigate the scale of the reduction of the carrier lifetime and this research is also left for future work.

6.2 Device Summary

The devices fabricated in this work were an integrated DFB laser and electroabsorption modulators and were the first devices to ever to be fabricated by using He*-InP defect induced intermixing. This result proves the feasibility of the intermixing technique for device applications. Several device fabrication techniques were refined in the development of the integrated DFB laser and EA modulator:

1. The He*-InP defect induced intermixing technique was adapted to the device fabrication procedure

2. A technique was perfected to facilitate the regrowth (by MBE) over material that had experienced a high temperature (800 °C) anneal.

3. A technique to selectively pattern the grating by using a semiconductor mask was also developed.

4. The number of processing steps required for device fabrication was minimized by using the same layer for the intermixing and as the etch mask so that only one more mask step than that required for DFB laser fabrication was required.

These techniques were then combined to fabricated the integrated device.

The final device design used a 700Å He*-InP layer, along with a 800 °C, 30s anneal to provide a relative blue-shift of 29nm between the laser and modulator sections. Only one more mask step to fabricate the integrated device than discrete DFB lasers was required. This was due to the dual use of the He*-InP layer which both induces the intermixing and acts as the etch mask required to prevent grating formation in the modulator section. However, an extra regrowth was required to grow the sacrificial layers needed to protect the regrowth interface during the anneal. The threshold currents of discrete, 600μm long DFB lasers ranged from 18 to 35mA depending on ridge width and its placement on the wafer. The lasing wavelength varied from 1568nm for a 2μm ridge width to 1572nm for a 4μm ridge width. The absorption edge of a 400μm modulator was measured and was found to shift by 40nm as the voltage is varied from 0V to -3.0V, and that at 1570, the absorption changes by approximately 10dB for a 3V bias change on the modulator. Integrated devices exhibited an extinction ratio of 10-16dB when 3V was applied, and varies with ridge width due to the different lasing wavelengths. The electrical isolation varied from 2-20kΩ and depended on the width of the isolation trench (which varied from 5-15μm). It was found that even though the resistance between the contacts was high, the leakage current was on the same order as the photocurrent in the modulator which will be detrimental to the modulation characteristics of the device. Optical feedback

from the modulator facet was found to cause mode hopping and kinks in the L-I curves. The feedback problem was more severe for the 4μm ridge widths since the optical coupling between the two cavities is greater. This problem can be corrected by growing a antireflection coating on the modulator facet. Further device optimizations can be performed, such as increasing modulator length or increasing numbers of quantum wells, to try to increase the extinction ratio. The electrical isolation and optical coupling between the laser and modulator should also be improved in future designs.

6.3 Future Work

The research in this thesis has shown that it is possible to use He*-InP for quantum well intermixing to fabricated integrated devices. However, this was only the first investigation into the material properties and much more research into both the material characteristics and process optimization needs to be done. Future work needs to focus on understanding the He*-InP defect intermixing process and how it interacts with the thermally induced intermixing. Layer thicknesses and anneal temperatures and times need to be optimized to obtain an ideal intermixing for a particular application. Identification of the defects would be useful in increasing the understanding of the intermixing process. Samples with different amounts of doping could also be investigated in an attempt to determine the charge state of the defect involved in the intermixing process. An investigation of the effectiveness of the He*-InP at blocking the thermal blue-shift should be done. A reduction of the thermal blue-shift would be beneficial by adding to the controllability of the annealing procedure. Even if the thermal blue-shift is not completely suppressed, this technique would also be useful for increasing the relative amount of intermixing between the

different integrated photonic devices. Research should also examine quantitatively the effects of adding non-radiative defects to the active region. One should determine the change in absorption caused by introducing the non-radiative defect into the quantum wells (due to the reduction in absorption saturation) as well as determine the recombination rate of the carriers within the active region of the device.

The reproducibility of the He*-InP intermixing process needs to be investigated further in future studies since this was a first investigation into the process and a thorough investigation into the reproducibility of the process was not done at this time. This type of QWI is expected to be more reproducible than dielectric-enhanced intermixing for several reasons. First, the layer responsible for the intermixing is an epilayer that is grown at the same time as the quantum wells. Dielectric-enhanced intermixing is based on a strained system made of materials with vastly different thermal expansion coefficients–one of which is a film grown by a low vacuum (~650mtorr) PECVD system. It is possible that strain at the dielectric and semiconductor interface is driving the dielectric-enhanced intermixing process. If that is the case, then the interface quality would greatly influence the reproducibility of the dielectric-enhanced intermixing process. Second, because molecular-beam-epitaxy is a highly controllable process taking place in a high vacuum chamber, using an epilayer to enhance QWI is expected to make the intermixing process more reproducible. This process does not introduce measurable strain or impurities into the system (since the intermixing is caused by defects from an epilayer of InP), and ensures a reproducible interface between the He*-InP layer and the remaining structure since the epilayer is grown at the same time as the quantum wells. Further reproducibility studies need to be performed in future work.

The device characteristics can also be improved. The relative positions be-

tween the absorption edge of the modulator and the lasing wavelength of the laser can be optimized to maximize the extinction ratio while minimizing the turn-off voltage required for the modulator. Developing a device with more quantum wells so that a larger extinction ratio is possible while maintaining a short modulator would be beneficial for microwave modulation measurement. It would be worthwhile to investigate methods to improve the electrical isolation and the optical coupling. One possibility is to change the doping profile so that the layers below the etch-stop are not doped. This would enable a narrower trench to be etched with the same electrical isolation. However, the series resistance of the device will be increased which is detrimental to the laser and modulator performance. Due to the compromise required between electrical isolation and optical coupling, a ridge-waveguide structure with an isolation trench is not an ideal design for device integration. Instead of using an isolation trench, an ion implanted region can be used to increase the resistivity between the devices. Since the ridge is continuous between the two devices, large optical coupling is still possible. Another alternative is a buried-heterostructure laser which provides even more flexibility in the device design, though the fabrication procedure is more difficult.

Future work should also focus on obtaining a process in which the anneal is performed after the regrowth of the waveguide and contact layers since such a procedure would simplify the device fabrication. Annealing after the regrowth was not used for the devices in this thesis since early intermixing experiments have shown the regrowth interface to have an unpredictable influence on the thermally-induced intermixing–especially when the regrowth interface contains a grating. However, it should be noted that the quality of the regrowth has been improved since the early experiments of annealing after the regrowth, so it might now be possible to anneal

after the regrowth and still have a properly matched grating. If so, the fabrication step involving the regrowth of the sacrificial layers required for the anneal can be eliminated (i.e. the anneal can be performed after the upper waveguide layers and contact is grown). The removal of the second regrowth would simplify processing, so future work should investigate procedures for improving the reproducibility of intermixed samples containing gratings.

Last of all, the modulation characteristics of the modulator should be examined after further device optimization. The non-radiative defects introduced by the intermixing technique might prove be useful for decreasing transient effects when the device is modulated.

Appendix A

Matrix Methods for Calculating Electrical and Optical Confinement

Matrix methods are an extremely flexible and highly effective numerical technique for calculating optical and electronic wavefunctions for arbitrary structures. The matrix method begins with the time independent wave equation [56, 57]

$$\frac{d^2\psi(x)}{dx^2} + R\psi(x) = 0 \tag{A.1}$$

where R is a constant, and is determined by the physics of the problem. This wave equation has a generalized solution:

$$\psi_j(x) = A_j \cdot e^{p_j(X)} + B_j \cdot e^{-p_j(X)} \tag{A.2}$$

with A and B representing the magnitudes of the forward and backward traveling waves respectively, and $p_j(x)$ defined as a complex function representing the propagation constant in the material. Matrix methods involve relating these magnitudes at the boundaries of layers j and $j+1$. This is accomplished by writing a generalized matrix:

$$\begin{bmatrix} A_{j+1} \\ B_{j+1} \end{bmatrix} = M_j \cdot \begin{bmatrix} A_j \\ B_j \end{bmatrix} \tag{A.3}$$

where M_j is a 2 x 2 matrix.The matrix elements of M_j is determined by the propagation characteristics in the material and the required boundary conditions. By matrix

multiplication, it is possible to find the relationship between the ingoing and outgoing waves at the boundaries of the system:

$$\begin{aligned}\begin{bmatrix} A_{N-1} \\ B_{N-1} \end{bmatrix} &= M_{N-2} \cdot M_{N-1} \cdot \cdots \cdot M_1 \cdot M_0 \cdot \begin{bmatrix} A_0 \\ B_0 \end{bmatrix} \\ &= M \cdot \begin{bmatrix} A_0 \\ B_0 \end{bmatrix} \end{aligned} \tag{A.4}$$

where M is the matrix describing the whole system, and is a 2x2 matrix:

$$M = \begin{bmatrix} \alpha_{11} & \alpha_{12} \\ \alpha_{21} & \alpha_{22} \end{bmatrix} \tag{A.5}$$

In any situation where the wavefunction is bounded in space, one requires that $A_0 = 0$ and $B_{N-1} = 0$ so that x diminishes to zero at $\pm\infty$. For this to be true, we must have

$$\alpha_{22}(R) = 0 \tag{A.6}$$

It is then a simple matter of using numerical techniques to find the values of R which satisfy this criteria [56].

A.1 The Application of the Matrix Method to the Schrödinger Equation

A.1.1 Theory

The matrix method is easily applied to the one-dimensional time-independent Schrödinger equation [56]. In this case, the Schrödinger equation is given by:

$$\left[\frac{-h^2}{8\pi^2}\frac{d}{dx}\frac{1}{m^*(x)}\frac{d}{dx} + V(x)\right]\psi(x) = E\psi(x) \tag{A.7}$$

where m^* is the effective mass, h is Planck's constant, V is the potential, and E is the energy eigenvalue. As previously discussed, we can assume a solution of (A.2). In this situation we find that

$$p_j(x) = \begin{cases} \Gamma_0 \cdot x & (j = 0) \\ \Gamma_j \cdot (x - x_{j-1}) & (j > 0) \end{cases} \tag{A.8}$$

where

$$\Gamma_j(E) = i \cdot \sqrt{\frac{8pi^2 \cdot m_j^*}{h^2} \cdot (E - V_j)} \tag{A.9}$$

The requirements on the boundary conditions are:

$$\psi_{j-1}(x_{j-1}) = \psi_j(x_{j-1}) \tag{A.10}$$

$$\frac{1}{m_{j-1}^*} \cdot \frac{d}{dx}\left[\psi_{j-1}(x_{j-1})\right] = \frac{1}{m_j^*} \cdot \frac{d}{dx}\left[\psi_j(x_{j-1})\right] \tag{A.11}$$

as shown by [58]. The notation $\psi_{j-1}(x_{j-1})$ represents the value of the wavefunction in layer $(j-1)$ evaluated at position of the boundary between ψ_{j-1} and ψ_j (i.e. at x_{j-1}). Using this, it is possible to calculate the elements for matrix for each individual layer, M:

$$\alpha_{11_j} = \frac{1}{2} e^{p_j - p_{j+1}} \left(1 + \frac{m_{j+1}^*}{m_j^*} \frac{\Gamma_j}{\Gamma_{j+1}}\right)\Bigg|_{x=x_j} \tag{A.12}$$

$$\alpha_{12_j} = \frac{1}{2} e^{-p_j - p_{j+1}} \left(1 - \frac{m_{j+1}^*}{m_j^*} \frac{\Gamma_j}{\Gamma_{j+1}}\right)\Bigg|_{x=x_j} \tag{A.13}$$

$$\alpha_{21_j} = \frac{1}{2} e^{p_j + p_{j+1}} \left(1 - \frac{m_{j+1}^*}{m_j^*} \frac{\Gamma_j}{\Gamma_{j+1}}\right)\Bigg|_{x=x_j} \tag{A.14}$$

and

$$\alpha_{22_j} = \frac{1}{2} e^{p_{j+1} - p_j} \left(1 + \frac{m_{j+1}^*}{m_j^*} \frac{\Gamma_j}{\Gamma_{j+1}}\right)\Bigg|_{x=x_j} \tag{A.15}$$

From here, it is a simple matter to multiply all the individual matrices together to find the matrix for the complete system. As stated earlier in this appendix, the boundary conditions require that $\alpha_{22}(E) = 0$. Numerical techniques can be used to calculate the values of E which satisfy this boundary condition thereby calculating the energy levels in the quantum well.

A.1.2 Material Parameters

To accurately calculate the QW energy one must accurately know the material parameters [59, 60].

For an unstrained layer of $In_{(1-x)}Ga_xAs_yP_{(1-y)}$ on InP, the band-gap energy (in eV) is calculated by:

$$E_g(y) = 1.35 - 0.738y + 0.138y^2 \tag{A.16}$$

where y is the composition given by $In_{(1-x)}Ga_xAs_yP_{(1-y)}$ [61]. Once strain is added, the degeneracy between the light holes and heavy holes are lifted. From a paper by Chuang [60] we find that the transition energy is given by:

$$E_{g_{hh}} = E_g(y) - \delta E_{hy} + \zeta \tag{A.17}$$

for the heavy holes and

$$E_{g_{lh}} = E_g(y) - \delta E_{hy} - \zeta \tag{A.18}$$

for the light holes where δE_{hy} is the change in the energy gap due to hydrostatic strain and is calculated by:

$$\delta E_{hy} = -2a\left(1 - \frac{C_{12}}{C_{11}}\right)\varepsilon \tag{A.19}$$

and the change due to the shear strain is given by:

$$\zeta = \frac{1}{2}\delta E_{sh} = -2b\left(1 + \frac{2C_{12}}{C_{11}}\right)\varepsilon \tag{A.20}$$

where $a(y)$ is the lattice constant and $\varepsilon = (a_0 - a/a_0)$ is the strain, and a and b are the deformation potentials (in eV) and C_{11} and C_{12} are the elastic constants ($\times 10^{11}$dyn/cm^2). The values for the elastic constants in $In_{(1-x)}Ga_xAs_yP_{(1-y)}$ are given in a paper by Macrander [59]:

$$C_{11}(x,y) = -0.186y + 3.89x - 0.42xy + 10.19 \tag{A.21}$$

and

$$C_{12}(x,y) = -1.2y + 0.49x + 0.29xy + 5.73 \tag{A.22}$$

an the deformation potential coefficients are given by

$$a(x,y) = 0.35y - 3.25x - 0.52xy - 6.35 \tag{A.23}$$

and

$$b(x,y) = 0.20y + 0.35x - 0.25xy - 2 \tag{A.24}$$

as calculated from Vegard's law.

Using the matrix approach it is possible to calculate the electron and hole levels for any arbitrary structure. A sample calculation using this method is illustrated in Fig. 1.3 where the energy levels in square and an intermixed quantum well are calculated .

A.2 The Application of the Matrix Method to the Optical Wave Equation

A.2.1 Theory

The matrix method is also easily applied to the one-dimensional wave equation in optics [57]. It is an identical approach to that used for the time-independent Schrödinger equation. The wave equation is given by:

$$\frac{d^2}{dx^2}E + {k_0}^2 n^2 E = 0 \tag{A.25}$$

where n is the refractive index, k_0 is the free space propagation constant, and E is the electric field. As previously discussed, we can assume a solution of (A.2). In this situation we find that the equations become:

$$\Gamma(\beta)_j = -\sqrt{\beta^2 - k^2 {n_{o_{j+1}}}^2} \tag{A.26}$$

where β is the mode propagation constant and $k = 2\pi n/\lambda$ is the wave propagation constant. The required boundary conditions are:

$$E_{j-1}(x_{j-1}) = E_j(x_{j-1}) \tag{A.27}$$

$$\frac{d}{dx}[E_{j-1}(x_{j-1})] = \frac{d}{dx}[E_j(x_{j-1})] \tag{A.28}$$

As for the Schrödinger equation, the notation $E_{j-1}(x_{j-1})$ represents the value of the electric field in layer $(j-1)$ evaluated at position of the boundary between E_{j-1} and E_j (i.e. at x_{j-1}). Using the boundary conditions, the matrix elements become:

$$\alpha_{11_j} = \frac{1}{2}e^{p_j - p_{j+1}}\left(1 + \frac{\Gamma_j}{\Gamma_{j+1}}\right)\Bigg|_{x=x_j} \tag{A.29}$$

$$\alpha_{12_j} = \frac{1}{2}e^{-p_j - p_{j+1}}\left(1 - \frac{\Gamma_j}{\Gamma_{j+1}}\right)\Bigg|_{x=x_j} \tag{A.30}$$

$$\alpha_{21_j} = \frac{1}{2}e^{p_j + p_{j+1}}\left(1 - \frac{\Gamma_j}{\Gamma_{j+1}}\right)\Bigg|_{x=x_j} \tag{A.31}$$

and

$$\alpha_{22_j} = \frac{1}{2}e^{p_{j+1} - p_j}\left(1 + \frac{\Gamma_j}{\Gamma_{j+1}}\right)\Bigg|_{x=x_j} \tag{A.32}$$

Once again, the boundary conditions require that $\alpha_{22}(\beta) = 0$. This equation can also be solved numerically.

A.2.2 Material Parameters

To accurately calculate the mode profile one must accurately know the material parameters.

It has been found that for $In_{(1-x)}Ga_xAs_yP_{(1-y)}$, the phase index is described by:

$$\begin{aligned} n(\Delta E, y) &= 3.425 + 0.94\Delta E + 0.952(\Delta E)^2 \\ &\quad + (0.255 - 0.257\Delta E)y \\ &\quad - (0.103 - 0.092\Delta E)y^2 \end{aligned} \tag{A.33}$$

where ΔE is the energy separation from the band gap and is valid in the range $-0.2\text{eV} \leq \Delta E \leq 0\text{eV}$. (Note that this is not valid for InP at a wavelength of $1.55\mu\text{m}$. For this case, the index was taken to be 3.16.) The group index is described by the equation [61]

$$\begin{aligned} n(\Delta E, y) &= 3.425 + 1.88\Delta E + 2.86(\Delta E)^2 \\ &\quad + (0.255 - 0.514\Delta E)y - (0.103 - 0.184\Delta E)y^2 \\ &\quad + 0.94E - 1.9\Delta E - 0.257Ey + 0.092Ey^2 \end{aligned} \tag{A.34}$$

This matrix approach was used to calculate the mode profile for the MQW stack illustrated in Fig. 2.3.

Appendix B

Wave Propagation in Periodic Media

This appendix includes a brief summary of the equations found in the literature for the calculation the transmission and reflection profiles of Bragg gratings, DFB modes and grating coupling coefficients. There are 2 main methods seen in the literature for analyzing gratings: the truncated Floquet-Bloch [62] and coupled-mode [42] methods. They are both approximate solutions to the one-dimensional wave equation.

B.1 The Modified 1D Wave Equation

The one-dimensional wave equation can be written as:

$$\frac{\partial^2 E}{\partial z^2} + k(z)^2 E = 0 \tag{B.1}$$

with $k(z)$ as the propagation constant for the material, which depends on the configuration of the waveguide, and can be complex if the material has gain (or loss):

$$k^2 = k_o^2 n^2(z) + i2\alpha(z) k_o n(z) \tag{B.2}$$

where $n(z)$ is the effective index in the waveguide, and $\alpha(z)$ is the loss in the waveguide [1]. Both $n(z)$ and $\alpha(z)$ can be periodic with respect to z. For a periodic

variations in the index and the absorption, (using the more common approximations seen in the literature) one can write:

$$n(z) = n_0 + \Delta n \cos(2\beta_0 z + \Omega) \tag{B.3}$$

and

$$\alpha(z) = \alpha_0 + \Delta\alpha \cos(2\beta_0 z + \Omega + \theta) \tag{B.4}$$

where n_0 and α_0 are the unperturbed values of the index and absorption in the waveguide, Δn and $\Delta\alpha$ are the perturbations in the index and absorption, Ω and θ are phase shift terms used account for the relative phase differences between the two perturbations, and β_0 is the Bragg propagation constant, and is defined by:

$$\beta_0 = \frac{2\pi}{\lambda_B} = \frac{\pi}{\Lambda n_0} \tag{B.5}$$

where λ_B is the Bragg wavelength, Λ is the grating period and n_0 is the modal index. By using (B.3) and (B.4), it is possible to rewrite the expression for the propagation constant, (B.2):

$$k^2 \approx \beta^2 + 2j\beta\alpha_0 + 4\kappa\beta \cos(2\beta_0 z + \Omega) \tag{B.6}$$

in which $\beta(= k_0 n_0)$ is the real part of the propagation constant for an unperturbed waveguide, and κ is defined as the coupling coefficient:

$$\kappa = \frac{\pi\Delta n}{\lambda} + j\frac{\Delta\alpha}{2} = \kappa_i + \kappa_g \tag{B.7}$$

in which κ_i and κ_j represent the contributions of the index and the gain to the coupling coefficient. In deriving (B.6), it was assumed that $\Delta n \ll n_0$ and $\Delta\alpha \ll \alpha_0$, and $\theta = 0$ [1]. By using the modified form of the complex propagation constant, the wave equation can be rewritten as

$$\frac{d^2E}{dz^2} + \{\beta^2 + 2j\beta\alpha_0 + 2\kappa\beta e^{j(2\beta_0 z+\Omega)} + 2\kappa\beta e^{-j(2\beta_0 z+\Omega)}\}E = 0 \tag{B.8}$$

which is the equation that is commonly used in both the Floquet-Bloch and coupled-mode approaches to solving for periodic waveguides.

B.2 Calculation of the Coupling Coefficient

The coupling coefficient is calculated from the first order Fourier component of the grating. If we express the grating perturbation as a Fourier series we obtain the equation [1]:

$$\Delta\epsilon(x,y,z) = \sum_{q=-\infty}^{\infty} A_{q\neq 0}(x,y)\exp\left(\frac{2jq\pi z}{\Lambda}\right) \tag{B.9}$$

It can be shown than for a purely index coupled laser, the coupling coefficient (κ) is given by:

$$\kappa = \frac{{k_0}^2}{2\beta}\frac{\int_{corrugation} A_{q\neq 0}E_y^2(x)dx}{\int E_y^2(x)dx} \tag{B.10}$$

where $E_y(x)$ is the electric field in the transverse direction of the waveguide q is the order of the diffraction from the grating, and A is the Fourier coefficient of the grating [1].

For a trapezoidal grating, the sides of the grating can be described by two equations:

$$Z_1(x) = \frac{W_T}{2} + \frac{W}{g}(d_x + g - x) \tag{B.11}$$

and

$$Z_2(x) = \frac{W_T}{2} + 2W + W_B + \frac{W}{g}(x - d_x - g) \tag{B.12}$$

and are valid in the range of $x = d_x$ to $x = d_x + g$. In these equations, W_T, W_B and W are the lengths of the top, the bottom, and the falling distance of the trapezoid respectively (see Fig. B.1) [1]. By using these definitions, it is possible to show that for the trapezoidal corrugation, κ is described by the equation:

$$\kappa = \frac{k_0^2(n_{l+1}^2 - n_l^2)}{2m\pi\beta\int E_y^2(x)dx}\cdot\left|\int_{corrugation}\sin\left[\frac{2m\pi Z_1(x)}{\Lambda}\right]E_y^2(x)dx\right| \tag{B.13}$$

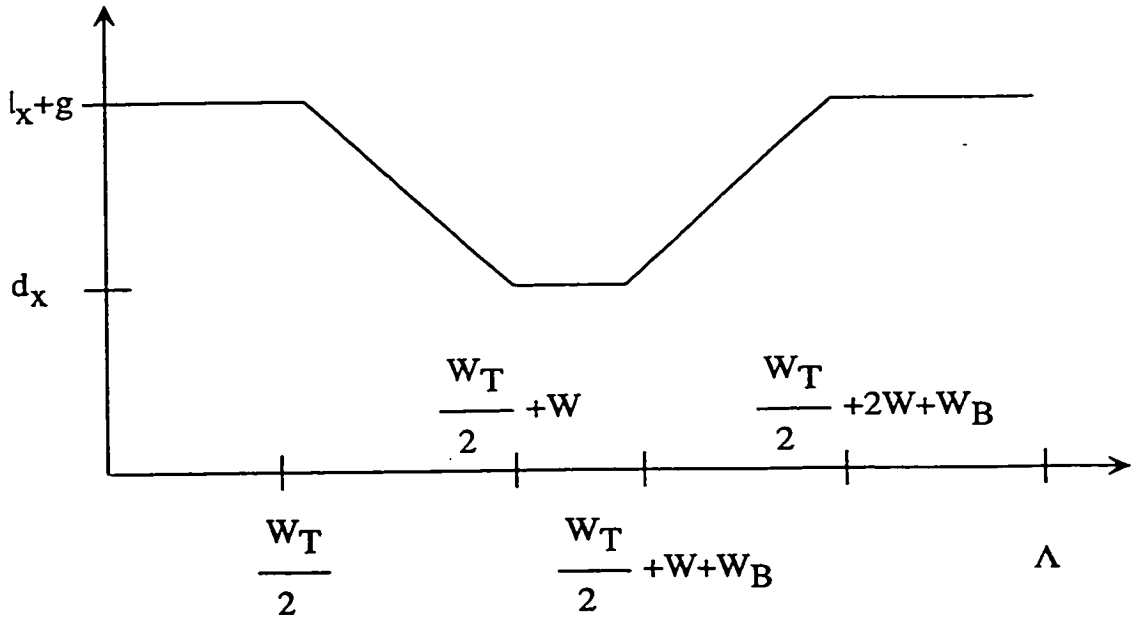

Figure B.1: Illustration of the notation used in describing the grating dimensions

where $E_y^2(x)$ is the electric field as determined from the waveguide structure and boundary conditions, n_{l+1} and n_l are the indices of the two layers that make up the grating, and m is the order of the grating [1]. Once the electric field is calculated by the techniques illustrated in Appendix A, it is a simple matter to calculate κ by using (B.13). The results from a sample calculation is shown in Fig 2.3.

B.3 Coupled-Mode Theory

The derivation of the coupled-mode theory is quite different from that of the Floquet-Bloch formalism. In the Floquet-Bloch formalism, one assumes a periodic media, and the wave equation is solved in terms of Floquet-Bloch waves. The infinite series is then truncated to make the solution solvable [62]. Coupled-mode theory, on the other hand, starts with a smooth waveguide and looks at the periodicity as

a perturbation of the waveguide solution. In this case, the solution is written as an infinite summation of modes of the unperturbed waveguide. Like the Floquet-Bloch formalism, this infinite summation is then truncated to make the equations solvable [1].

It can be shown the truncated Floquet-Bloch and coupled-mode analysis are equivalent, even though they both start with quite different assumptions. In the coupled-mode approach, one expands the fields in terms of the modes of a uniform waveguide, while the Floquet-Bloch analysis is a truncated version of the Floquet-Bloch wave solution to a periodic structure. In this situation, one finds a solution made up of two fundamental components and two associated space harmonics [63]. Both these assumed solutions are substituted into Maxwell's equation, (B.8). Since the physics of the problem is contained in Maxwell's equation, either solution is valid, and both the coupled-mode and Floquet-Bloch approaches will produce identical results [63].

The coupled-mode approach has one major advantage: it is relatively simple to formulate a matrix method. This is critical when one wishes to perform calculations on systems containing nonuniformities such as regions with different amounts of gain, or different gratings. Due to this major strength, the discussion here will focus on the coupled-mode approach to modeling waveguides with gratings.

B.3.1 Derivation and Theory

The derivation of coupled-mode theory starts with the wave equation (B.1). In this case, the trial solution is assumed to be a superposition of two opposing traveling waves:

$$E(z) = A(z)e^{-ik_{un}z} + B(z)e^{ik_{un}z} \tag{B.14}$$

where $A(z)$ and $B(z)$ are the complex amplitudes of the forward and backward propagating waves, and k_{un} is the complex propagation constant for the unperturbed waveguide, and is described by the equation:

$$k_{un}^2 = \beta^2 + 2i\beta\alpha_0 \approx (\beta + i\alpha_0)^2 \qquad (\text{since } \alpha_0 \ll \beta) \tag{B.15}$$

where $\beta = n_0 k_0$ is the real part of the wave propagation constant (k) for an unperturbed waveguide [1]. This trial solution is often rewritten in term of the Bragg propagation constant ($\beta_0 \equiv \frac{2\pi}{\lambda_B}$ where λ_B is the Bragg wavelength):

$$E(z) = R(z)e^{-i\beta_0 z} + S(z)e^{i\beta_0 z} \tag{B.16}$$

where $R(z)$ and $S(z)$ are the new complex amplitude terms. At this point, it is also useful to define a parameter known as the detuning factor:

$$\delta = \beta - \beta_0 \tag{B.17}$$

These equations are used to rewrite the wave equation (B.1) into two-coupled differential equations:

$$-\frac{dR}{dz} + (\alpha_o - j\delta)R = i\kappa_{RS}Se^{-i\Omega} \tag{B.18}$$

and

$$\frac{dS}{dz} + (\alpha_o - j\delta)S = i\kappa_{SR}Re^{-i\Omega} \tag{B.19}$$

where

$$\kappa_R S = \kappa_i + j\kappa_g e^{-i\theta} \tag{B.20}$$

is the forward-coupling coefficient and

$$\kappa_S R = \kappa_i + j\kappa_g e^{i\theta} \tag{B.21}$$

is the backward-coupling coefficient. For the usual situation with the index and gain perturbations are in phase ($\theta = 0$), one finds that $\kappa_R S = \kappa_S R = \kappa$ which is the

coupling coefficient as defined in (B.7) [1]. These differential equations can then be solved to find different parameters such as the threshold gain for a DFB. A good discussion is given in a book by Ghafouri-Shiraz [1]. However, the coupled-mode equations are quite cumbersome when it comes to solving complicated structures. Fortunately it is possible to recast them into a matrix method which allows for simple numerical techniques to calculate the electric fields for arbitrary structures.

B.3.2 Transfer Matrix Approach

One major benefit of the coupled-mode analysis is that it is possible to recast the solution into a matrix method [1] similar to the matrix methods discussed in Appendix A. As with other matrix methods, these matrix methods are extremely useful for calculating the characteristics of arbitrary structures. There are two main matrix approaches used for DFB structures: the transmission line matrix (TLM) method and the transfer matrix method (TMM). The main difference between the two methods is that the TLM method is performed in the time domain, and the TMM is performed in the frequency domain [1]. During the development of the DFB laser, we were mostly concerned with the frequency domain (i.e. the laser output spectrum), so the TMM is the model that is presented here. The TLM is more useful when examining modulation characteristics.

Transfer Matrix Formulation

The formulation of the TMM starts with the solution to the coupled-mode equations.

$$\begin{aligned} E(z) &= E_R(z) + E_s(z) \\ &= R(z)e^{-i\beta_0 z} + S(z)e^{i\beta_0 z} \end{aligned} \tag{B.22}$$

where $E_R(z)$ and $E_S(z)$ are the complex electric fields of the wave solutions and $R(z)$ and $S(z)$ are two slow varying complex amplitude terms [1].

After some manipulation of the above equations, it is possible to write a transfer matrix for a section of a waveguide:

$$\begin{bmatrix} E_R(z_2) \\ E_S(z_2) \end{bmatrix} = \boldsymbol{T}(z_2|z_1) \cdot \begin{bmatrix} E_R(z_1) \\ E_S(z_1) \end{bmatrix} = \begin{bmatrix} t_{11} & t_{12} \\ t_{21} & t_{22} \end{bmatrix} \begin{bmatrix} E_R(z_1) \\ E_S(z_1) \end{bmatrix} \tag{B.23}$$

where

$$t_{11} = (E - \rho^2 E^{-1}) \cdot e^{-i\beta_0(z_2 - z_1)}/(1 - \rho^2) \tag{B.24}$$

$$t_{12} = -\rho(E - E^{-1}) \cdot e^{-i\Omega} e^{-i\beta_0(z_2 + z_1)}/(1 - \rho^2) \tag{B.25}$$

$$t_{21} = \rho(E - E^{-1}) \cdot e^{j\Omega} e^{i\beta_0(z_2 + z_1)}/(1 - \rho^2) \tag{B.26}$$

$$t_{22} = -(\rho^2 E - E^{-1}) \cdot e^{-i\beta_0(z_2 - z_1)}/(1 - \rho^2) \tag{B.27}$$

where

$$\rho = \frac{i\kappa}{\alpha - i\delta + \gamma} \tag{B.28}$$

and Ω is the residual corrugation phase at the origin. The variable γ is the complex propagation constant in the material and is defined as

$$\gamma^2 = (\alpha_s - i\delta)^2 + \kappa^2 \tag{B.29}$$

It has also been shown that due to energy conservation,

$$\det \boldsymbol{T} = 1 \tag{B.30}$$

i.e. the determinant of the transfer matrix is unity [1]. Once the transfer matrix is calculated, it become a simple matter to calculate how the electric field varies as a function of position, z, once E_R and E_S are known at one position. It also becomes a simple matter to incorporate structural variations in the equations. Since E_R and

E_S are required to be continuous at the boundaries of the different sections, each region can be described by a different transfer matrix and then multiplied together to obtain a total matrix that describes the properties of the complete system [1]. This enables an identical method to be used for FP, DFB, DBR, or any other type of laser structure. The only difference is the strength of the grating (κ) in each section of the different lasers.

There are three other matrices which are useful in describing an arbitrary structure. The first one is the matrix for a phase shift:

$$\begin{aligned}\begin{bmatrix} E_R(z_2^+) \\ E_S(z_2^+) \end{bmatrix} &= \boldsymbol{P}(z_2^+|z_1^-) \cdot \begin{bmatrix} E_R(z_2^-) \\ E_S(z_2^-) \end{bmatrix} \\ &= \begin{bmatrix} e^{i\theta_2} & 0 \\ 0 & e^{i\theta_2} \end{bmatrix} \cdot \begin{bmatrix} E_R(z_2^-) \\ E_S(z_2^-) \end{bmatrix} \end{aligned} \tag{B.31}$$

where θ_2 corresponds to the phase change experienced by E_R and E_S [1]. This expression is useful for modeling lasers with a $\lambda/4$ phase shift. Facet reflectivities also often have to be modeled. The transfer matrix for a reflective interface is given by:

$$\begin{aligned}\begin{bmatrix} E_R(z_2^+) \\ E_S(z_2^+) \end{bmatrix} &= \frac{1}{e^{i\phi_2}\sqrt{1-\hat{r}_2^2}} \cdot \begin{bmatrix} 1 & -\hat{r}_2 \\ -\hat{r}_2 & 1 \end{bmatrix} \boldsymbol{T}(z_2|z_1) \\ &\quad \cdot \frac{1}{e^{i\phi_1}\sqrt{1-\hat{r}_1^2}} \cdot \begin{bmatrix} 1 & \hat{r}_1 \\ \hat{r}_1 & 1 \end{bmatrix} \begin{bmatrix} E_R(z_1^-) \\ E_S(z_1^-) \end{bmatrix} \end{aligned} \tag{B.32}$$

where 1 and 2 refer to the left and right facets respectively, r corresponds to the reflectivity and ψ corresponds to the phase change experienced by E_R and E_S when they are reflected [1]. Combined, these three matrices form the building blocks required to model any type of semiconductor laser.

Formulation of the Amplified Spontaneous Emission Spectrum

In calculating the output spectra of semiconductor lasers, one must take into account the effects of spontaneous emission. Spontaneous emission is commonly modeled as a series of noise sources distributed throughout the laser cavity. One common

approach of modeling noise sources in a laser cavity is the so-called "Green's Function" approach [1]. The general 1D wave equation, written as an inhomogeneous differential equation including noise (spontaneous emission) sources is:

$$\left[\frac{d^2}{dz^2} + \beta(z)^2\right] E_\omega(z) = F_\omega(z) \tag{B.33}$$

where $\beta(z)$ is the propagation constant, E_ω is the complex Fourier component of the electric field, and $F_\omega(z)$ is the Langevin-force term which is used to account for the spontaneous emission [1].

This equation can be solved by using a Green's function approach:

$$E_\omega = \int_{z_1}^{z} G(z, z') F_\omega(z') dz' \tag{B.34}$$

where z' locates the spontaneous noise source and $G(z, z')$ is Green's function [1]. In brief, this equation sums up the impulse responses of spontaneous noise sources stretching from $z = z_1$ to $z = z$ from which one can obtain an expression for the spontaneous emission power:

$$P_N(z_{N+1}) = \frac{hc\Delta\omega}{\lambda} \cdot \frac{n_{sp} g}{|y_{22}(z_{N+1}|z_1)|^2} \int_{z_1}^{z_{N+1}} |Z_1(z)|^2 dz \tag{B.35}$$

where Z_1 is one of the independent solutions of the homogeneous wave equation (with $F_\omega(z) = 0$):

$$Z_1(z) = E_R(z|z_1) + E_S(z|z_1) = y_{12}(z|z_1) + y_{22}(z|z_1) \tag{B.36}$$

and

$$\boldsymbol{Y}(Z_{N+1}|z) = \begin{bmatrix} y_{11} & y_{12} \\ y_{21} & y_{22} \end{bmatrix} \tag{B.37}$$

is the total matrix for the system (including reflectivities and phase shifts) from the right facet (z_{N+1}) to position z. Also, n_{sp} is the population inversion factor and g is the optical gain [1].

Equation (B.35) can easily be numerically integrated. It is then a simple matter to calculate the below-threshold output spectrum of the laser as a function of wavelength. (An example of a calculation of the spectrum of a 1000μm long index-coupled DFB with $\kappa L = 1$ by using this technique is illustrated in Fig. 2.2).

This section has discussed the main considerations required for the calculation of the below-threshold spectrum. The term "below-threshold" means that it is assumed that the carrier density (and hence the gain and index) is uniform throughout the length of the device and that the model does not take into account effects such as spatial hole burning. Above threshold models are much more complex, and entire degrees focus on incorporating as many parameters as possible to create a more accurate model. For a discussion on some of the non-linear effects found in above threshold models, please see the book by Ghafouri-Shiraz [1]. This book was the basis of most of the discussion in this chapter.

Appendix C

Processing Steps

This appendix outlines the step-by-step procedure developed for this thesis for fabricating integrated DFB lasers and electroabsorption modulators.

C.1 Grating Fabrication Steps for DFB and Modulator Fabrication

This section outlines a step by step procedure for patterning the grating in the fabrication DFB lasers and electroabsorption modulators. [1] The general procedure was discussed in Chapter 4.

Clean Sample:

1. Nitrogen (N_2) dry samples to remove light particles
2. A1 (Acetone) @ 90 °C for 5 min.
3. A2 @ 90 °C for 5 min.
4. M1 (Methanol)@ 90 °C for 5 min.
5. M2 @ 90 °C for 5 min.
6. De-ionized water (DI) rinse.
7. Blow Dry.
8. UV ozone for 10 min.
9. HF dip in 10: 1, DI:HF for 2 min.

[1] The DFB grating processing steps are based on those developed by Susan Nagy at McMaster University and were adapted and improved to enable the fabrication of the devices in this thesis. The RWG laser processing procedures are based on those developed by Susan Nagy and Kevin Cearns.

10. DI rinse for 2 min.
11. Blow Dry

Pattern for Modulators

1. Pattern modulator and laser regions using standard RWG processing procedures.
   - Bake sample at 100 °C for 5min. to remove moisture.
   - Take cooled devices and spin PR 1808 at 4000rpm for 30 sec. (allow 30s between application and spin time).
   - Wait 5 min., soft bake at 110 °C for 90 sec.
   - Wait 5 min. (mix developer).
   - Developer solution- 5: 1, DI:Developer.
   - Align mask so laser and modulator regions run parallel to the major flat.(the ridge waveguides will run perpendicular to the major flat).
   - Expose at 25mJ.
   - Develop in developer solution, slowly agitating sample for 20or less.
   - DI rinse for 2 min, blow dry.
   - Check development (remember filters).
   - Hard Bake at 130 °C for 2 min.
2. Etch top InP layer for 15s using 1:2 $HCl:H_3PO_4$
3. Etch top InGaAs layer for 15s using 1:8:80 $H_2SO_4:H_2O_2:H_2O$
4. Remove photoresist by soaking in acetone at 80 °C for 5 min.
5. Remove top InP layer (in both sections) by etching for 1 min. using 1:2 $HCl:H_3PO_4$
6. Clean for Regrowth
   - 20 min. UV ozone
   - 2 min. Buffered HF (BHF)
   - 5 min. DI rinse
   - blow dry using N_2
7. Submit for regrowth
8. When sample is returned, anneal for band gap shifting
9. clean using standard techniques
10. remove native oxide- 1 min. 49%HF.
11. etch off top layers to the 250Å InP layer using the standard selective etches (1:2 $HCl:H_3PO_4$ and 1:8:80 $H_2SO_4:H_2O_2:H_2O$) (PL can be done before the last InGaAs layer is removed to ensure a clean surface for subsequent processing steps)

Pattern Gratings

1. Allow HeCd Laser to warm up for at least and hour
2. Bake at 80 °C for 5 min. to remove water and to ensure hot plate is at the right temperature.
3. Apply thinned photoresist using standard techniques (2:3 Shipley 1808PR:Thinner)
4. spin at 5000 RPM
5. let rest 5 min.
6. bake at 80 °C for 1 min.
7. expose in holographic system for 40 sec. (Detector reading=250μW)
8. develop in Microposit CD-30 developer for 45 sec.- slow agitation
9. check development using the techniques discussed earlier.
10. hard bake at 110 °C for 2 min.
11. etch in 1:1:20 HBr:HNO_3:DI Special care is required
    - Mix acids together
    - Stir well for 90sec.
    - Wait 10 min.
    - Add acids to water at one time.
    - let sit for at least 1 hour.

    *Note: this procedure produces acids with different etch rates depending on how the acids are mixed. Please see text.
12. etch for 30s using gentle agitation. (Will result in 50nm grating depth in the Q)
13. Rinse
14. Soak in Acetone for 5 min. to remove PR
15. Remove oxide if present
16. etch in 1:2 HCL:H_3PO_4 for 30s to remove InP.
17. rinse for at least 5 min. using agitation. (H_3PO_4 sticks to the surface)
18. etch off the remaining InP and InGaAs layers using the standard selective etches. There should now be regions with and without a grating.
19. Clean for regrowth using standard procedures
    - 20 min. UV ozone.
    - 2 min. BHF
20. Submit for regrowth

C.2 Ridge Waveguide Fabrication Steps

The general procedure fore RWG laser fabrication can be summarized as: sample cleaning, patterning ridges, depositing isolation layer, opening windows in dielectric for the top contact, p-type metalizing the top contacts, lift-off to form contacts, sample thinning, backside metalization, and then annealing to form ohmic contacts. The details are as follows.

Clean Sample:

1. N_2 dry samples to remove light particles
2. A1 (Acetone) @ 90 °C for 5 min.
3. A2 @ 90 °C for 5 min.
4. M1 (Methanol)@ 90 °C for 5 min.
5. M2 @ 90 °C for 5 min.
6. Deionized water (DI) rinse.
7. Blow Dry.
8. UV ozone for 10 min.
9. HF dip in 10: 1, DI:HF for 2 min.
10. DI rinse for 2 min.
11. Blow Dry

Apply Spin-On-Glass:

1. Apply spin-on-glass (SOG) 111 at 4000 rpm for 30 sec.
2. Place samples on a microscope slide, and cover with a petri dish.
3. Place samples in a cold oven. Turn on to "9" and "HI" allowing oven to ramp up to $\sim$ 250 °C.

Photolithography for SiO_2 etch and device etch:

1. Open oven, allowing devices to cool to room temperature. (If the devices have been sitting around for a while, heat to 120 °C on the hot plate for at least 5 minutes to drive off the water, and then allow to cool)
2. Turn on mask aligner- giving 30 minutes to warm up.
3. Take cooled devices and spin PR (Shipley 1808) at 4000rpm for 30 sec. (allow 30s between application and spin time).
4. Wait 5 min., soft bake at 110 °C for 90 sec.
5. Wait 5 min. (mix developer).

6. Developer solution- 5: 1, DI:Developer (Microposit 351 developer).
7. Align mask so ridges are perpendicular to the major flat.
   Mask Aligner using HP mode:
   Follow instructions on aligner.
   Exposure Times:
   - Etching: 25mJ/cm^2. (i.e 25.0/P(sec.) P=Power reading in mW/cm^2
   - Lift off: 50mJ/cm^2.
8. Develop in developer solution, slowly agitating sample for 15+5+5 sec.
9. DI rinse for 2 min, blow dry.
10. Check development (remember filters).
11. Check ridge width.
12. Hard Bake at 130 °C for 2 min.
13. Etch in (premixed buffered) HF solution using slow agitation.
    20+ seconds for Wet etching
    25+ seconds for RIE. (Check under microscope)
14. DI rinse and blow dry.
15. A1 at 90 °C for 5 min. (PR will lift. If it doesn't use a PR stripper. Stripper etches InP though).
16. A2 at 90 °C for 5 min.
17. Rinse well , >5min. (Especially if PR stripper is used instead of acetone)
18. Mix Acids for Rib etching.
    (3:1 H_3PO_4:HCl for a vertical InP etch)
    (1:8:80 H_2SO_4:H_2O_2:DI for InGaAs)
19. Etch InGaAs for approximately 30sec. (4000Å/min)
20. Etch InP for approx. 2 min. (4000-7000Å/min. Annealed material might be even slower).
    Make sure solutions are well mixed for reproducibility.
21. rinse for 5 min.

Photolithography for Oxide Windows

1. Apply 1000 CVD dielectric (SiO_xN_y) by following instructions.(Best)
   or
   Apply 311 SOG at 4000RPM for 30sec.
2. Bake sample at 120 °C for at least 5 min. and allow to cool.
3. Spin PR (1808) at 4000 rpm for 30 (as before).
4. Soft bake at 110 °C for 90 sec.
5. Expose and develop as before.
6. Hard Bake at 130 °C for 90s
7. Etch SiO_2
   85+ seconds for PECVD oxide
   15 sec for SOG.

8. Remove PR with acetone as before.

Photolithography for Lift-off:

1. Bake samples at 120 °C to remove moisture.
2. Spin PR 1808 at 4000 rpm for 30 sec.
3. Wait 5 min.
4. Softbake at 80 °C for 90 sec.
5. Expose sample in mask aligner with 50mJ.
6. Soak in Toluene for 6 min.
7. Blow dry immediately and bake at 80 °C for 45 sec.
8. Develop in 5:1 developer mixture for 2 min- agitate well to remove exposed PR.
9. DI rinse, dry, and check (remember filters)
10. Metalize using 60° angled stage(Ti/Pt/Au, 250/500/1200 each side).

Lift-Off

1. Soak sample in acetone bath until metal lifts from device (5-10 min.) (Heat if required).
2. Spray with acetone bottle to agitate the metal.
3. Rinse device in acetone, methanol, and then DI.
4. Dry Device.
5. Mount to polishing blocks using crystal-bond.
6. Thin sample (from 350μm to 100-120μm).
7. Clean with acetone to remove crystal-bond.
8. Rinse with DI
9. Clean with a 5 min. bath of Trichloroethylene, acetone, methanol, and then IPA.
10. DI rinse
11. Metalization. (Ni/Ge/Au 250/500/1200)
12. Anneal at 425 °C ramping at 50 °C/s for 30 sec.
13. Cleave.

References

[1] H. Ghafouri-Shiraz and B. Lo, *Distributed Feedback Laser Diodes: Principles and Physical Modeling.* Chichester: John Wiley and Sons, first ed., 1996.

[2] B. Streetman, *Solid State Electronic Devices.* Prentice Hall, 4 ed., 1995.

[3] P. S. Zory, *Quantum Well Lasers.* Academic Press, 1993.

[4] D. Delprat, A. Ramdane, A. Ougazzaden, H. Nakajima, and M. Carr, "Integrated multiquantum well distributed feedback laser-electroabsorption modulator with a negative chirp for zero bias voltage," *Electronics Letters*, vol. 33, no. 1, pp. 53–55, 1997.

[5] R. M. Lammert, S. D. Roh, J. Highes, M. L. Osowski, and J. J. Coleman, "Mqw dbr lasers with monolithically integrated external-cavity electroabsorption modulators fabricated without modification of the active region," *IEEE Photonics Technology Letters* , vol. 9, no. 5, pp. 566–568, 1997.

[6] D. A. B. Miller, J. S. Weiner, and D. S. Chemla, "Electric-field dependence of linear optical properties in quantum well structures: waveguide electroabsorption and sum rules," *IEEE Journal of Quantum Electronics*, vol. 22, no. 9, pp. 1816–1803, 1986.

[7] M. Behet, R. Hövel, A. Kohl, A. Mesquida Küsters, B. Opitz, and K. Heime, "MOVPE growth of II-IV compounds for optoelectronic and electronic applications," *Microelectronics Journal*, vol. 27, pp. 297–334, 1996.

[8] M. Aoki, M. Suzuki, T. Taniwatara, H. Sano, and T. Kawano, "New photonic device integration by selective-area MOVPE and its application to optical modulator/laser integration," *Microwave and optical technology letters*, vol. 7, no. 3, pp. 132–139, 1994.

[9] T. Tanbun-Ek, Y. Chen, J. Grenko, E. Byrne, J. Johnson, R. Logan, A. Tate, A. Sergent, K. Wecht, P. Sciortine, and S. Chu, "Integrated DFB-DBR laser modulator grown by selective-area metalorganic vapor phase epitaxy growth technique," *Journal of crystal growth*, vol. 145, pp. 902–906, 1994.

[10] K. Kudo, M. Ishizaka, T. Sasaki, H. Yamazaki, and M. Yamaguchi, "1.52-1.59μm range different-wavelength modulator-integrated DFB-LDs fabricated on a single wafer," *IEEE Photonics technology letters*, vol. 10, no. 7, pp. 929–931, 1998.

[11] S. Nagy, "GSMBE growth and characterization of InGaAs-InP structures on SiO_2 patterned substrates," Master's thesis, McMaster University, Hamilton, Ontario, Canada, 1995.

[12] J. H. Marsh, O. P. Kowalski, S. D. MacDougall, B. C. Qiu, A. McKee, C. J. Hamilton, R. M. De La Rue, and A. C. Bryce, "Quantum well intermixing in material systems for 1.5μm," *Journal of Vacuum Science Technology A*, vol. 16, pp. 810–816, March 1998.

[13] S. Charbonneau, E. Koteles, P. Poole, J. He, G. C. Aers, J. Haysom, M. Buchanan, Y. Feng, A. Delage, F. Yang, M. Davies, R. Goldberg, P. Piva,

and I. Mitchell, "Photonic integrated circuits fabricated using ion implantation," *IEEE Journal of Selected Topics in Quantum Electronics*, vol. 4, no. 4, pp. 772–793, 1998.

[14] J. Chang, K. Carey, J. Turner, and L. Hodge, "Compositional non-uniformities in selective area growth of GaInAs on InP grown my OMVPE," *Journal of Electronic Materials*, vol. 19, no. 4, pp. 345–348, 1990.

[15] H. Roehle, H. Schroeter-Janssen, and R. Kaiser, "Large- and selective-area LP-MOVPE growth of InGaAsP-based bulk QW layers under nitrogen atmosphere," *Journal of Crystal Growth*, vol. 170, pp. 109–112, 1997.

[16] M. Aoki, M. Suzuki, H. Sano, T. Kawano, T. Ido, T. Taniwatari, K. Uomi, and A. Takai, "InGaAs/InGaAsP MQW electroabsorption modulator integrated with dfb laser fabricated by band-gap energy control elective area MOCVD," *IEEE Journal of Quantum Electronics*, vol. 29, no. 6, pp. 2088–2096, 1993.

[17] S. A. Schwartz, P. Mei, T. Venkatesan, R. Bhat, D. M. Hwand, C. L. Schwartz, M. Koza, L. Nazar, and B. J. Skromme, "InGaAs/InP superlattice mixing induced by Zn or Si diffusion," *Applied Physics Letters* , vol. 53, no. 12, pp. 1051–1052, 1988.

[18] S. K. Si, D. H. Yeo, K. H. Yoon, and S. J. Kim, "Area selectivity of InGaAsP-InP multiquantum-well intermixing by impurity-free vacancy diffusion," *IEEE Journal of Selected Topics In Quantum Electronics*, vol. 4, no. 4, pp. 619–623, 1998.

[19] T. Miyazawa, H. Iwamura, and M. Naganuma, "Integrated external-cavity InGaAs/InP lasers using cap-annealed disordering," *IEEE Photonics Technology Letters* , vol. 3, no. 5, pp. 421–423, 1991.

[20] N. Cao, B. B. Elenkrig, J. G. Simmons, and D. A. Thompson, "Band-gap blue shift by impurity-free vacancy diffusion in 1.5μm strained-InGaAsP/InP multiple quantum-well laser structure," *Applied Physics Letters* , vol. 70, pp. 3419–3421, June 1997.

[21] A. Hamoudi, E. V. K. Rao, P. Krauz, A. Ramdane, A. Ougazzaden, D. Robein, and Thirbierge, "Controlled disordering of compressively strained InGaAsP multiple quantum wells under SiO:P encapsulant and application to laser-modulator integration.," *Journal of Applied Physics* , vol. 78, no. 9, pp. 5638–5641, 1995.

[22] S. Shi, P. L. K. Wa, A. Miller, J. Pamulapati, P. Cooke, and M. Dutta, "The controlled disordering of quantum wells using surface oxidation," *Semiconductor Science and Technology*, vol. 9, pp. 1564–1566, 1994.

[23] J. S. Tsang, C. P. Lee, S. H. Lee, K. L. Tsai, C. M. Tsai, and J. C. Fan, "Compositional disordering of InGaAs/GaAs heterostructures by low-temperature-grown GaAs layers," *Journal of Applied Physics*, vol. 79, no. 2, pp. 664–670, 1996.

[24] Y. Chiu, F. S., D. Lasaosa, and J. Bowers, "Ultrafast (370 GHz bandwidth) p-i-n traveling wave photodetector using low-temperature-grown GaAs," *Applied Physics Letters*, vol. 71, no. 17, pp. 2508–2510, 1997.

[25] K. Li Dessau, "Insights into high-speed detectors and high-frequency techniques." Newfocus, Inc. Application Note 1.

[26] T. H. Wood, J. Z. Pastalan, C. A. Burrus, B. C. Johnson, B. I. Miller, J. L. deMiguel, U. Koren, and M. G. Young, "Electric field screening by photogenerated holes in multiple quantum wells: a new mechanism for absorption saturation," *Applied Physics Letters*, vol. 57, no. 11, pp. 1081–1083, 1990.

[27] T. Ido, H. Sano, S. Tanaka, and H. Inoue, "Frequency-domain measurement of carrier escape times in MQW electro-absorption optical modulators," *IEEE Photonics Technology Letters*, vol. 7, no. 12, pp. 1421–1423, 1995.

[28] M. K. Chin, P. K. L. Yu, and W. S. C. Chang, "Optimization of multiple quantum well structures for waveguide electroabsorption modulators," *IEEE Journal of Quantum Electronics*, vol. 27, no. 3, pp. 696–701, 1991.

[29] R. Sahara, K. Morito, K. Sato, K. Kotaki, H. Soda, and N. Okazaki, "Strongly improved frequency response at high-optical input powers from InGaAsP compensated strain MQW electroabsorption modulators," *IEEE Photonics Technology Letters*, vol. 7, no. 9, pp. 1004–1006, 1995.

[30] F. Devaux, F. Dorgeuille, A. Ougazzaden, F. Huet, M. Carr, A. Carenco, M. Henry, Y. Sorel, J.-F. Kerdiles, and E. Jeanney, "20 Gbit/s operation of a high-efficiency InGaAsP/InGaAsP MQW electroabsorption modulator with 1.2-v drive voltage," *IEEE Photonics Technology Letters*, vol. 5, no. 11, pp. 1288–1290, 1993.

[31] J. A. Cavaills, D. A. B. Miller, J. E. Cunningham, P. L. K. Wa, and A. Miller, "Simultaneous measurement of electron and hole sweep-out from quantum wells and modeling of photoinduced field screening dynamics," *IEEE Journal of Quantum Electronics*, vol. 28, no. 10, pp. 2486–2497, 1992.

[32] D. J. Moss, T. Ido, and H. Sano, "Photogenerated carrier sweep-out times in strained InGaAs/InAlAs quantum well modulators," *Electronics Letters*, vol. 30, no. 5, pp. 405–406, 1994.

[33] H. H. Tan, C. Jagadish, M. J. Lederer, B. Luther-Davies, J. Zou, J. H. Cockayne, M. Haiml, U. Sienger, and U. Keller, "Role of implantation-induced defects on the response time of semiconductor saturable absorbers," *Applied Physics Letters*, vol. 75, no. 10, pp. 1437–1439, 1999.

[34] U. Keller, K. J. Weingarten, F. X. Krtner, D. Kopf, B. Braun, I. D. Jung, R. Fluck, C. Hnniger, N. Matuschek, and J. Aus der Au, "Semiconductor saturable absorber mirrors (SEAM's) for femtosecond to nanosecond pulse generation in solid-state lasers," *IEEE Journal of Selected Topics in Quantum Electronics*, vol. 2, no. 3, pp. 435–452, 1996.

[35] H.-H. Wang, P. Grenier, J. F. Whitaker, H. Fujioka, J. Jasinski, and Z. Liliental-Weber, "Ultrafast response of As-implanted GaAs photoconductors," *IEEE Journal of Quantum Electronics*, vol. 1, no. 3, pp. 630–635, 1996.

[36] S. Dankowski, P. Kiesel, M. Ruff, D. Streb, S. Tautz, U. Keil, C. Sørensen, B. Knpfer, M. Kneissl, and G. Dhler, "Optical and electro-optical investigation of low-temperature grown GaAs," *Materials Science and Engineering B*, vol. B44, pp. 316–319, 1997.

[37] R. Takahashi, Y. Kawamura, and H. Iwamura, "Ultrafast 1.55μm all-optical switching using low-temperature-grown multiple quantum wells," *Applied Physics Letters*, vol. 68, no. 2, pp. 153–155, 1996.

[38] H. S. Loka, S. D. Benjamin, and P. W. E. Smith, "Optical characterization of low-temperature-grown GaAs for ultrafast all-optical switching devices," *IEEE Journal of Quantum Electronics*, vol. 34, no. 8, pp. 1427–1436, 1998.

[39] H. Tsuda, A. Hirano, R. Takahashi, K. Sato, and K. Hagimoto, "2.4 Gbit/s all-optical pulse discrimination experiment using a high-speed saturable absorber optical gate," *Electronics Letters*, vol. 32, pp. 365–366, 1996.

[40] L. Quan, S. Benjamin, P. Smith, B. Robinson, and D. Thompson, "Sub-picosecond carrier lifetime in beryllium doped InGaAsP grown by He-plasma-assisted molecular beam epitaxy," *Applied Physics Letters*, vol. 71, no. 11, pp. 1513–1515, 1997.

[41] F. Koyama and K. Iga, "Frequency chirping in external modulators," *Journal of Lightwave Technology*, vol. 6, no. 1, pp. 87–93, 1988.

[42] H. Kogelnik, "Coupled wave theory for thick hologram gratings," *The Bell System Technical Journal*, vol. 48, no. 9, p. 2909, 1969.

[43] D. T. Cassidy, "Technique for measurement of the gain spectra of semiconductor diode lasers," *Journal of Applied Physics*, vol. 56, no. 11, pp. 3096–3099, 1984.

[44] T. H. Wood, "Direct measurement of the electric-field-dependent absorption coefficient in GaAs/AlGaAs multiple quantum wells," *Applied Physics Letters* , vol. 48, no. 21, pp. 1413–1415, 1986.

[45] T. H. Wood, "Multiple quantum well (MQW) waveguide modulators," *Journal of Lightwave Technology*, vol. 6, no. 6, pp. 743–757, 1988.

[46] C. H. Wallace, E. Herbert Li, and J. Micallef, "Polarization-insensitive electroabsorption modulation using interdiffused InGaAs(P)-InP quantum wells," *IEEE Journal of Quantum Electronics*, vol. 33, no. 9, pp. 1316–1322, 1997.

[47] C. Vassallo, "Reflectivity of multidielectric coatings deposited on the end facet of a weakly guiding dielectric slab waveguide," *Optical Society of America*, vol. 5, no. 11, pp. 1918–1925, 1988.

[48] J. Hazell, "Optical coupling as a function of ridge gap in a 2-section RWG laser calculated by BPM." Private Communications, 1998.

[49] H. Pinkney, D. Thompson, B. Robinson, P. Mascher, P. Simpson, U. Myler, J. Kang, and M. Frankey, "Characterization of annealed high-resistivity InP grown by He-plasma-assisted epitaxy," *Journal of Vacuum Science Technology A*, vol. 16, pp. 772–775, March 1998.

[50] M. Melloch, J. Nolte, D.D. Woodall, J. Chang, D. Janes, and E. Harmon, "Molecular beam epitaxy of nonstoichiometeric semiconductors and multiphase material systems," *Critical Reviews in Solid State and Materials Science*, vol. 21, no. 3, pp. 189–263, 1996.

[51] H. Pinkney, *Characterization of InP and InGaAsP grown by He-plasma-assisted GSMBE.* Ph.d., McMaster University, 1999.

[52] J. Hazell, "Dielectric-enhanced intermixing of $In_{(1-x)}Ga_xAs_yP_{(1-y)}$ quantum wells." Private Communications, 2000.

[53] B. Robinson, J. Bursink, D. Thompson, G. Weatherly, and R. Streater, "Regrowth over grating-etched InGaAsP," *Proceedings, IPRM 1999*, 1999.

[54] H. Takeuchi, K. Tsuzuki, K. Sato, M. Yamamoto, Y. Itaya, A. Sano, M. Yoneyama, and T. Otsuji, "Very high-speed light-source module up to 40gb/s containing an mqw electroabsorption modulator integrated with a DFB laser," *IEEE Journal of Selected Topics in Quantum Electronics*, vol. 3, no. 2, pp. 336–343, 1997.

[55] A. Ramdane, P. Krauz, E. Rao, A. Ougazzaden, D. Robein, A. Gloukhian, and Carré, "Monolithic integration of InGaAsP-InP strained-layer distributed feedback laser and external modulator by selective quantum-well interdiffusion," *IEEE Photonics Technology Letters*, vol. 7, no. 9, pp. 1016–1018, 1995.

[56] B. Jonsson and S. Eng, "Solving the schrödinger equation in arbitrary quantum-well potential profiles using the transfer matrix method," *IEEE Journal of Quantum Electronics* , vol. 26, no. 11, pp. 2025–2035, 1990.

[57] L. M. Walpita, "Solutions for planar optical waveguide equations by selecting zero elements in a characteristic matrix," *Journal of the Optical Society of AmericaA* , vol. 2, no. 4, pp. 595–602, 1985.

[58] G. Bastard, "Superlattice band structure in the envelope-function approximation," *Physical Review B*, vol. 24, no. 10, pp. 5693–5697, 1981.

[59] A. Macrander and S. Lau, "X-ray, photoluminescence, stoichiometry, and thickness mapping of $In_{(1-x)}Ga_xAs_yP_{(1-y)}$," *Journal of Electrochemical Society* , vol. 138, no. 4, pp. 1147–1155, 1991.

[60] S. L. Chuang, "Efficient band-structure calculations of strained quantum wells," *Physical Review B*, vol. 43, no. 12, pp. 9649–9661, 1991.

[61] H. Burkhard, "Effective phase and group indicies for $In_{(1-x)}Ga_xAs_yP_{(1-y)}$ / InP waveguide structures," *Journal of Applied Physics* , vol. 55, no. 2, pp. 503–508, 1984.

[62] S. Wang, "Principles of Distributed Feedback and Distributed Bragg Reflector lasers," *Wave Electronics*, vol. 1, pp. 31–59, 1974.

[63] A. Yariv and A. Gover, "Equivalence of the Coupled Mode and Floquet-Bloch formalisms in periodic optical waveguides," *Applied Physics Letters* , vol. 26, no. 9, pp. 537–539, 1975.